PSI-1319/
TR-1829

A Diode Laser Based Flux Sensor for Characterization of Terrestrial CO_2 Sources and Sinks

Contract No. DE-FG02-99ER82858

Final Report

Prepared by:

David M. Sonnenfroh, Phillip A. Mulhall, and Mark G. Allen
Physical Sciences Inc.
20 New England Business Center
Andover, MA 01810

Prepared for:

DOE/Environmental Sciences Division
Germantown, MD

February 2003

SBIR RIGHTS NOTICE (MAR 94)

These SBIR data are furnished with SBIR rights under Contract No. DE-FG02-99ER82858. For a period of 4 years after acceptance of all items to be delivered under this contract, the Government agrees to use these data for Government purposes only, and they shall not be disclosed outside the Government (including disclosure for procurement purposes) during such period without permission of the Contractor, except that, subject to the foregoing use and disclosure prohibitions, such data may be disclosed for use by support Contractors. After the aforesaid 4-year period, the Government has a royalty-free license to use, and to authorize others to use on its behalf, these data for Government purposes, but is relieved of all disclosure prohibitions and assumes no liability for unauthorized use of these data by third parties. This Notice shall be affixed to any reproductions of these data, in whole or in part.

PSI-1319/
TR-1829

A Diode Laser Based Flux Sensor for Characterization of Terrestrial CO_2 Sources and Sinks

Contract No. DE-FG02-99ER82858

Final Report

Prepared by:

David M. Sonnenfroh, Phillip A. Mulhall, and Mark G. Allen
Physical Sciences Inc.
20 New England Business Center
Andover, MA 01810

Prepared for:

DOE/Environmental Sciences Division
Germantown, MD

February 2003

SBIR RIGHTS NOTICE (MAR 94)

These SBIR data are furnished with SBIR rights under Contract No. DE-FG02-99ER82858. For a period of 4 years after acceptance of all items to be delivered under this contract, the Government agrees to use these data for Government purposes only, and they shall not be disclosed outside the Government (including disclosure for procurement purposes) during such period without permission of the Contractor, except that, subject to the foregoing use and disclosure prohibitions, such data may be disclosed for use by support Contractors. After the aforesaid 4-year period, the Government has a royalty-free license to use, and to authorize others to use on its behalf, these data for Government purposes, but is relieved of all disclosure prohibitions and assumes no liability for unauthorized use of these data by third parties. This Notice shall be affixed to any reproductions of these data, in whole or in part.

TABLE OF CONTENTS

Appendices

LIST OF FIGURES

LIST OF FIGURES (Continued)

LIST OF FIGURES (Continued)

LIST OF FIGURES (Continued)

LIST OF FIGURES (Continued)

LIST OF TABLES

Executive Summary

In this Phase II program, Physical Sciences Inc. (PSI) designed, fabricated, and field demonstrated a next generation, near-infrared tunable diode laser-based sensor for boundary layer flux measurements of greenhouse gas trace species, specifically CO_2. This next generation sensor is based on robust, near-infrared telecom diode lasers in combination with balanced optical detection, a high sensitivity detection technique. Advantage is taken of mature fiber optic technology to enable an *in situ*, open path air probe that is located remotely from the main sensor body. An *in situ* probe minimizes both sampling losses and loss of response to high frequency eddies. This next generation flux sensor provides new measurement capabilities including: measurement of multiple species, measurement of isotopes, and very high speed measurements. Our prototype measured both $^{12}CO_2$ and H_2O simultaneously at 10 Hz. We showed that, since mixing ratios were measured, the usual corrections to the measured CO_2 flux arising from active fluxes of latent heat and water vapor were not necessary. We also demonstrated measurements of $^{13}CO_2$. These new sensors are needed to support space- and airborne remote sensing programs and development of computational models of global climate change.

During this program, we reviewed and completed our design for a prototype eddy flux covariance sensor that we began in the Phase I program. Our sensor was specifically designed for boundary layer flux measurements above a hardwood forest canopy. The sensor is actually a suite of component sensors that includes a near-IR tunable diode laser absorption spectrometer for high speed concentration measurements of $^{12}CO_2$ and H_2O. A sonic anemometer for wind measurements and a barometer for pressure measurements are also included in the suite. The system is composed of a main processing unit and three *in situ* air probes specifically designed for flux measurements via eddy covariance. The prototype field sensor is fully automated and single-man portable.

We characterized the laser absorption spectrometer's precision using standard practices and precision gas mixtures. We achieved a precision of 1.5 ppmv CO_2 (0.4% of ambient) over 10 min at 10 Hz operation. For H_2O, our precision was 30 ppmv (0.1% relative humidity).

The flux sensor suite was field tested at the Vermont Monitoring Cooperative Forest Canopy Experiment Station, which is part of the Proctor Maple Research Center in Underhill Center, VT. We tested for two weeks in August 2001 and again for two weeks in July 2002. For these demonstrations, we had available a commercial nondispersive infrared CO_2 and H_2O analyzer for intercomparison. As example results, the TDL-based sensor measured a CO_2 flux of -0.68 ppmv*m/s at 1 pm, 22 July 2002 while the NDIR sensor measured a CO_2 flux of -0.45 ppmv*m/s. The CO_2 flux level expected from the literature was -0.55 ppmv*m/s. The CO_2 fluxes measured by the TDL sensor were on average 48% larger than the NDIR sensor fluxes. In addition, the H_2O fluxes measured by the TDL sensor were on average 31% larger than the NDIR sensor fluxes. The NDIR channel measured flux to better than 10%. The flux measurement precision for the TDL channel was three to five times larger. The two data sets agree within the error bars of the TDL channel. However, two potential sources for the measurement differences are discussed. The TDL sensor exhibited good high frequency response. We also demonstrated measurement of $^{13}CO_2$ during the second field test.

Commercial applications of this technology span many fields and disciplines including environmental fenceline monitoring of pollution, automotive emissions sensing, combustion diagnostics, treaty verification and antiterrorist operations via detection of fugitive emissions and explosives, medical breath diagnostics, diagnostics for semiconductor manufacturing including feedstock gas impurity analysis, and battlefield detection of toxic agents.

1. Introduction

As the burden of CO_2 in the atmosphere continues to increase, prediction of global climate change is predicated on a detailed understanding of the exchanges of greenhouse gases with the terrestrial ecosystem and with the hydrosphere. High quality measurements of biogenic and deposition trace gas exchange fluxes will help quantify changes in the carbon cycle occurring in the terrestrial biosphere. These measurements are needed in studies of the bio-diversity of ecosystems, their response to changing environmental parameters, and their feed-backs to the processes involved in global climate change. New field sensors are needed to make these flux measurements with high precision. In this Phase II program, we have designed, fabricated, tested, and field-demonstrated this next generation sensor. This new sensor is based on robust, near-infrared tunable diode laser (TDL) optical technology and provides new measurement capabilities to the community. During this Phase II program, we have fabricated and demonstrated a near-infrared tunable diode laser-based eddy covariance flux sensor. Our sensor has a very small footprint, low power consumption, and is easily transported, setup, and maintained by a single technician. It is capable of unattended, extended field deployment.

The TDL-based sensor is designed to make high precision and high speed measurements of CO_2 fluxes via optical absorption using the eddy covariance technique. By combining a near-IR tunable diode laser absorption spectrometer with an open path, *in situ* air probe, our sensor design represents a significant improvement over existing extractive sampling eddy covariance instruments and offers new measurement capabilities. The open path air probe bypasses concerns inherent with extractive sampling, including loss of high frequency eddy components, as well as wall losses, and removes the need for high-speed air pumps. New measurement capabilities include the ability to monitor several species, such as CO_2 and H_2O, simultaneously. The high selectivity provided by the near-IR diode laser probe offers the capability to monitor isotope fractionation, that is, both $^{12}CO_2$ and $^{13}CO_2$ can be measured for source apportionment. In addition, a network of air probes can be created using fiber optic links, which enables deployment over variable field scales and vegetation types.

In Phase II, we took the design and development work that was developed during the Phase I program and finalized our design for a field prototype eddy flux covariance sensor for CO_2. We then fabricated that prototype, tested it, and demonstrated it in the field on two separate occasions. The prototype has three channels, one each for $^{12}CO_2$, H_2O, and $^{13}CO_2$. The TDL absorption spectrometer has sensitivities of 0.3 ppmv and 20 ppmv for CO_2 and H_2O respectively, a measurement rate of 500 Hz, and a reporting rate of 10 Hz. The overall sensor suite also includes a sonic anemometer and a precision barometer. We demonstrated the sensor suite in August 2001 and July 2002 at the Proctor Maple Research Center in Underhill Center, VT. During these demonstrations, we intercompared it with an *in situ* nondispersive infrared CO_2 and H_2O sensor.

The exchanges of energy, water, and carbon between the terrestrial surface and the atmosphere directly link the atmospheric physical climate and the biogeochemical dynamics of terrestrial ecosystems. However, our understanding of the spatial and temporal dynamics of these exchanges, of the environmental controls on surface-atmosphere exchange processes, and of how surface-atmosphere exchange processes may change in response to natural and human-induced changes on the system is still limited for most of the Earth's ecosystems.[1,2] To develop and validate improved climate models, which in turn should lead to improved climate projections,[3] national and international programs, such as the U.S. Global Change Research Program (USGCRP) and the International Geosphere Biosphere Program (IGBP), have called for the development of improved data sets characterizing surface-atmosphere dynamics. It was the goal of this Phase II program to develop and test a new field flux sensor that can contribute to the generation of such high quality databases.

Turbulent transport of heat, mass, and momentum is a key process in biosphere-atmosphere interactions, regulating the transfer of CO_2 between the atmosphere and vegetation canopy, the dissipation of sensible heat from leaves to the atmosphere, and water loss from the surface by evapotranspiration. The magnitude of the turbulent transport effect is variable, and is dependent upon atmospheric and surface properties, such as wind speed and aerodynamic roughness defined by the surface and canopy configuration.

To address turbulent transport, aerodynamic approaches, such as eddy flux covariance, must be employed. Enclosed chamber measurements, although applicable to a wide variety of local scale objectives, cannot address turbulent transport issues and are subject to sampling bias due to spatial heterogeneity, as well as to temporal variabilities and potential disturbance to the surface exchange processes.[4] The eddy flux covariance technique is based on the premise that vertical flux densities between the surface and the atmosphere are proportional to the mean covariance between vertical velocity (w') and the respective scalar (c') fluctuations.[5-7] Eddy covariance observations represent the flux spatially integrated over areas on the order of 10^3 m^2 for tower-based studies. The eddy flux covariance technique represents one of the most direct means to obtain quantitative, non-intrusive measurements of flux from a surface source and requires no assumptions regarding exchange coefficients or eddy diffusivities as do other micrometeorological approaches.[8] The underlying physics and advantages of the eddy flux covariance technique have been widely discussed and the technique has been applied in numerous studies over the past decade over forests,[9-12] croplands,[13] and wetlands.[14,15]

Because of the relative lack of commercially-available fast-response sensors, most eddy covariance applications have been devoted to the measurement of CO_2, water vapor, heat and momentum using either closed- or open-path nondispersive infrared (NDIR) gas analyzers integrated with commercial micrometeorological instrumentation.[9,16-19] Commercially-available NDIR sensors can suffer from spectroscopic interferences (cross talk) (water vapor can lead to a spurious signal in the CO_2 channel and vice versa). They also require compensation for pressure broadening of the CO_2 absorption bands arising from water vapor. In addition, they require renewable chemicals used to scrub the reference channel of the measured component.

Several other sensor technologies are capable of making eddy covariance or flux gradient measurements. CH_4 and N_2O fluxes have been measured using gas chromatography (GC) and/or flame ionization detection (FID) or electron capture detection (ECD).[20] CH_4 and N_2O fluxes have also recently been measured using a Fourier transform IR (FTIR) spectrometer.[21] H_2O vapor fluxes have been measured with a fast response Kr or Lyman-α hygrometer.[19]

The advent of tunable diode lasers, in conjunction with the development of highly sensitive detection techniques for absorption measurements, has brought about the possibility for high precision, high-speed diode laser-based flux sensors. TDL-based flux sensors to date have generally been research prototypes and thus are personnel-intensive in operation, power consumptive, and expensive. The vast majority of systems have been based on mid-IR Pb salt diode lasers, which are difficult to use. Mid- or near-IR TDL systems have been used to measure fluxes of NH_3, N_2O, CO, and CH_4.[15,17,22-29] Widespread field deployment of mid-IR instruments has been hampered by the need for cryogenic cooling for the Pb salt laser and detector, and by instrument size and complexity. A typical, commercially available, mid-IR TDL flux sensor weighs 75 kg and uses extractive sampling with a closed path optical cell.[30] As a consequence of these issues, TDL instruments have not yet received wide acceptance in the micrometeorological community. The sensor we have demonstrated under this program will enable routine, reliable field use without sacrificing measurement precision or frequency response, and with minimal sampling losses.

The goal of this Phase II program was to develop the next generation diode laser-based flux sensor by taking advantage of advances in near-infrared tunable diode lasers and in high sensitivity detection techniques. The development of room temperature-operable tunable diode lasers in the near infrared by the telecommunications industry has resulted in lasers that are economical, very compact, rugged, efficient, reliable, and long-lived. In contrast to previous laser sensors that use frequency modulation (FM) detection techniques, our sensor uses a balanced ratiometric detection (BRD) technique. The high degree of noise quieting provided by the BRD results in high measurement precision. The BRD also has a fast temporal response, with a readily achievable measurement rate of 20 Hz or better. The BRD-line scanned technique has several advantages including high chemical specificity and independence from pressure effects. A TDL-based sensor, using near-IR diode lasers coupled with the BRD, possesses the requisite sensitivity and precision, as well as the temporal response, to measure fluxes of CO_2 and several other important trace gases via eddy covariance.

Near-infrared diode lasers, in combination with PSI's BRD technology, are the fundamental technologies with which a new generation of high precision flux sensors can be realized. This new sensor utilizes a compact, open optical path for *in situ* sensing. Thus concerns about loss of high frequency response and about wall losses inherent with extractive sampling are avoided.[31] CO_2 and H_2O are measured simultaneously. Simultaneous measurement of water vapor is important so that corrections to CO_2 fluxes due to air density fluctuations caused by temperature and water vapor density fluctuations can be performed.[32] Indeed, we have shown that, since we make high speed measurements of H_2O simultaneously with the wind and CO_2 measurements, we can calculate the instantaneous mixing ratio of CO_2 in dry air so that these corrections are no longer necessary. The Phase I program developed and successfully demonstrated the open optical probe and also demonstrated the precision and temporal response required for flux measurements. The Phase I program concluded with a conceptual design for an integrated eddy covariance flux sensor. The Phase II program fabricated the integrated sensor and successfully field-tested it.

2. Ultrasensitive Absorption Spectroscopy

Our sensor is based on the quantitative absorption of a near-IR diode laser beam propagating through an air sample. Because of the fingerprint nature of the infrared spectral region, an isolated absorption feature, free of interference from absorption by other species, can always be found. The measurement of small optical absorbances is limited by excess laser amplitude noise. Absorption measurements below ~1 part in 10^3 require low-noise detection schemes. Over the past 8 years, PSI has developed the balanced ratiometric detection technique for this purpose. The balanced ratiometric detector (BRD) employs a novel electronic noise canceling technique first demonstrated at IBM.[33] The BRD is a dual beam technique. The diode laser beam is split into reference and signal beams. The signal beam propagates through the absorbing gas while the reference beam propagates through an optical fiber. Cancellation of excess noise is achieved by balancing the photocurrents from each of the photodiodes. This balance is achieved electronically with the BRD. Common mode excess laser noise in the signal and reference channels is reduced by more than 50 dB, or 5 orders of magnitude. Noise reduction to the shot-noise limit has been demonstrated both by Hobbs and coworkers[33] and by PSI.[34] In the limit of weak absorbance, the BRD provides an output signal that is directly proportional to the absorbance and, therefore, to the absorbing species number density. The BRD affords a simple electronic detection technique. No high frequency bandwidth components are required. The technique provides direct measurement of the absorption lineshape, resulting in measurements that are insensitive to pressure variations.

3. Eddy Flux Covariance Measurements and Sensor Resolution

We have developed values for the measurement precision required for flux measurements based on the definition of chemical resolution proposed by Businger and Delany.[35] The required precision scales directly as the magnitude of the flux. The chemical resolution, R (g/m^3, or mixing ratio), required to measure the flux of species C, F_c (g/m^2/s), is:[35]

$$R = 0.1 * |F_c| * AP \tag{1}$$

The atmospheric parameter, AP (s/m), is a function of the friction velocity, u_*, and the scaled potential temperature, θ_*. The Atmospheric Parameter is given by:

$$AP = \frac{\sigma_\theta}{u_* |\theta_*|} \tag{2}$$

The potential temperature,

$$\theta = T\left(\frac{P_o}{P}\right)^{0.286} \tag{3}$$

where P_o is a reference pressure usually = 100 kPa. The potential virtual temperature, $\theta_v = \theta(1+0.61r)$, where r is the water vapor mixing ratio. Finally, the scaled potential temperature,

$$\theta_* = \frac{-\overline{w'\theta'}}{u_*} \tag{4}$$

Here, σ_θ is the standard deviation of θ. In addition, $\overline{w'\theta'}$ is the vertical turbulent heat flux. For typical atmospheric conditions, AP falls within the range: $3.5 \leq AP \leq 10$ s/m.[35] The relationship between AP and F_c is plotted in Figure 1. As an example, given an AP of 6 s/m and a typical flux of 10^{-3} g/m^2/s,[36] the required resolution is 600 µg CO_2/m^3 or 330 ppbv CO_2 at 296 K and 1 atm. The ratio of the chemical resolution to the ambient concentration is the required measurement precision. For CO_2, the required precision is ~ 0.1%; for water vapor, it is ~1%. Table 1 presents the required chemical resolutions for CO_2 and H_2O for example fluxes.

We have demonstrated the sensitivity of our technique for CO_2 during the Phase I program. We found our sensitivity for CO_2 to be 670 ppbv-m, as shown in Table 1 (this corresponds to a minimum measurable absorbance of 1 x 10^{-5}, which we have found to be routinely achievable value in laboratory and field instruments using the BRD). The optical pathlength required to achieve a resolution of 330 ppbv is simply the ratio of the sensitivity to the resolution. This ratio indicates that the resolution can be achieved with a path of 2 m. The required resolution for H_2O can be easily achieved with a 2 m path. Thus, CO_2 and H_2O can be measured over relatively small path lengths. This small optical pathlength greatly facilitates making eddy covariance flux measurements, as it leads to an extremely compact air probe design. The optical path can be folded within a much smaller physical pathlength.

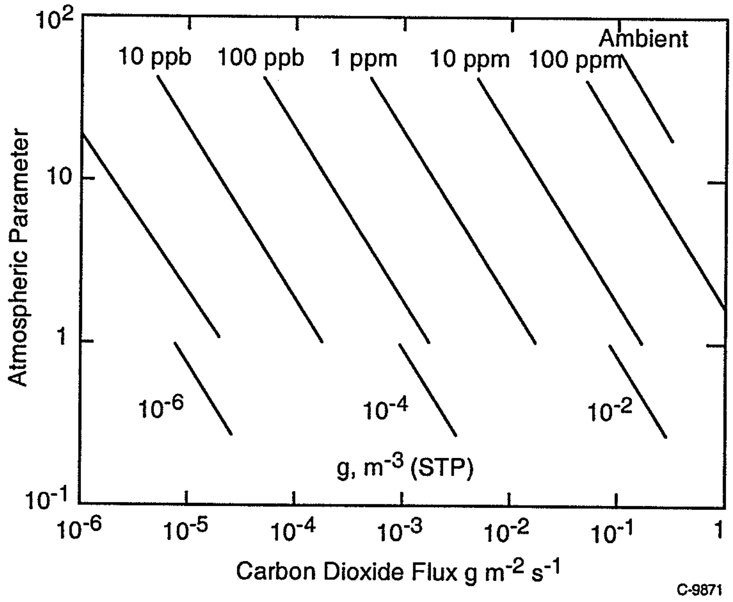

Figure 1. Plot of atmospheric parameter, AP, vs CO_2 flux, following Ref. 35.

Table 1. Chemical Resolution Required for Flux Measurement via Eddy Covariance

Species	Mixing Ratio[a] [ppmv]	Peak Absorbance[b]	Flux [g m^{-2} s^{-1}]	Required Resolution[c] [ppbv]	Demonstrated Sensitivity[d] [ppbv-m]	Required Path [m]
CO_2	30	4.9×10^{-3} *2.004 μm*	10^{-3}	330	670	2
H_2O	7730[e]	3.8×10^{-3} *1.994 μm*	10^{-1}	75000	20000	0.3

a) US Standard Atmosphere.
b) Peak absorbance of ambient concentration at indicated wavelength, 1 m path, 296 K.
c) Calculated for an atmospheric parameter of 6 s/m.
d) Minimum absorbance of 1 x 10^{-5}, 0.1 s average.
e) Represents 28% relative humidity at 296 K.

Recently summarized exchange rates vary between ~0.2 to 2.0 mg $CO_2/m^2/s$ for a variety of ecosystems.[36] These rates are presented in Table 2. Based on our sensitivity and the above development, the optical paths needed to measure fluxes of these magnitudes are 10 and 2 m respectively, given the desire to maintain a 10 Hz measurement rate. As we discuss below, we desire to use a physical pathlength of 0.25 m; a folded optical path of 2 or 10 m can be created with 8 or 40 passes respectively. Such folded path optical cells are easily fabricated. The range of measurable CO_2 flux can be extended both by temporal averaging and by increasing the optical path. A measurement rate faster than 1 Hz is necessary to preserve sensitivity to high frequency flux components. This limits the amount of temporal averaging. As an example, a flux of 7 x 10^{-5} g $CO_2/m^2/s$ should be measurable for a 1 Hz measurement rate and a 10 m path. Thus, by careful design, our sensor can monitor the typically encountered range of fluxes for a variety of ecosystems.

Table 2. Summary of Net Ecosystem Fluxes for CO_2

Vegetation Type	Max Net Ecosystem Assimilation, A_{smax} (gm $CO_2/m^2/s$)	Max Ecosystem Respiration, R_{smax} (gm $CO_2/m^2/s$)
Tundra	2.9 x 10^{-4}	-2.2 x 10^{-4}
Salt marsh	7.2 x 10^{-4}	-1.9 x 10^{-4}
Tropical savanna	5.2 x 10^{-4}	-1.4 x 10^{-4}
Temperature C_4 grassland	8.9 x 10^{-4}	-2.1 x 10^{-4}
Temperature C_3 grassland	6.8 x 10^{-4}	-2.8 x 10^{-4}
C_4 crops	1.7 x 10^{-3}	-3.7 x 10^{-4}
C_3 crops	1.4 x 10^{-3}	-1.5 x 10^{-4}
Tropical rainforests	7.4 x 10^{-4}	-2.7 x 10^{-4}
Deciduous forest		
broadleaf	1.0 x 10^{-3}	-2.7 x 10^{-4}
needleleaf	2.6 x 10^{-4}	-2.0 x 10^{-4}
Evergreen forest		
needleleaf	6.9 x 10^{-4}	-1.3 x 10^{-4}
broadleaf	8.8 x 10^{-4}	-1.2 x 10^{-4}

N. Bachmann and E.D. Schultz, "Net CO_2 and H_2O fluxes of terrestrial ecosystems," *Global Biogeochemical Cycles*, 13, 751, 1999.

4. Absorption Spectroscopy Background

This program developed and field demonstrated a near-IR tunable diode laser absorption spectrometer for boundary layer flux measurements of CO_2 and H_2O above a forest canopy. The laser sensor makes high-speed measurements of the concentrations of each of these species. When combined with wind speed measurements from a sonic anemometer, this data yields the flux of each species via the eddy flux covariance technique. The laser spectrometer was designed to monitor $^{12}CO_2$ using one of several lines in the $2\nu_1 + \nu_3$ combination band near 2.01 μm (The HITRAN notation for the absorption band is 00001→20012).[37] The spectrum is presented in Figure 2. For the initial field trials during August 2001, we used the R36 line at 5001.5 cm^{-1} (1.9994 μm) for the $^{12}CO_2$ measurement (see Figure 3). This is not the strongest line in the band, as can be seen from the figure. After the end of the first field demonstration, we were able to purchase new lasers that could access the stronger lines (R16 and R18) near the peak of the Boltzmann distribution. These devices were incorporated into the sensor over the winter of 2001/2002. For the second field trials during July 2002, we used the R16 line at 4990.0 cm^{-1} (2.004 μm) for the $^{12}CO_2$ measurement (see Figure 4).

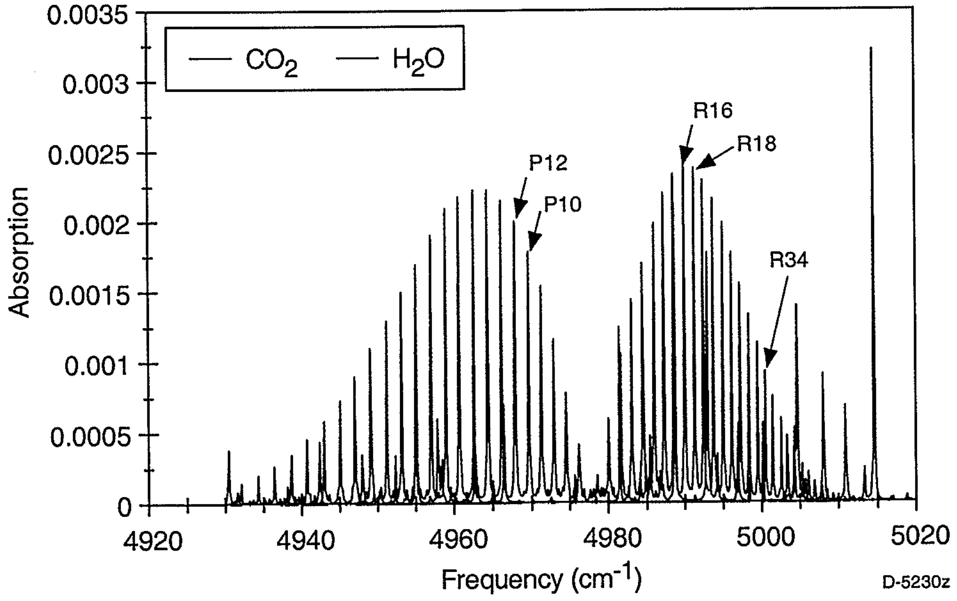

Figure 2. Calculated spectrum of the $2\nu_1 + \nu_3$ combination band (00001→20012) of $^{12}CO_2$. Modeled for 333 ppmv CO_2/N_2, 2 m path, 28% relative humidity, 296 K, and 1 atm.

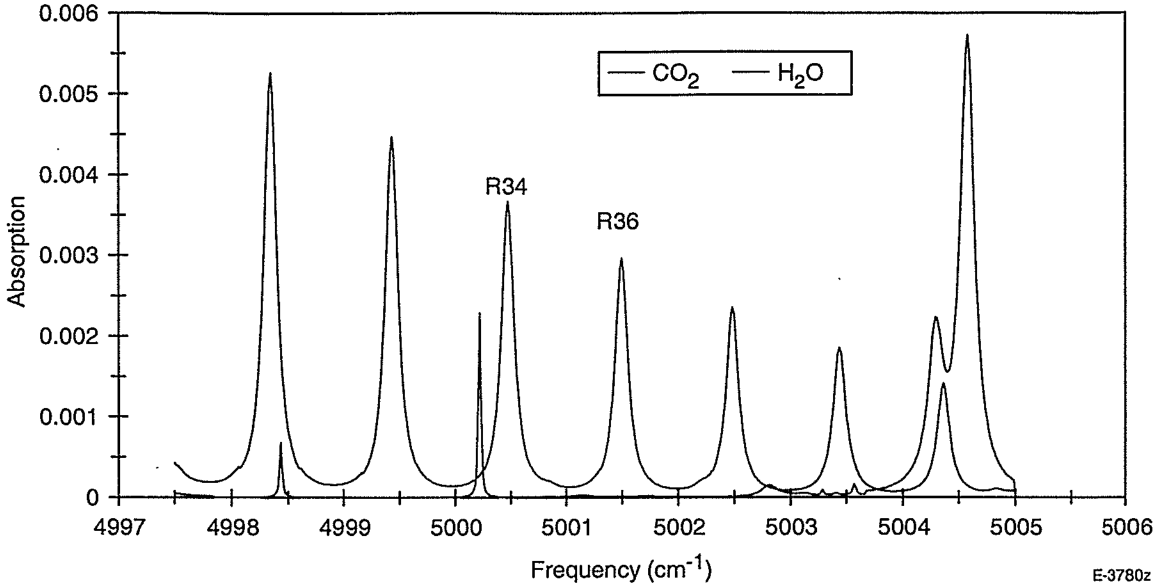

Figure 3. Calculated spectrum of the region surrounding the R36 line of the $2\nu_1 + \nu_3$ band (00001→20012) of CO_2. Modeled for 333 ppmv CO_2/N_2, 2 m path, 28% relative humidity, 296 K, and 1 atm.

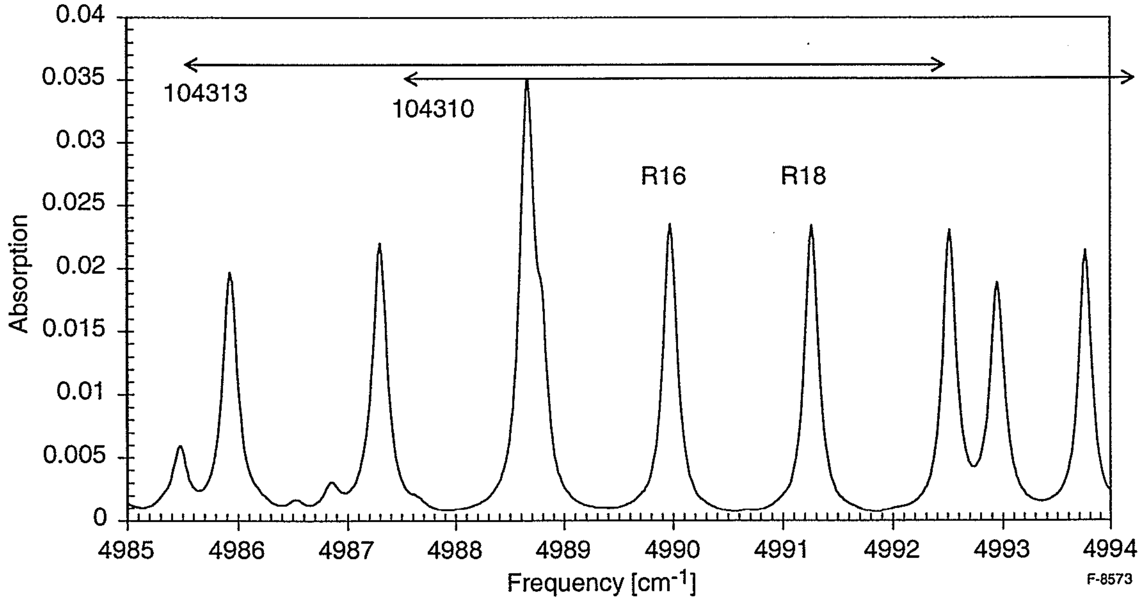

Figure 4. Calculated spectrum of the region surrounding the R16 line of the $2\nu_1 + \nu_3$ band (00001→20012) of CO_2. Modeled for 333 ppmv CO_2/N_2, 5 m path, 28% relative humidity, 296 K, and 1 atm. Also shown are the wavelength ranges accessible by temperature tuning the available lasers, designated by their serial numbers.

It is possible to develop a strategy for monitoring $^{13}CO_2$ in this spectral region and we devoted a small amount of program resources to develop this capability. The pertinent bands of $^{13}CO_2$ and $^{12}CO_2$ are shown in Figure 5. The preferred region for monitoring $^{13}CO_2$ lies in the R branch of the $2\nu_1 + \nu_3$ band (00001→20012) near 4900 cm^{-1} (2.04 μm). Specifically, the R22 transition at 2.0394 μm is a prime candidate as illustrated in Figure 6. We were only able to procure a laser that could access this region near the very end of the program. During the second field demonstration, we did use an existing 2 μm laser, previously used for the $^{12}CO_2$ measurements during the first deployment, to access the R branch of the (00001→20011) band near 5007 cm^{-1} (1.997 μm). This was possible by temperature tuning the device to achieve the necessary wavelength. Higher resolution calculated spectra are provided in Figures 7 and 8. These figures show the $^{12}CO_2$ R48 line at 5007.0 cm^{-1} and the $^{13}CO_2$ R22 line at 5007.35 cm^{-1} that were monitored simultaneously in a single laser sweep during the second field demonstration. The disadvantage on monitoring $^{13}CO_2$ in this region is that both these lines are weak, thus requiring longer pathlengths, and they ride on the wing of a strong neighboring water line. However, the R22 line was the only line accessible with available lasers.

Water was monitored on the feature near 7185.5 cm^{-1}, as shown in Figure 9. This is a relatively strong line, and with the relatively large ambient mixing ratios expected in summer, strong peak absorptions can be obtained using short pathlengths.

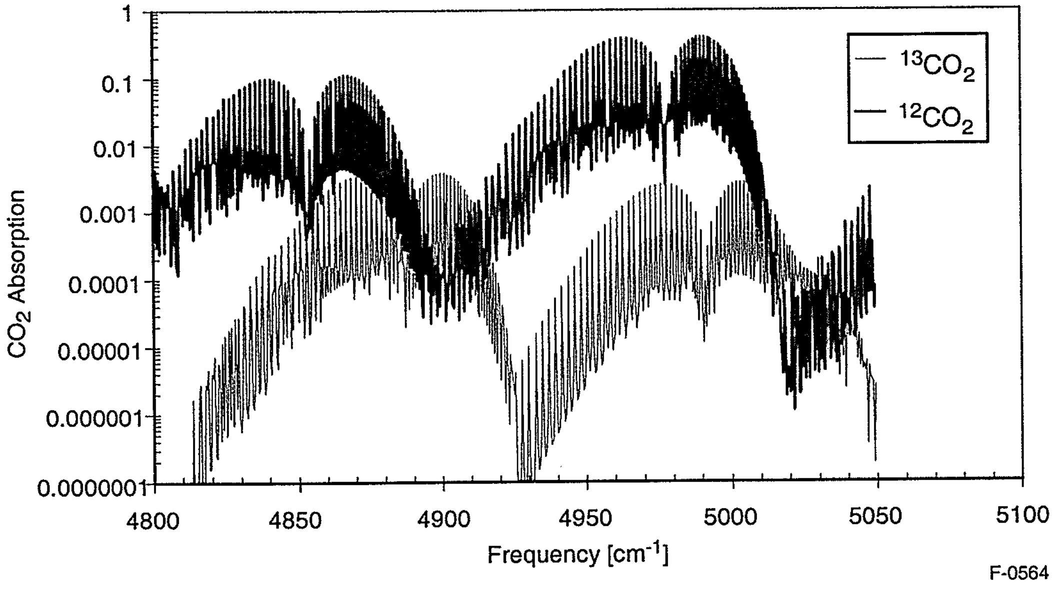

Figure 5. Calculated spectrum of the $2\nu_1 + \nu_3$ combination bands of $^{12}CO_2$ and $^{13}CO_2$. Modeled for 333 ppmv CO_2/N_2, 100 m path, 28% relative humidity, 296 K, and 1 atm.

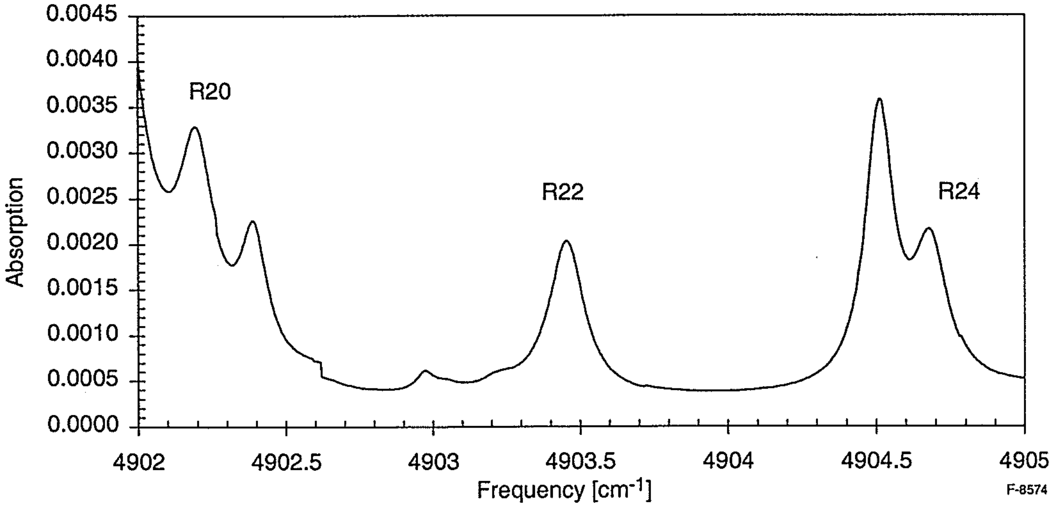

Figure 6. Calculated spectrum of the R22 line of the $2\nu_1 + \nu_3$ combination band (00001→20012) of $^{13}CO_2$. Modeled for 330 ppmv CO_2/N_2, 50 m path, 28% relative humidity, 296 K, 1 atm, and natural abundance. All unlabeled major features are H_2O.

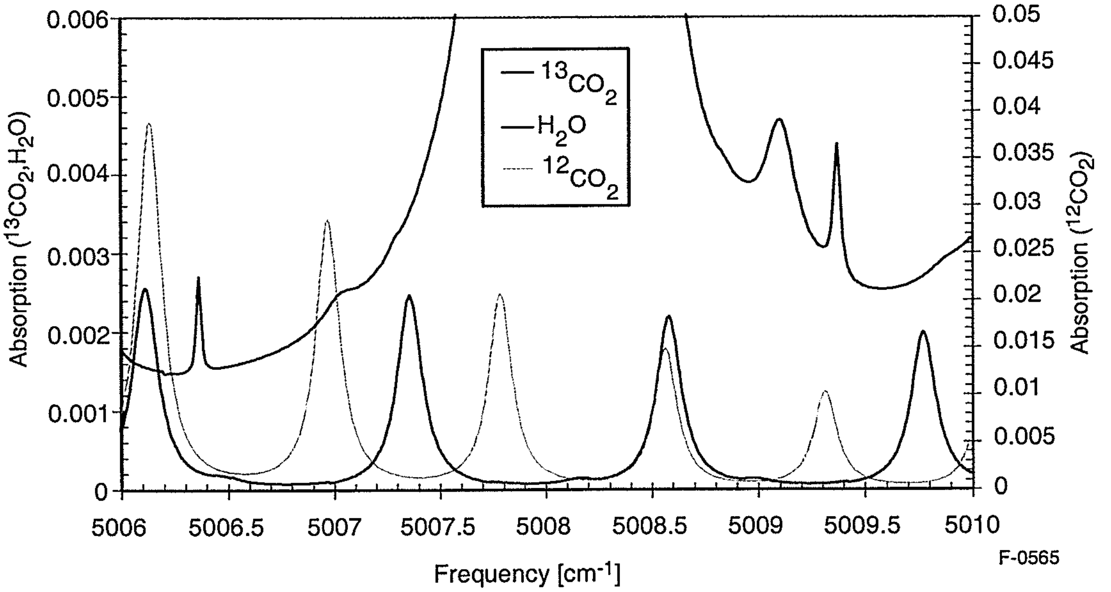

Figure 7. Calculated spectrum of the R22 line of the $2\nu_1 + \nu_3$ combination band (00001→20011) of $^{13}CO_2$ and the R48 line of the $2\nu_1 + \nu_3$ combination band of $^{12}CO_2$. Modeled for 333 ppmv CO_2/N_2, 100 m path, 28% relative humidity, 296 K, 1 atm, and natural abundance.

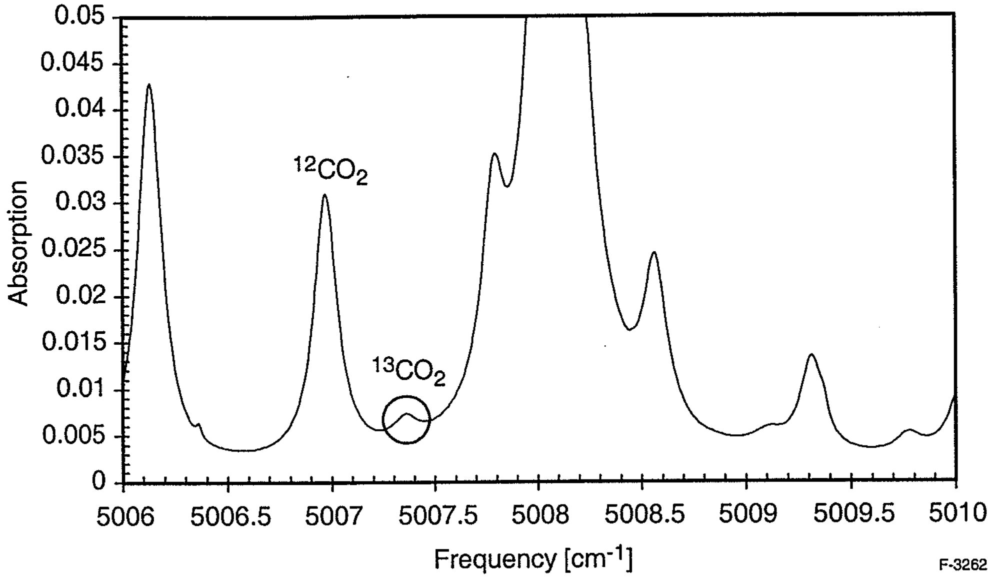

Figure 8. Calculated spectrum of the R22 line of the $2\nu_1 + \nu_3$ combination band (00001→20011) of $^{13}CO_2$ and the R48 line of the $2\nu_1 + \nu_3$ combination band of $^{12}CO_2$. Modeled for 333 ppmv CO_2/N_2, 100 m path, 28% relative humidity, 296 K, 1 atm, and natural abundance.

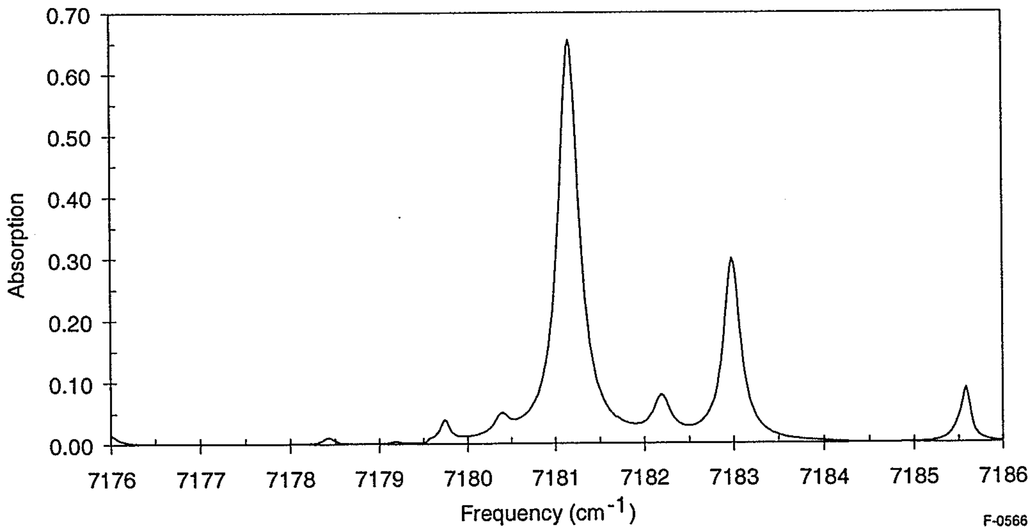

Figure 9. Calculated spectrum of lines of the $\nu_1 + \nu_3$ combination band of H_2O. The target line is at 7185.5 cm^{-1}. Modeled for 7750 ppmv H_2O/N_2, 1 m path, 28% relative humidity, 296 K, and 1 atm.

5. General Diode Laser Absorption Spectrometer

A schematic diagram of a general diode laser-based absorption spectrometer is presented in Figure 10. The laser is tuned, via temperature, to an absorption transition of CO_2 in the $2\nu_1 + \nu_3$ combination band near 2 μm and scanned across the absorption feature by modulating the laser injection current at 500 Hz. The output of the laser, which is coupled into a single mode fiber, is split into two legs using a single mode, fused 1 x 2 fiber splitter. One of the output legs, the signal leg, is directed to the *in situ* air probe via a fiber optic cable. The signal beam is launched into the measurement cell using a fiber-coupled collimator, it then reflects between the two mirrors that define the multipass cell, and finally it exits the far mirror via a slot and impinges on a large area extended response InGaAs photodiode. The signal photocurrent is directed to the signal input channel of the balanced ratiometric detector (BRD). The remaining output leg of the splitter is routed to the reference input of the BRD. The amplified and filtered output of the BRD is digitized by a computer-based data acquisition system.

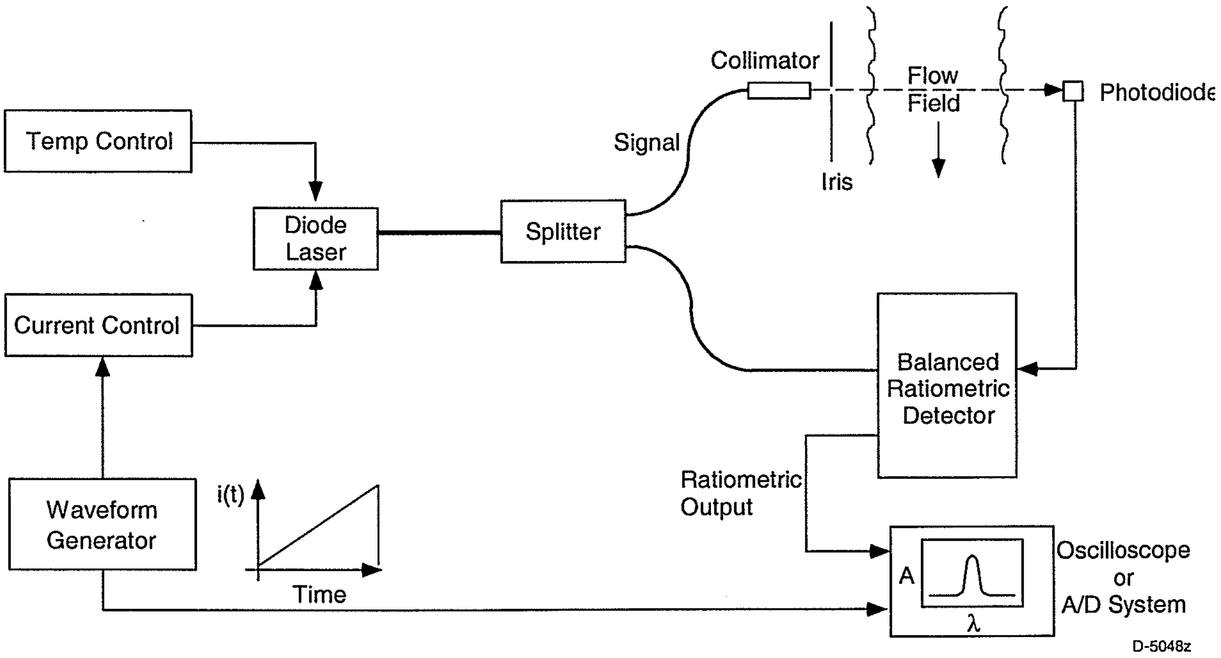

Figure 10. General schematic of a tunable diode laser absorption spectrometer.

One of the main advantages of the fiber-coupled near-IR diode laser sensor is that the laser and electronic systems can be deployed remotely from the measurement location. This allows true, *in situ* measurement of CO_2 and water vapor via the open path optical measurement cells. Most of the electronic components are consolidated into a compact, rugged enclosure, termed the sensor processor module (SPM) that is deployed in an environmentally controlled housing at the foot of the measurement tower. The cells and ancillary sensors are mounted on a boom at the top of the tower. One fiber optic and several electronic cables lead from the SPM to the air measurement cells. Figure 11 depicts the general field deployment architecture.

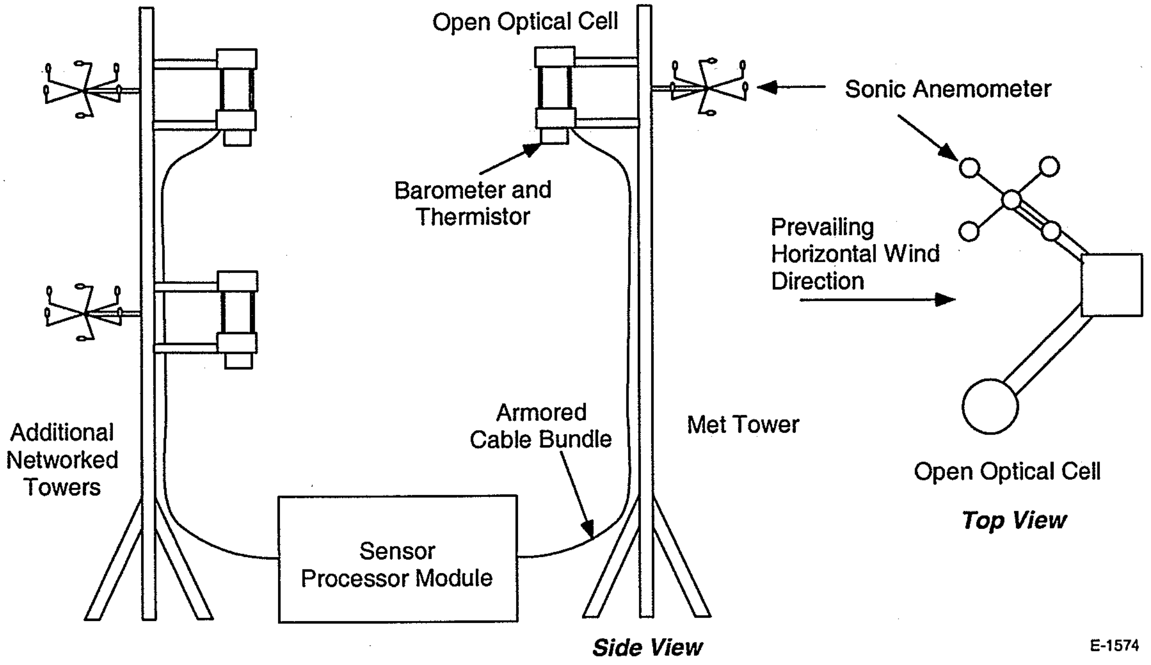

Figure 11. General schematic of sensor deployment.

5.1 Sensor Processor Module

A functional diagram for the SPM is shown in Figure 12. The main components of the SPM are: 1) a single board computer with a Pentium III 800 MHz processor and a PCI bus, 2) high speed multifunction data acquisition boards, 3) laser controller, 4) diode laser and fiber optic splitter, 4) BRD, 5) ethernet communications board, and 6) mass storage device (hard disk drive).

The single board computer executes the signal processing algorithms to calculate species concentrations from the digitized BRD signals, monitors the health of the individual systems, and sends and receives data over the serial communications bus. The data acquisition board provides a modulation input to the laser controller, monitors laser operation and health, and digitizes the BRD signals. The laser controller stabilizes the diode laser temperature and provides a low noise current source for modulation. The Ethernet board provides a communication link over which system diagnostics and data downloads to the remote laptop station are performed. The remote laptop takes the high-speed CO_2 and H_2O concentration measurements from the laser sensor, along with the wind speed measurements from the sonic anemometer to calculate fluxes of both species. It then calculates 30-min averages.

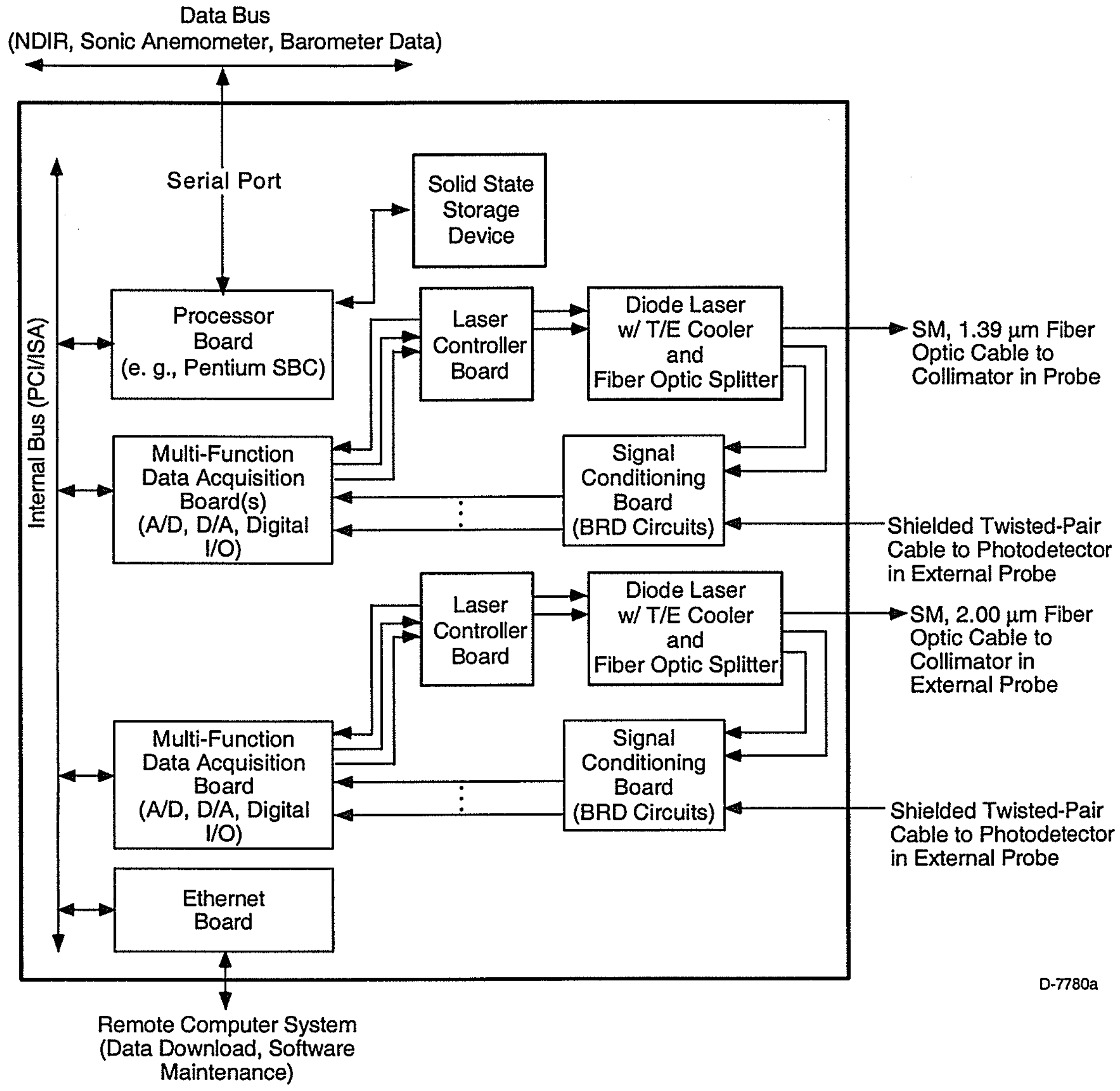

Figure 12. Functional diagram for the sensor processor module. Only two of the three laser channels are illustrated.

The SPM enclosure was specifically designed to house all the major components compactly in a rugged package that was single man portable. We chose to use OEM cabinetry components that allow for flexible design. An aluminum chassis is used for mounting all the components. The chassis sits inside a plastic outer case. An isometric assembly view of the enclosure is presented in Figure 13. Another view with the outer cover removed is shown in Figure 14. The chassis is divided into upper and low bays. The upper bay houses the system power supplies, single board computer and data acquisition cards, the junction board, and the BRD detector. The lower bay is divided into three sections, each of which houses an integrated laser carrier. Each carrier contains a laser controller, laser and mount, and fiber optic splitter. The laser carrier is shown in Figure 15.

Figure 13. Isometric view of SPM.

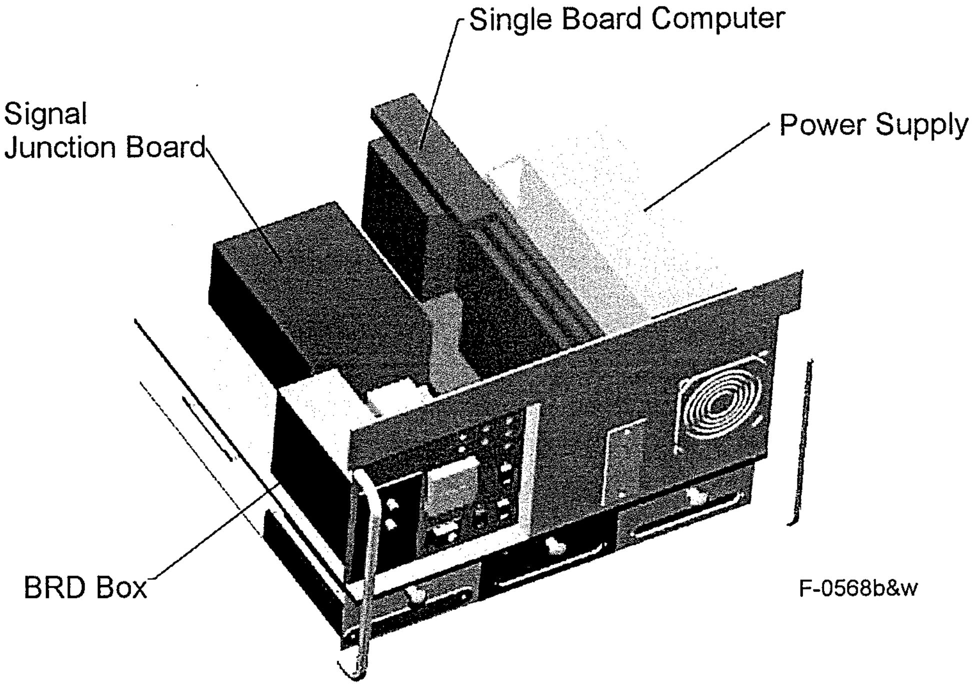

Figure 14. Isometric view of SPM with cover removed.

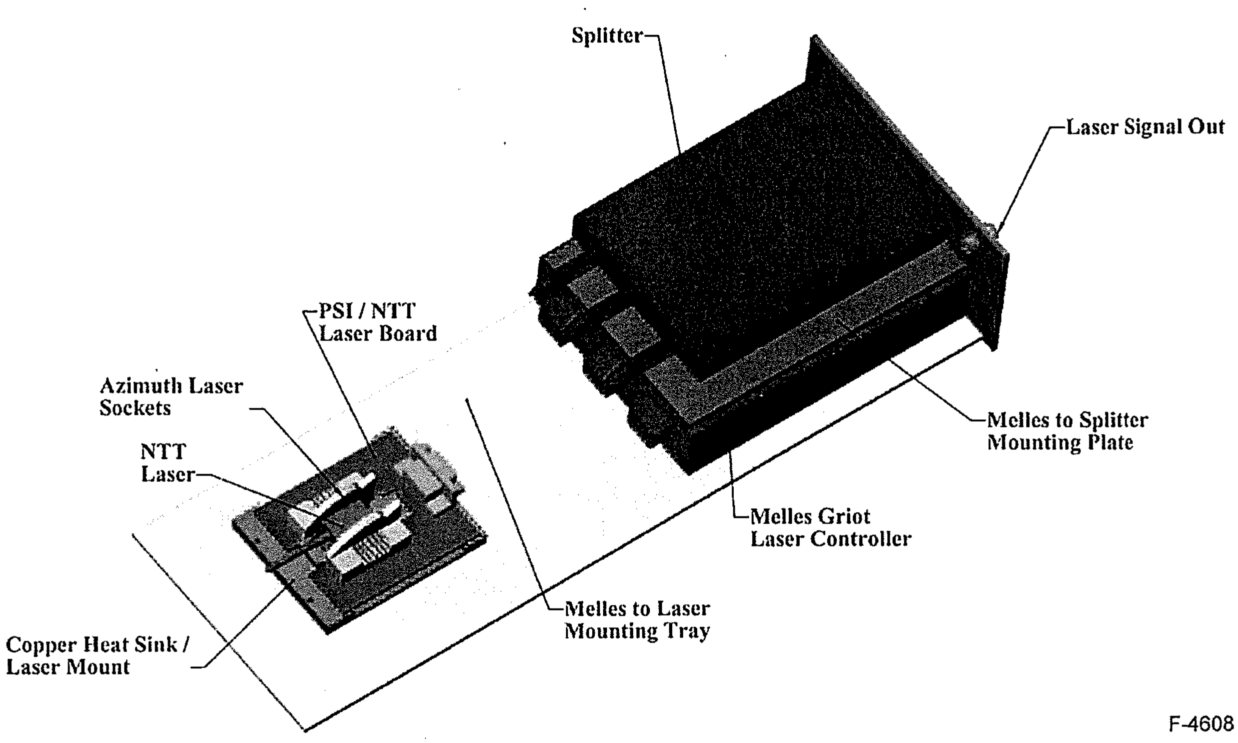

Figure 15. Isometric view of laser carrier.

The user interface panel is shown in Figure 16. The panel provides the user with access to various controls and connectors. While AC line power is connected and switched at the rear of the chassis, the DC power is switched on the interface panel. An array of LEDs indicates proper function of each of the AC/DC converters. The BRD unit is accessible via this panel and the photodiode input connectors are directly accessible. Also on this panel are connectors for the Ethernet link, as well as inputs for the barometer, sonic anemometer, and Li-Cor NDIR analyzer signals. Finally, there is a reset button for the computer. Connections for video and keyboard are provided behind a small panel to the right of the interface panel. These allow the operator to set up and run the system locally. A shipping panel is provided to cover the interface panel during transport.

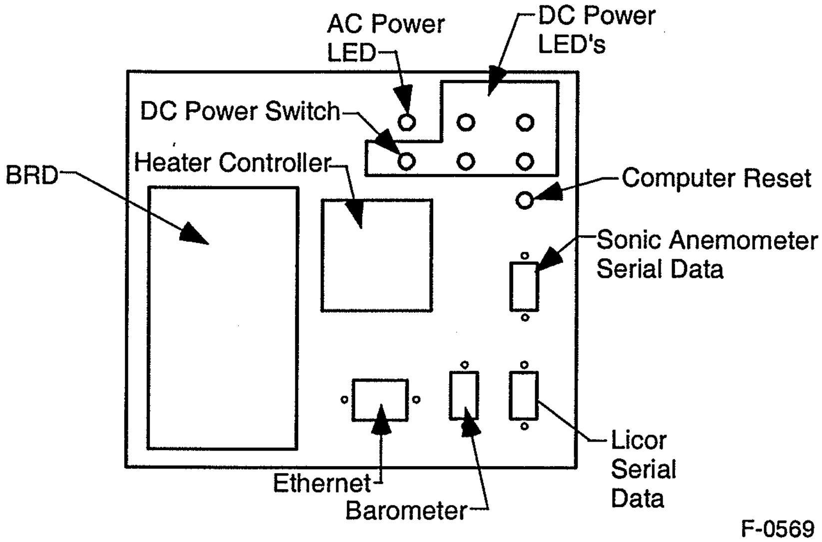

Figure 16. User interface panel of SPM.

In order to achieve the most compact footprint for the SPM, we designed and fabricated a custom printed circuit signal junction board. This board acts to route signals between the computer and the laser controllers, the data acquisition cards, and on-board temperature monitors. A schematic diagram of the junction board is provided in Figure 17; the board layout is provided in Figure 18.

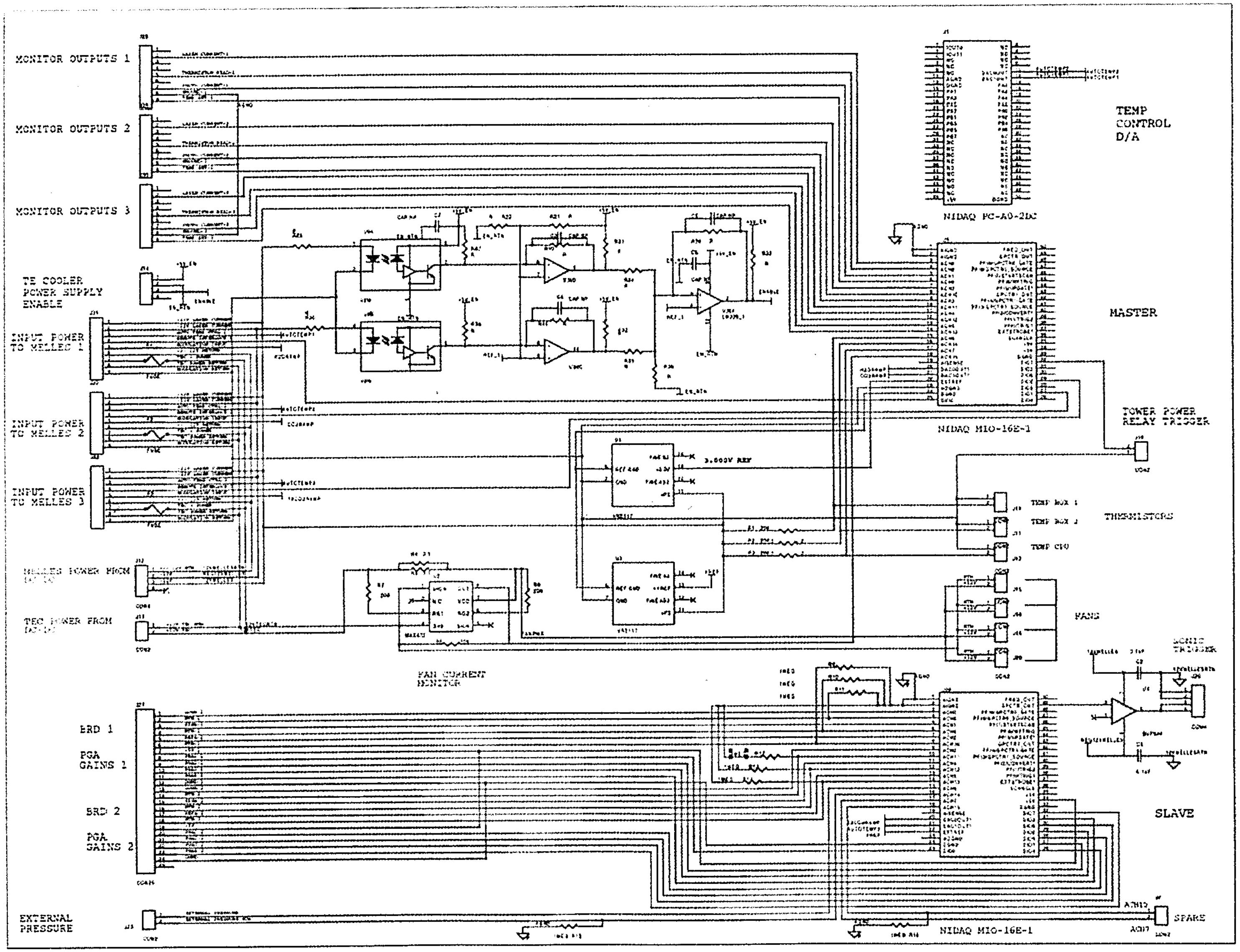

F-0570

Figure 17. Circuit diagram of custom junction pc board.

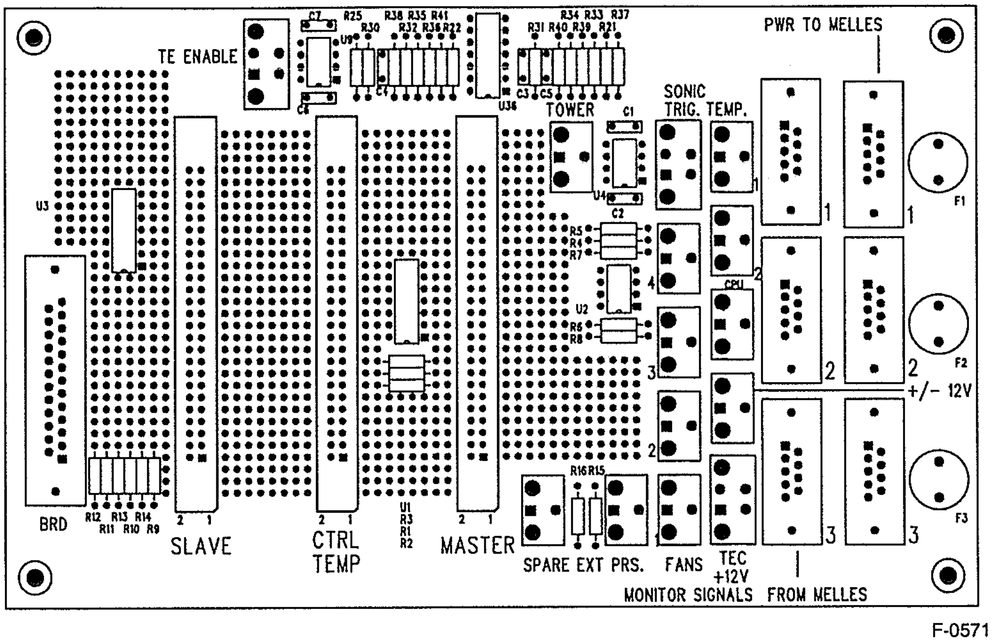

Figure 18. Layout of custom junction pc board.

The size, weight, and power of the integrated SPM are listed in Table 3.

Table 3. SPM Physical Parameters

Parameter	Value
Size	37 x 54 x 45 (h x w x d) cm
Weight	25 kg (with three lasers)
Power	<200 W at 110 VAC

5.2 In Situ Air Probe – Open Path Optical Multipass Cells

The *in situ* air probes were designed for making boundary layer eddy flux covariance measurements from a tower above a forest canopy. Several basic criteria arising from this application were followed in the design of these probes. These criteria were:

- The probe is an open path, *in situ* design. This alleviates concerns over loss of response to high frequency eddies and wall losses inherent with extractive sampling.

- The probe must be compact and symmetric in design. This minimizes concern over perturbation of the airflow and undersampling of high frequency eddies.[38]
  - The expected wind speeds and measurement rate determine the maximum size of the probe.

  - The compact size of the probe allows close coupling to the sonic anemometer, ensuring correlated measurements of an air parcel.
  - The absorption signal strength, desired precision, and expected flux magnitude determine the optical path length. An optical multipass cell is used to provide an extended optical pathlength in a compact physical footprint, maintaining small probe size.

- The probe must be stable to temperature and humidity excursions.
  - We specified low thermal expansion coefficient materials.

- The probe must be stable to mechanically and turbulence induced vibration.

We designed and fabricated probes of two different sizes. A small cell with an optical path of a few meters was designed to measure $^{12}CO_2$ or H_2O. A large cell with an optical path of a few tens of meters was designed to measure $^{13}CO_2$, which reflects the natural abundance of ~1.1% ^{13}C. The probes share general design features. Each probe has one fixed and one adjustable mirror. The small cell has 2.5 cm diameter mirrors of 15 cm focal length separated by 25 cm. The large cell has 5 cm diameter mirrors of 30 cm focal length separated by 50 cm. The mirrors are custom-fabricated, gold-coated metal substrates with a HfO_2 protective overcoat. Narrow radial slots in the mirrors allow passage of the laser beam into or out of the cell. Based on the experience gained in the Phase I program, the width of the slots was increased in the new mirror sets. Figure 19 illustrates the general design of the cell. The small cell is pictured. The main (bottom) flange supports the fixed launch mirror and the optical bench for the launch optics. The optical bench is pictured in Figure 20. The fiber coupled laser beam is launched through a slot in the front mirror into the cell using a pigtailed collimator. The collimator was designed to provide a focal spot of < 700 μm at 50 cm. A lightweight aluminum box protects the optics. The beam passes between the two mirrors for the required number of passes then exits through a slot in the exit mirror at the top of the cell. The exit mirror is gimbaled for easy alignment. It can also be moved relative to the bottom mirror to tune the separation. The exiting beam impinges on a photodiode that is housed inside a protective can. A cross-sectional view of the detector region is provided in Figure 21. The entire multipass region can be enclosed with a separate aluminum can for calibration using precision gas mixtures (Figure 22).

Measurement of $^{12}CO_2$ with the necessary precision requires a pathlength of only a few meters. Thus, a multipass cell with an 0.25 m base path required only a few bounces to achieve this pathlength. For example, for the second deployment, with an 0.25 m separation and 15 passes, the total optical pathlength of the small cell was 3.8 m. This provided a 2% peak absorption on the R16 absorption line. The calculated spot patterns for the launch and receive mirrors are presented in Figure 23(a) and (b).

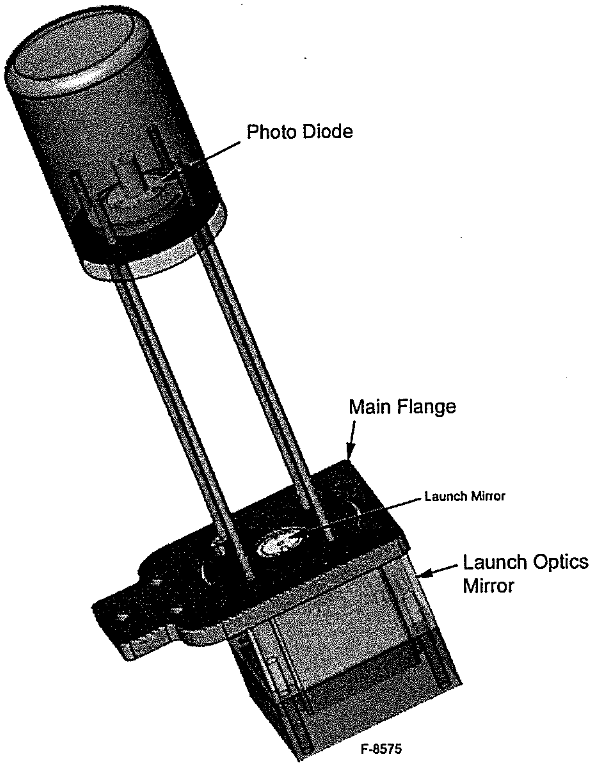

Figure 19. Schematic of small open path cell.

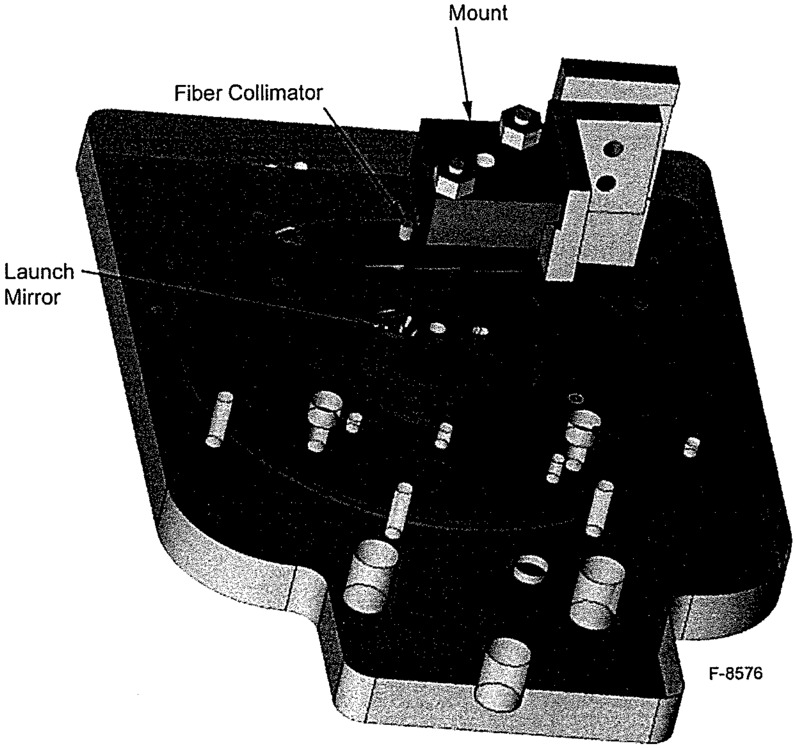

Figure 20. Schematic of optical bench.

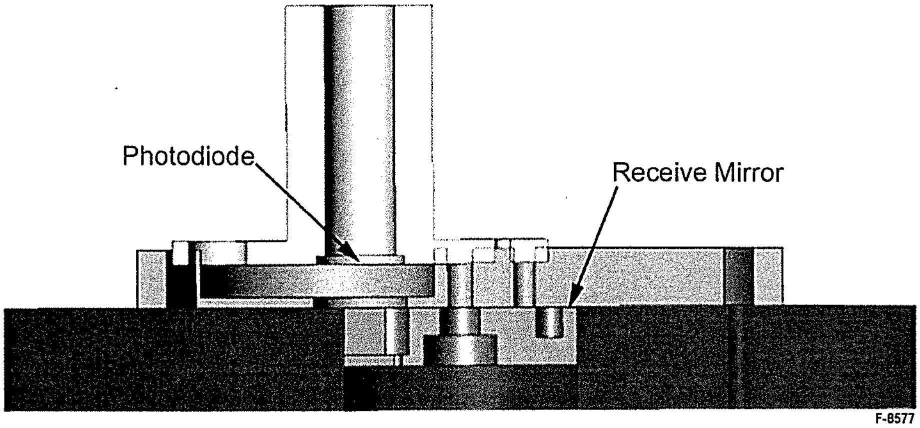

Figure 21. Cross section of detector region.

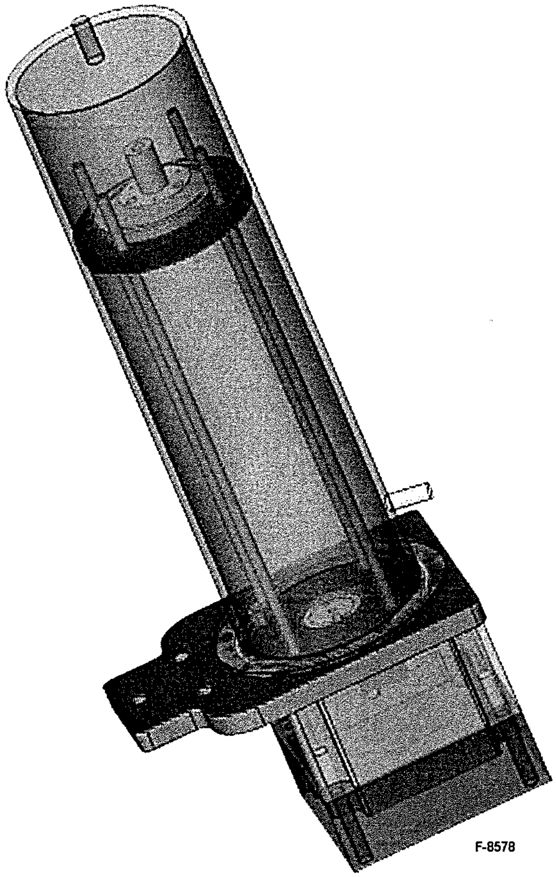

Figure 22. Schematic of small cell with calibration can.

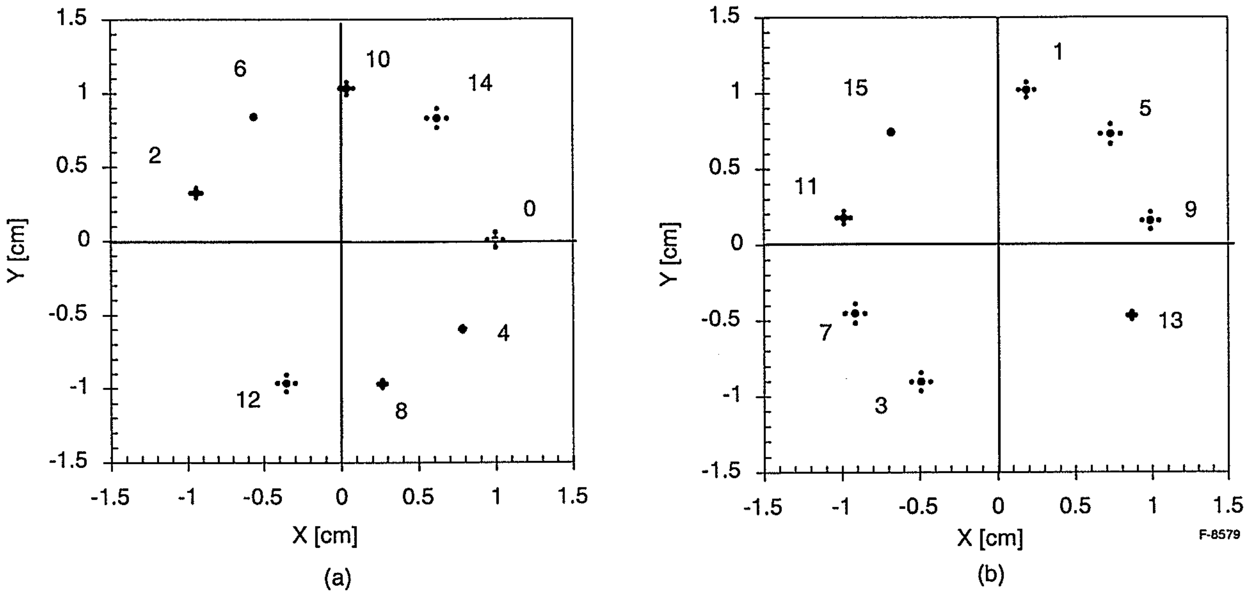

(a) (b)

Figure 23. Calculated spot patterns for the (a) launch mirror and (b) receive mirror of the small cell. Mirror separation was 0.25 m, 15 passes, 3.8 m total optical path. The launch spot (#0) is green and the exit spot (#15) is red. The calculated spot size is indicative of the actual beam spot size.

Measurement of $^{13}CO_2$ with the necessary precision requires a much longer pathlength, on the order of 100 m. Thus, the large cell was designed with a 0.5 m mirror separation and tens of bounces. The large mirror set was designed to space the spots around the circumference of the mirror without overlap. This could only be done easily with larger diameter mirrors. Thus 50 cm mirrors were chosen. The calculated spot pattern for the launch side mirror is presented in Figure 24. During the second deployment, with an 0.50 m separation and 69 passes, the total optical pathlength of the large cell was 34.5 m. This provided an 0.09% peak absorption on the R22 $^{13}CO_2$ absorption line.

We did design windows to protect the lower mirrors. A 3 mm thick, sapphire window sits on top of the mirror as shown in Figure 25 to provide protection from the elements. The window is antireflection coated. We were not able to identify a vendor willing to ar coat the windows, so they were not procured or used during our field deployments.

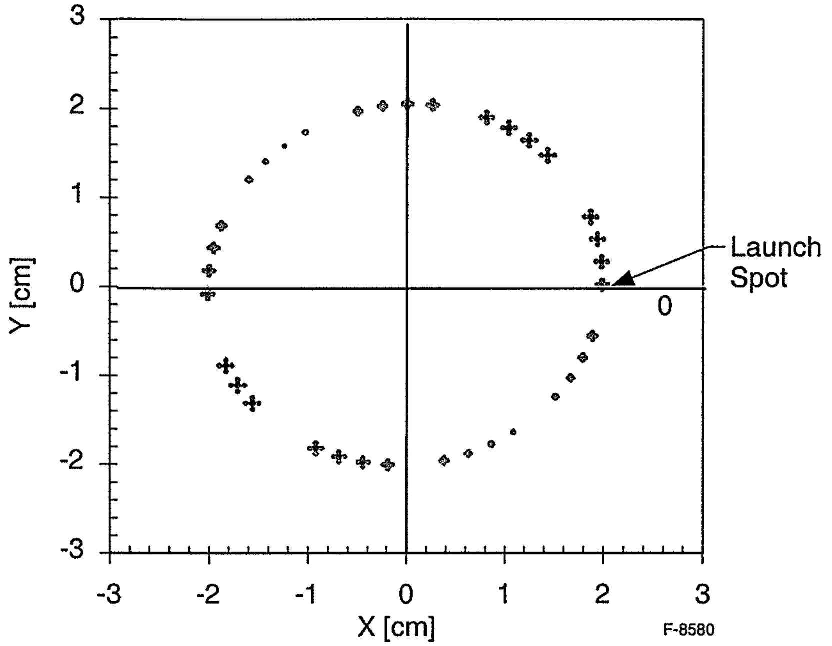

Figure 24. Calculated spot pattern for the launch mirror of the large cell. Mirror separation was 0.50 m, 69 passes, 34.5 m total optical path. The calculated spot size is indicative of the actual beam spot size.

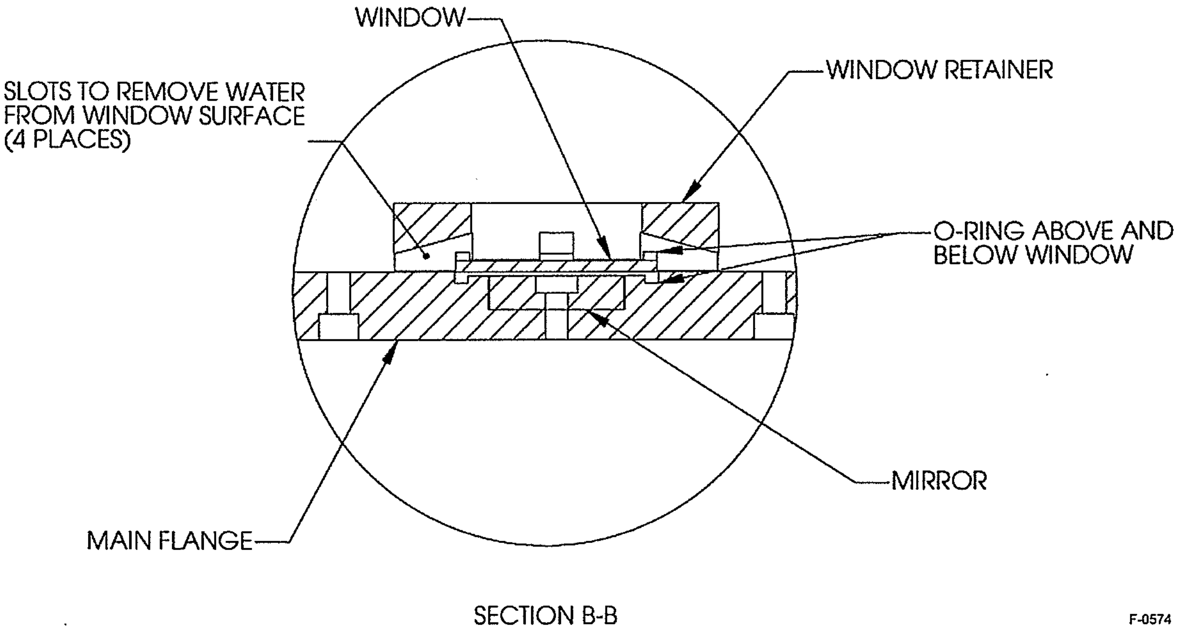

Figure 25. Detail of cell showing position of protective window with respect to mirror.

5.3 System Control Software

The system control program was written using National Instruments' LabWindows CVI programming language. It operates under Windows 98/2000. The program provides full control of system parameters and functions to the user. The user can control the power, temperature, and modulation of each diode laser, monitor health parameters, and monitor intermediate and final calculated results. The software features several graphical user interface panels to organize control features and inputs. There are several GUI panels: Main, CO_2 laser setup, H_2O laser setup, oscilloscope and filtering.

The Main panel is illustrated in Figure 26. At the top is a strip chart to display each of the CO_2 and H_2O concentrations. Data from both the laser and NDIR sensors are displayed in different colors. At the right of the charts are readouts for the current concentration and mixing ratio of each gas. There is also a button that will display the Setup panel for each laser. Below the stripcharts are several boxes grouping related data. The ambient temperature and pressure are displayed in the uppermost box. The sonic data are displayed in the next box. Current values of CO_2 and H_2O concentrations, as well as temperature and pressure, from the NDIR sensor are displayed in the bottom left box. The bottom middle box displays several indicators of sensor health. There are two thermistors monitoring temperatures in the upper and lower bays and a third thermistor on the CPU heat sink. There is also a special IC that monitors the current going

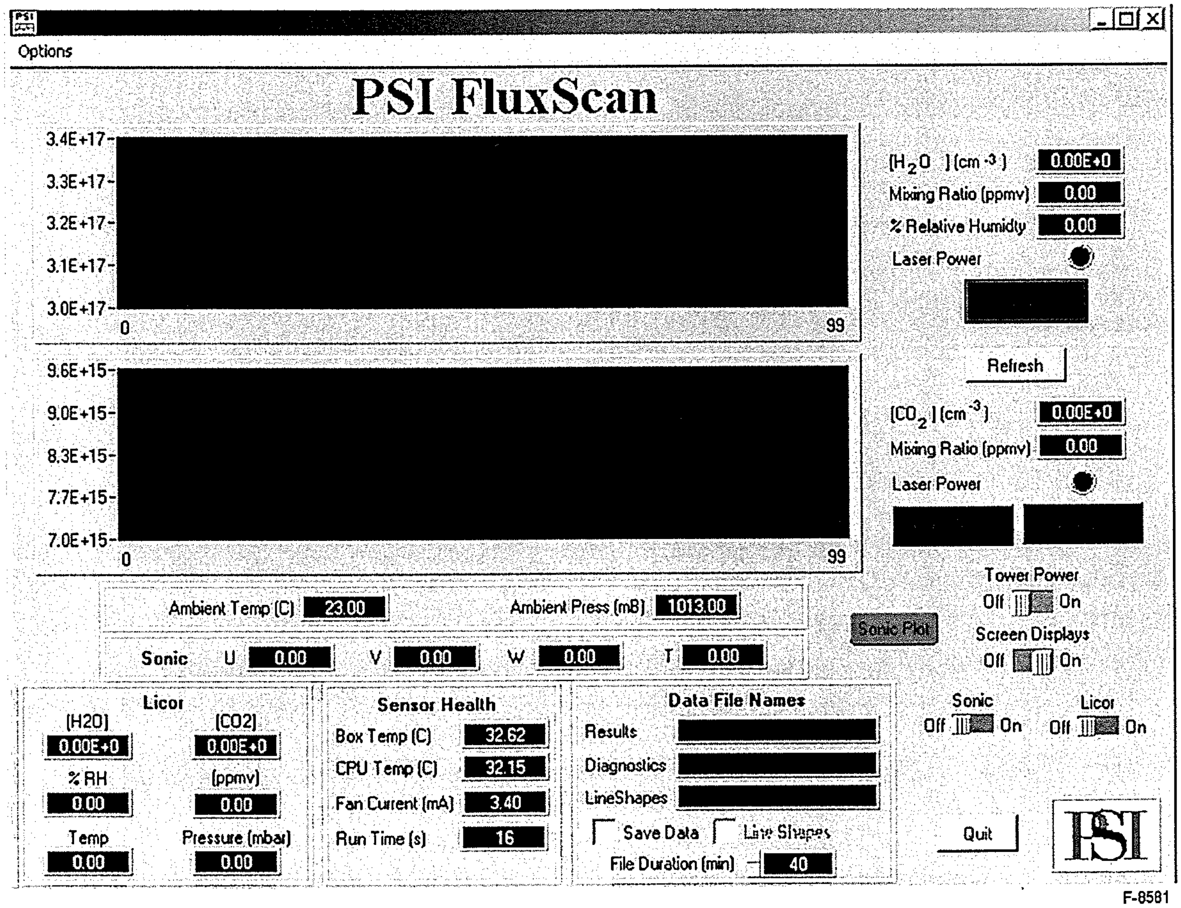

[H_2O] (cm^{-3}) 0.00E+0
Mixing Ratio (ppmv) 0.00
% Relative Humidity 0.00

[CO_2] (cm^{-3}) 0.00E+0
Mixing Ratio (ppmv) 0.00

Ambient Temp (C) 23.00
Ambient Press (mB) 1013.00

Sonic U 0.00 V 0.00 W 0.00 T 0.00

Licor
[H2O] 0.00E+0
[CO2] 0.00E+0
% RH 0.00
(ppmv) 0.00
Temp 0.00
Pressure (mbar) 0.00

Sensor Health
Box Temp (C) 32.62
CPU Temp (C) 32.15
Fan Current (mA) 3.40
Run Time (s) 16

Data File Names
Results
Diagnostics
LineShapes
☐ Save Data ☐ Line Shapes
File Duration (min) 40

F-8581

Figure 26. Control software Main Panel graphical user interface.

to the cooling fans inside the chassis. The bottom right box displays the names of the current files. The operator can save concentration versus time data in a "Results" file, system health parameters in a "Diagnostics" file, and lineshapes in a third file. On the extreme right hand side of the Interface are several switches to control battery power (for the sensors at the top of the tower) and to toggle on/off the sonic anemometer and NDIR sensors.

The Setup panel for the H_2O channel is presented in Figure 27. There are seven main control buttons arranged along the bottom of the panel. The panel is further organized into eight blocks of related parameter inputs and outputs. These are labeled: "Status LEDs", "Control Parameters", "Laser Ramp", "Laser Conditions", "Data File Names", "Experiment Conditions", "Results", and "Digital Filter". Sensor data is graphically displayed in three charts along the right hand side. These are labeled: "H_2O Density", "Acquired Lineshape", and "BRD Linear Signals". The operator uses this panel to set up the experiment by choosing the laser sweep rate and amount of signal averaging desired as well as the laser current modulation. Once spectra are being sampled, the user sets up automatic processing of the raw lineshape. This includes culling off endpoints and calculating a baseline. The baseline is determined by fitting either a line or a third order polynomial to the wings of the spectrum. An absorption spectrum is calculated by subtracting the baseline from the raw spectrum. A similar interface (Figure 28) allows the user to set up the CO_2 channel.

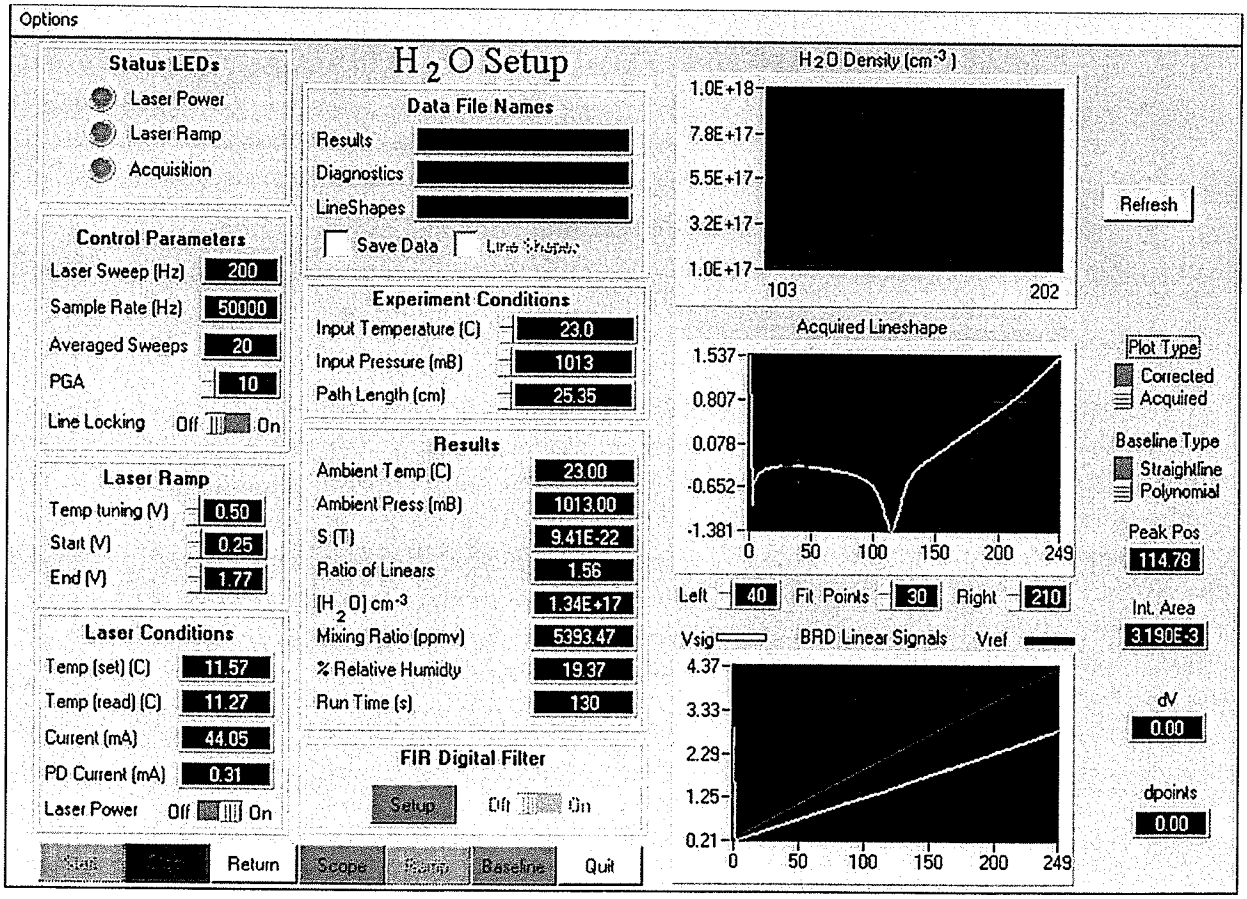

Control Parameters

Laser Sweep (Hz) 200
Sample Rate (Hz) 50000
Averaged Sweeps 20
PGA 10
Line Locking Off On

Laser Ramp

Temp tuning (V) 0.50
Start (V) 0.25
End (V) 1.77

Laser Conditions

Temp (set) (C) 11.57
Temp (read) (C) 11.27
Current (mA) 44.05
PD Current (mA) 0.31
Laser Power Off On

Experiment Conditions

Input Temperature (C) 23.0
Input Pressure (mB) 1013
Path Length (cm) 25.35

Results

Ambient Temp (C) 23.00
Ambient Press (mB) 1013.00
S (T) 9.41E-22
Ratio of Linears 1.56
$[H_2O]$ cm^{-3} 1.34E+17
Mixing Ratio (ppmv) 5393.47
% Relative Humidity 19.37
Run Time (s) 130

Left 40
Fit Points 30
Right 210
Peak Pos 114.78
Int. Area 3.190E-3
dV 0.00
dpoints 0.00

Figure 27. H_2O channel Setup Panel graphical user interface.

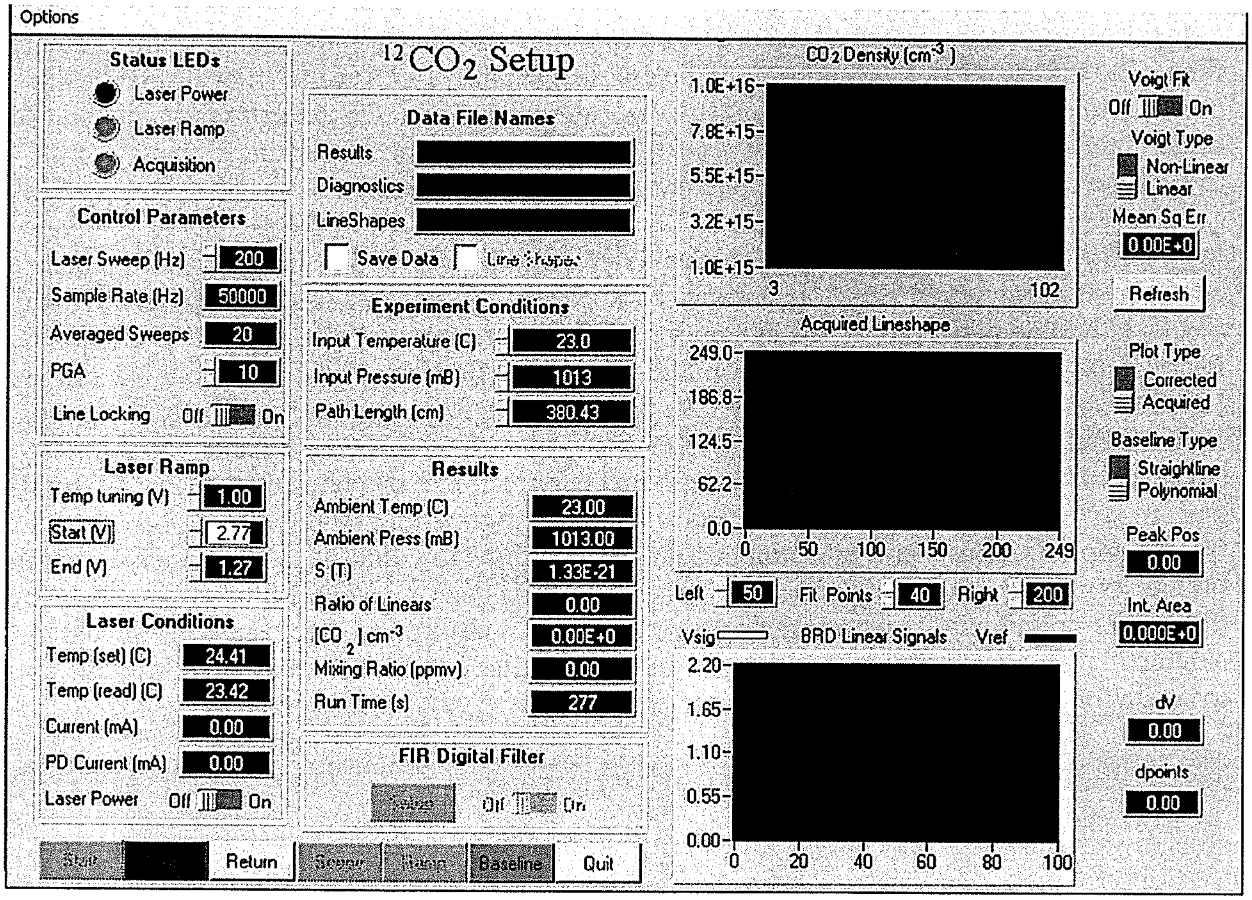

Control Parameters
Laser Sweep (Hz) 200
Sample Rate (Hz) 50000
Averaged Sweeps 20
PGA 10
Line Locking Off ☐ On

Laser Ramp
Temp tuning (V) 1.00
Start (V) 2.77
End (V) 1.27

Laser Conditions
Temp (set) (C) 24.41
Temp (read) (C) 23.42
Current (mA) 0.00
PD Current (mA) 0.00
Laser Power Off ☐ On

Experiment Conditions
Input Temperature (C) 23.0
Input Pressure (mB) 1013
Path Length (cm) 380.43

Results
Ambient Temp (C) 23.00
Ambient Press (mB) 1013.00
S (T) 1.33E-21
Ratio of Linears 0.00
$[CO_2]$ cm^{-3} 0.00E+0
Mixing Ratio (ppmv) 0.00
Run Time (s) 277

Left 50 Fit Points 40 Right 200

Voigt Fit Off ☐ On
Voigt Type ■ Non-Linear ☐ Linear
Mean Sq Err 0.00E+0
Plot Type ■ Corrected ☐ Acquired
Baseline Type ■ Straightline ☐ Polynomial
Peak Pos 0.00
Int. Area 0.000E+0
dV 0.00
dpoints 0.00

F-8583

Figure 28. CO_2 channel Setup Panel graphical user interface.

5.4 Post-Processing Software

Post processing software was developed to process the data and calculate fluxes for four quantities: $^{12}CO_2$ from the laser sensor, H_2O from the laser sensor, CO_2 from the NDIR sensor and H_2O from the NDIR sensor. Typically, 40-min data files were collected and 30-min averages were calculated from the high resolution data. Coordinate rotations and Webb corrections were implemented as described below. Data from the slow response sensors (that we describe in Section 4.1) were used to perform quality assurance checks in order to verify the assumptions underlying the eddy covariance technique. A screen image of the main GUI interface page of the post processing software is presented in Figure 29.

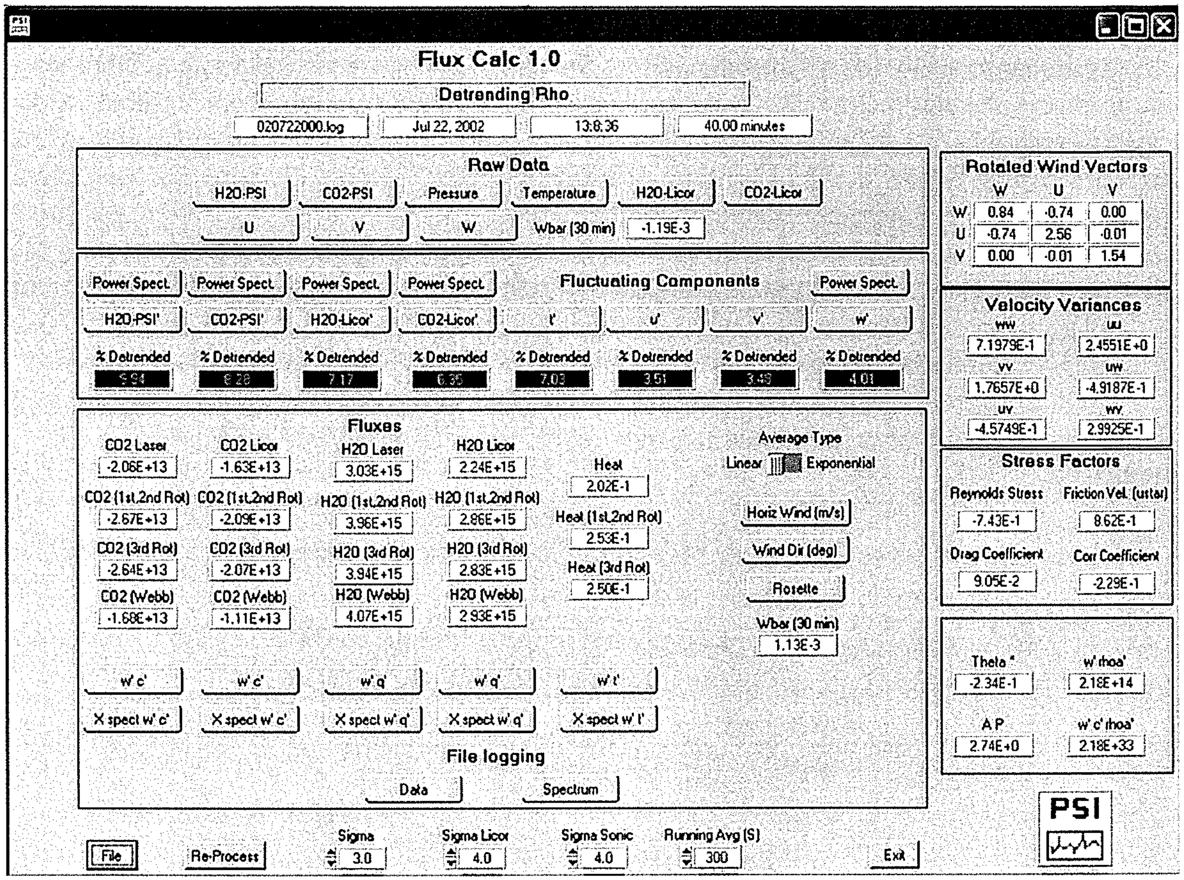

Detrending Rho

020722000.log | Jul 22, 2002 | 13:8:36 | 40.00 minutes

Wbar (30 min) -1.19E-3

H2O-PSI'	CO2-PSI'	H2O-Licor'	CO2-Licor'	t'	u'	v'	w'
% Detrended 5.94	% Detrended 6.28	% Detrended 7.17	% Detrended 6.35	% Detrended 7.03	% Detrended 3.51	% Detrended 3.49	% Detrended 4.01

CO2 Laser	CO2 Licor	H2O Laser	H2O Licor	Heat
-2.06E+13	-1.63E+13	3.03E+15	2.24E+15	2.02E-1
CO2 (1st,2nd Rot)	CO2 (1st,2nd Rot)	H2O (1st,2nd Rot)	H2O (1st,2nd Rot)	Heat (1st,2nd Rot)
-2.67E+13	-2.09E+13	3.96E+15	2.86E+15	2.53E-1
CO2 (3rd Rot)	CO2 (3rd Rot)	H2O (3rd Rot)	H2O (3rd Rot)	Heat (3rd Rot)
-2.64E+13	-2.07E+13	3.94E+15	2.83E+15	2.50E-1
CO2 (Webb)	CO2 (Webb)	H2O (Webb)	H2O (Webb)	
-1.68E+13	-1.11E+13	4.07E+15	2.93E+15	

Average Type: Linear ▨ Exponential

Wbar (30 min) 1.13E-3

Sigma 3.0 | Sigma Licor 4.0 | Sigma Sonic 4.0 | Running Avg (S) 300

	W	U	V
W	0.84	-0.74	0.00
U	-0.74	2.56	-0.01
V	0.00	-0.01	1.54

ww 7.1979E-1 | uu 2.4551E+0
vv 1.7657E+0 | uw -4.9187E-1
uv -4.5749E-1 | wv 2.9925E-1

Reynolds Stress -7.43E-1 | Friction Vel. (ustar) 8.62E-1
Drag Coefficient 9.05E-2 | Corr Coefficient -2.29E-1

Theta * -2.34E-1 | w' rhoa' 2.18E+14
A P 2.74E+0 | w' c' rhoa' 2.18E+33

Figure 29. Post processing software graphical user interface.

The detailed processing procedure is outlined here:

1. Read in 40 min data set
2. Reject outliers
    a. Reject any data point the lies beyond 3 σ of the local 1 second running mean for all variables
    b. Use linear interpolation to replace outliers
3. Calculate running averages for w, T, and all concentrations
    a. Use 300 second moving averages
4. Calculate perturbations of w, T, and all concentrations
    a. Use 300 second moving averages
5. Calculate raw fluxes of w, T, and all concentrations using covariances
6. Apply coordinate rotations to raw fluxes
7. Apply Webb correction to rotation corrected fluxes
8. Calculate power spectra for w', T', and all concentrations'
9. Calculate cospectra of w' with T' and of w' with all concentrations'

5.4.1 Coordinate Rotations

Systematic errors can be introduced into the calculated fluxes if the sonic anemometer is misaligned or if the site is not flat. This occurs by introducing a small nonzero vertical velocity. We are interested in quantifying the turbulent vertical fluxes across the mean horizontal wind streamlines, which follow the land contour. To handle these concerns, the real 3D coordinate system of the sonic anemometer is rotated mathematically in post processing both to obtain a zero mean vertical velocity and to align the longitudinal velocity (u) along the direction of the mean wind. Turbulent fluxes are then computed in reference to the rotated coordinate system.

The coordinate rotations are carried out in three stages. The first rotation is about the z-axis and aligns u into the x direction on the x-y plane. The second rotation is about the x-axis and aligns w into the z direction, resulting in w and v = 0. The corrected turbulent flux is computed as:

$$\overline{w'c'} = \overline{w'c'}_i \cos(\theta) - \overline{u'c'}_i \sin(\theta)\cos(\Sigma) - \overline{v'c'}_i \sin(\theta)\sin(\Sigma) \tag{5}$$

where $\overline{w'c'}_i, \overline{u'c'}_i, and\ \overline{v'c'}_i$ are fluxes computed in the original coordinate system. The sines and cosines are computed in terms of the originally measured u, v, and w:

$$\cos(\theta) = \left(\overline{u}^2 + \overline{v}^2\right)^{1/2} / \left(\overline{u}^2 + \overline{v}^2 + \overline{w}^2\right)^{1/2} \tag{6}$$

$$\sin(\theta) = \left(\overline{w}\right) / \left(\overline{u}^2 + \overline{v}^2 + \overline{w}^2\right)^{1/2} \tag{7}$$

$$\cos(\Sigma) = \left(\overline{u}\right) / \left(\overline{u}^2 + \overline{v}^2\right)^{1/2} \tag{8}$$

$$\sin(\Sigma) = \left(\overline{v}\right) / \left(\overline{u}^2 + \overline{v}^2\right)^{1/2} \tag{9}$$

In some situations, the quantities $\overline{u'v'}\ and\ \overline{v'w'}$ are nonzero. In this case, a third rotation is performed about the z-y plane, rendering $\overline{v'w'}$ zero.

5.4.2 Webb Corrections

A consequence of the assumption of horizontal homogeneity of the field site is that the mean vertical velocity is zero. This is not always the case for sites with active fluxes of sensible heat (<w'T'>) and water vapor (<w'H_2O'>, latent heat). These exchanges result in fluctuations in the density of dry air, which introduces a small but nonzero, mean vertical velocity. This velocity is too small to measure with the sonic anemometer; however, it can result in a significant error in the *in situ* flux measurement of any trace species unless these species are measured as mixing ratios or the air sample is dried and brought to a common temperature. Webb et al. have developed density corrections to account for these influences. With these corrections, the CO_2 flux, F_C, and water vapor flux, F_V, are written as:

$$F_C = \overline{w'\rho_C'} + \mu\left(\frac{\overline{\rho}_C}{\overline{\rho}_a}\right)\overline{w'\rho_V'} + (1+\mu\sigma)\left(\frac{\overline{\rho}_C}{\overline{T}}\right)\overline{w'T'} \tag{10}$$

$$F_V = (1+\mu\sigma)\left\{\overline{w'\rho_V'} + \left(\frac{\overline{\rho}_C}{\overline{T}}\right)\overline{w'T'}\right\} \tag{11}$$

where:

F_C = flux of CO_2
F_V = flux of H_2O
ρ = total air density
ρ_a = dry air density
ρ_V = H_2O density
ρ_C = CO_2 density
ρ = $\rho_a + \rho_V + \rho_C \sim \rho_a + \rho_V$
m_a = molecular mass of dry air
m_V = molecular mass of H_2O
μ = m_a / m_V
σ = $\overline{\rho}_V / \overline{\rho}_a$

For F_C, the first term is the raw flux, the second term represents the water vapor correction and the second term represents the sensible heat correction.

6. Additional Sensors

In addition to the laser absorption spectrometer, we fielded additional sensors during our demonstrations tests. These included an *in situ* NDIR CO_2/H_2O sensor for intercomparison, a sonic anemometer for wind measurement, and a barometer. We next describe each of these sensors.

6.1 NDIR CO_2/H_2O Sensor

We were able to obtain a NonDispersive InfraRed (NDIR) CO_2/H_2O analyzer on loan to us from LiCor for the duration of the program. NDIR analyzers are the community-accepted technology for ambient atmospheric CO_2 measurements in general and LiCor devices are defacto community standards. We had available a LI-7500 Open Path CO_2/H_2O Analyzer (illustrated in Figure 30). The LI-7500 is a dual channel device measuring both CO_2 and H_2O in a common sample volume. The sensor offers an in situ sampling head and a remotely locatable control box. The LI-7500 only became available in general just before the start of the Phase II program. It was the first commercially available open path sensor for CO_2. Relevant performance specs are listed in Table 4.

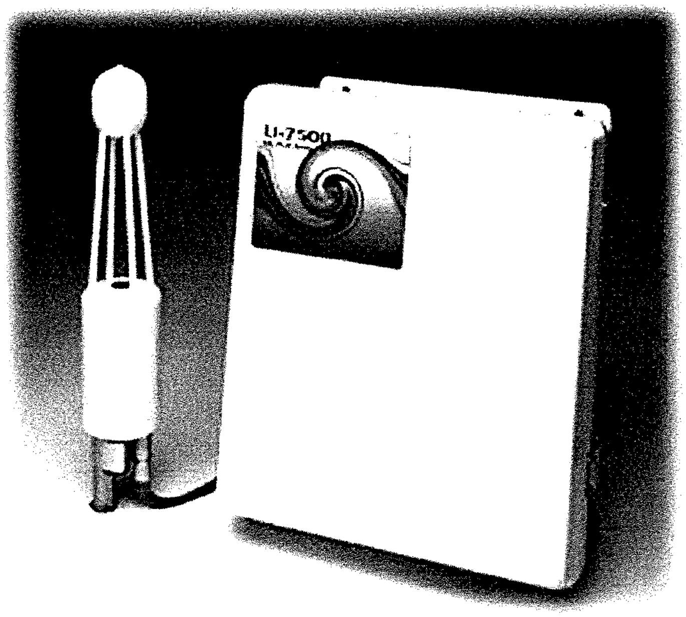

Figure 30. LiCor LI-7500 Open Path CO_2/H_2O Analyzer

Table 4. Performance Characteristics of the LI-7500 NDIR Analyzer

Parameter	**Value**
Bandwidth	5, 10, 20 Hz user selectable
Path length	12.5 cm
Power requirements	10.5 to 30 VDC; 30 W startup, 10 W steady state
Head	6.5 cm diameter x 30 cm 0.75 kg
Control Box	15 x 30 x 35 cm 4.8 kg
CO_2	**μmol mol^{-1}**
Calibration range	0-3000
RMS noise at ambient (370 ppmv)	0.10 at 10 Hz
Zero drift with temperature (per °C)	± 0.3 max, ± 0.1 typical
Gain drift with temperature (per °C)	± 0.1% max, ± 0.02% typical
Sensitivity to a 20 mmol mol^{-1} change in H_2O	± 0.4 max, ± 0.2 typical
H_2O	**μmol mol^{-1}**
Calibration range	0-60
RMS noise at ambient (10 mmol mol^{-1})	3.5 at 10 Hz
Zero drift with temperature (per °C)	± 0.015 max, ± 0.005 typical
Gain drift with temperature (per °C)	± 0.3% max, ± 0.15% typical
Sensitivity to a 20 mmol mol^{-1} change in H_2O	± 0.02 max, ± 0.01 typical

6.2 Sonic Anemometer

For wind measurements, we used a 3-axis, K type probe, sonic anemometer from Applied Technologies Inc. The probe is illustrated in Figure 31. In a given axis, a pair of sonic transceivers emits a pair of pulses, one in each direction. The transit time for both pulses is measured. From these times and the known separation of the transceivers, the wind speed along the given axis can be determined. The performance characteristics of the sensor are listed in Table 5. Of the several types of probes available, this is the recommended version for boundary layer measurements above forest canopies. The probe has an embedded microprocessor. An RS232 interface allows the user to program aspects of the sensor such as the sampling frequency and to either provide a trigger to or receive a trigger from the device. In our case, the laser spectrometer provided a trigger to the sonic anemometer. On receipt of a trigger, the anemometer makes it speed determination and reports the u, v, w wind speed values, as well as the virtual temperature as determined from the equation for the speed of sound in air:

$$T_v = \frac{C^2 M}{\gamma R} \tag{12}$$

where C is the speed of sound measured by the anemometer, M is the molecular weight of air, γ is the heat capacity ratio, and R is the gas constant. This temperature was used for calculating the linestrengths needed by the laser spectrometer for converting measured absorption to concentration.

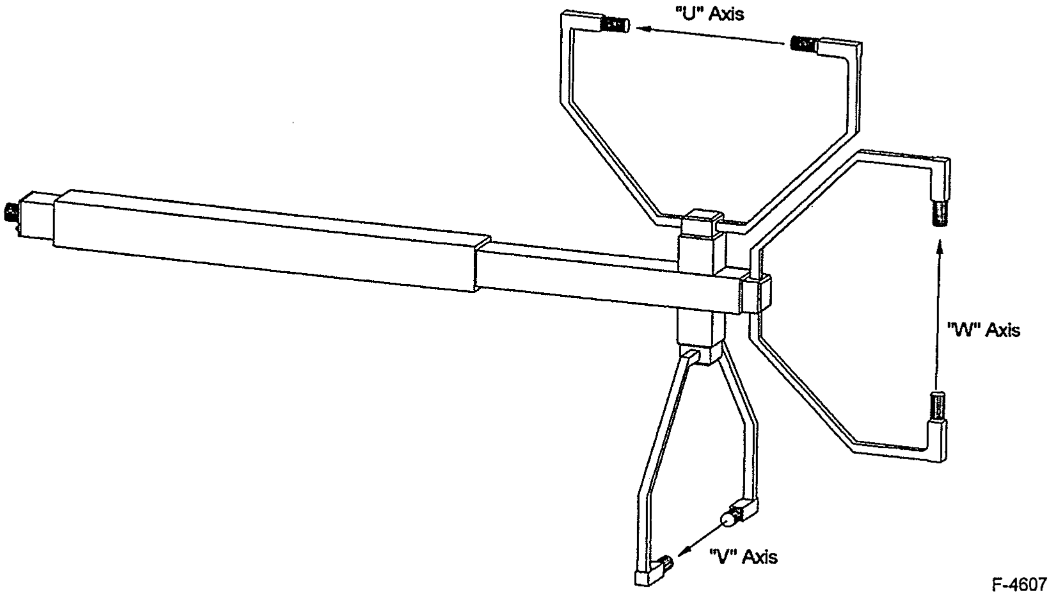

Figure 31. Applied Technologies Inc. K type probe.

Table 5. Characteristics of K type Sonic Anemometer

Parameter	Value
Range of wind speeds	± 20 m/s
Range of temperature	-20 to +50 °C
Pathlength	15 cm
Accuracy	
Wind speed	± 0.05 m/s
Wind direction	± 1 deg
Temperature (abs)	± 2 °C
Temperature (sonic)	± 0.05 °C
Precision	
Wind speed	0.01 m/s
Wind direction	0.1 deg
Temperature (sonic)	0.01 °C

6.3 Barometer

Pressure measurements were obtained using a commercial grade barometer. We used the Vaisala PTB100A sensor. The sensor is illustrated in Figure 32 and its characteristics are summarized in Table 6. The sensor was mounted inside the battery power switching box. The sensor had a direct tube connection to the exterior of the box. The box was mounted on the penultimate stage of the tower. The measured pressure, along with the virtual temperature from the sonic anemometer, was used to calculate the total air density.

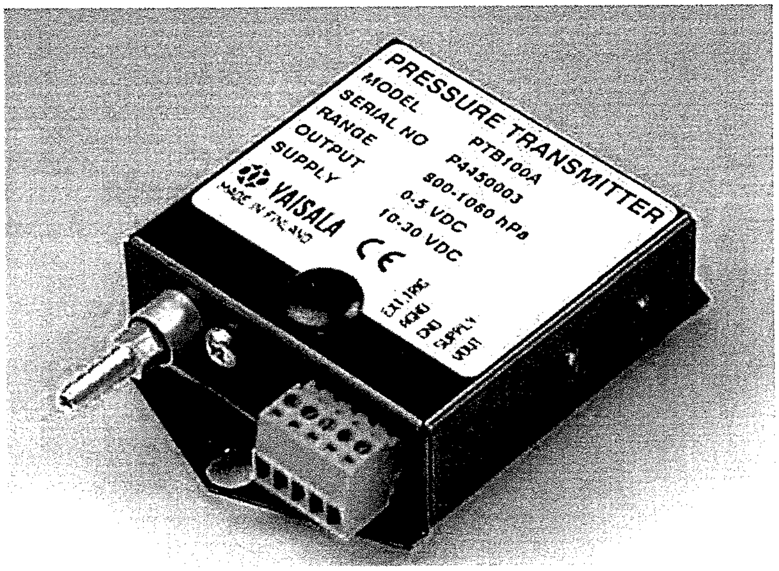

F-8586

Figure 32. Vaisala PTB100A barometer

Table 6. Characteristics of Vaisala PTB100A Barometer

Parameter	**Value**
Measurement range	800...1060 hPa
Range of temperature	-40...+60 °C
Temporal response	300 ms
Accuracy	± 0.3 hPa
Resolution	0.1 hPa
Stability	± 0.1 hPa/yr

7. Lab Calibrations and Stability Measurements

Both the TDL and NDIR instruments were calibrated for CO_2 using precision gas mixtures from Scott-Marrin. The primary mixture was 378 ± 4 ppmv (1%). Figure 33 shows a typical absorption spectrum. Typical computed concentration results are presented in Figure 34 for the calibration and intercomparison of the two instruments. The plot shows 200 seconds worth of span check data for both instruments. This data was taken 4 weeks before the second field trials. The TDL channel measured 376.0 ± 2.5 ppmv for a measurement precision ratio of 0.0066 (1 σ). The NDIR measured 378.7 ± 0.08 ppmv for a measurement precision ratio of 0.00022 (1 σ). The ratio of the TDL to NDIR data over this period was 0.99 ± 0.0066 (1 σ).

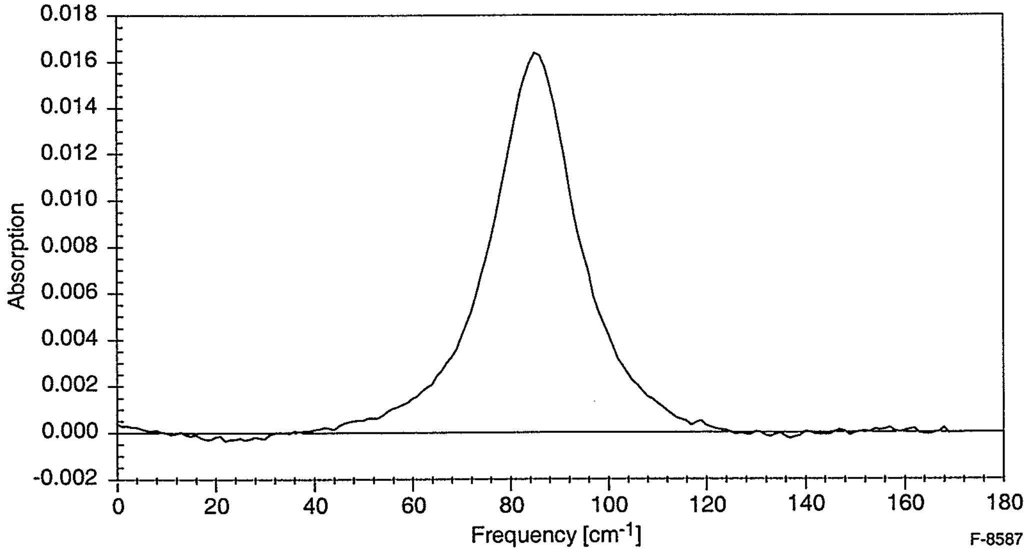

Figure 33. Measured CO_2 spectrum for the R16 line. Conditions: 378 ppmv, 296K, 3.8 m, 0.1 second acquisition.

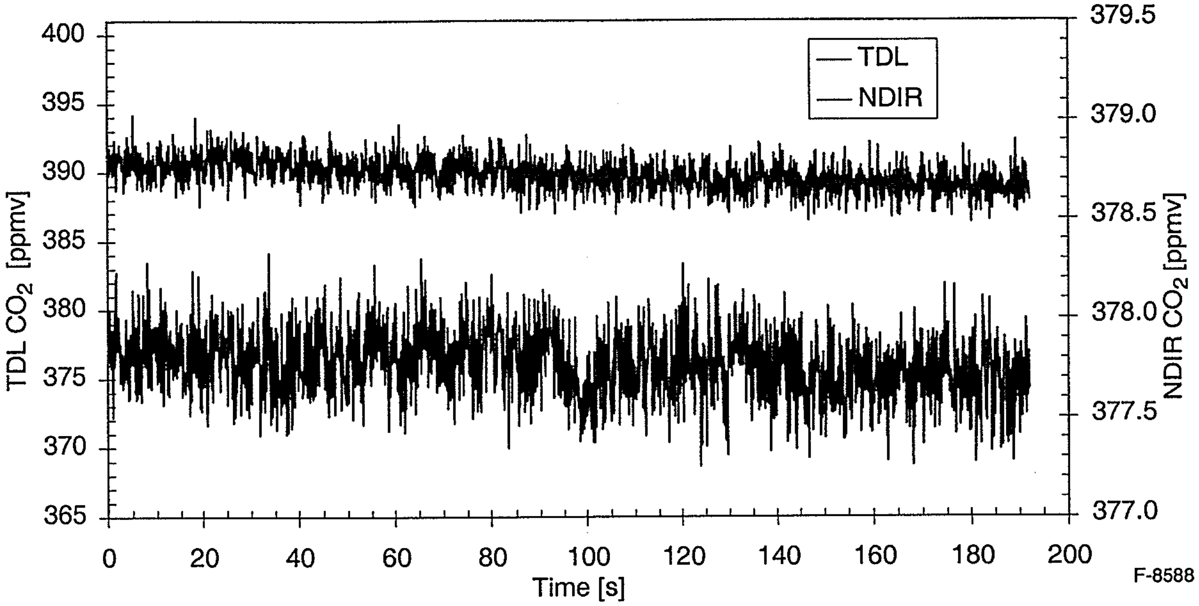

Figure 34. Intercomparison of TDL and NDIR sensors for CO_2 response.

Implementation of a Voigt lineshape fitting routine as described below in Section 8.2 improved the TDL channel precision as documented in Figure 35. This plot shows 600 seconds worth of span check data. This data was taken 3 weeks before the second field trials. Over the period of 100 to 700 seconds, the TDL channel measured 376.6 ± 1.5 ppmv for a measurement precision ratio of 0.0040 (1 σ). This represents a concentration-pathlength product of 5.7 ppmv-m. (The pathlength was 3.8 m). During the Phase I program, we recorded a measurement precision with a similar sensor of 0.8 ppmv for a 333 ppmv calibration mixture, which represents a ratio of 0.0024 (1 σ, over 10 min). That data is reproduced in Figure 36. This represents a concentration-pathlength product of 3.6 ppmv-m. (The pathlength was 4.5 m). We collected precision and calibration data for the TDL CO_2 channel for many weeks before the second deployment and were unable to regain this level of performance. We did observe the measurement precision degrade over this time period but were unable to correct it.

Both the TDL and NDIR instruments were calibrated for H_2O vapor using an in-house saturator facility. The saturator is illustrated schematically in Figure 37. This facility consists of two metered flow lines. The first line is used to meter N_2 into the actual saturator. The reservoir bulb is filled with distilled water. Incoming N_2 flows into the bulb and passes through a frit. Outgoing N_2 is saturated with H_2O vapor at the temperature of the reservoir. The temperature of the reservoir is monitored with a NIST traceable thermometer having 0.1 °C precision. The bulb is placed in a larger reservoir of water that is held within an insulated container. A second metered flow line brings either research grade N_2 or liquid N_2 blowoff to a union with the first line so that the gas streams are mixed. This allows the relative humidity of the mixed flow to be set at any desired level. In addition, the zero of the instruments can also be checked by valving off the moist flow.

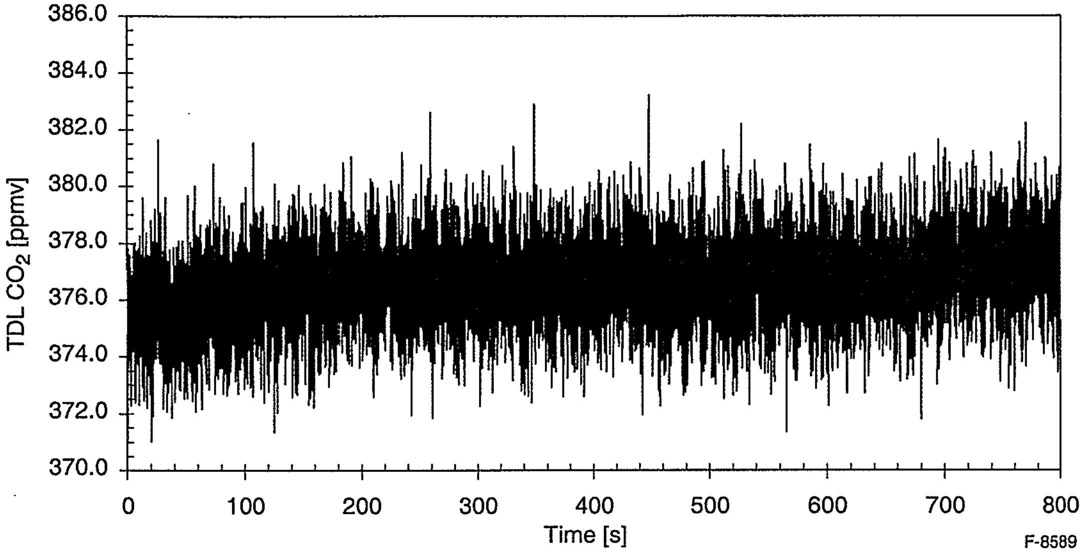

Figure 35. Tdl sensor span check for CO_2 response, with Voigt lineshape fitting active.

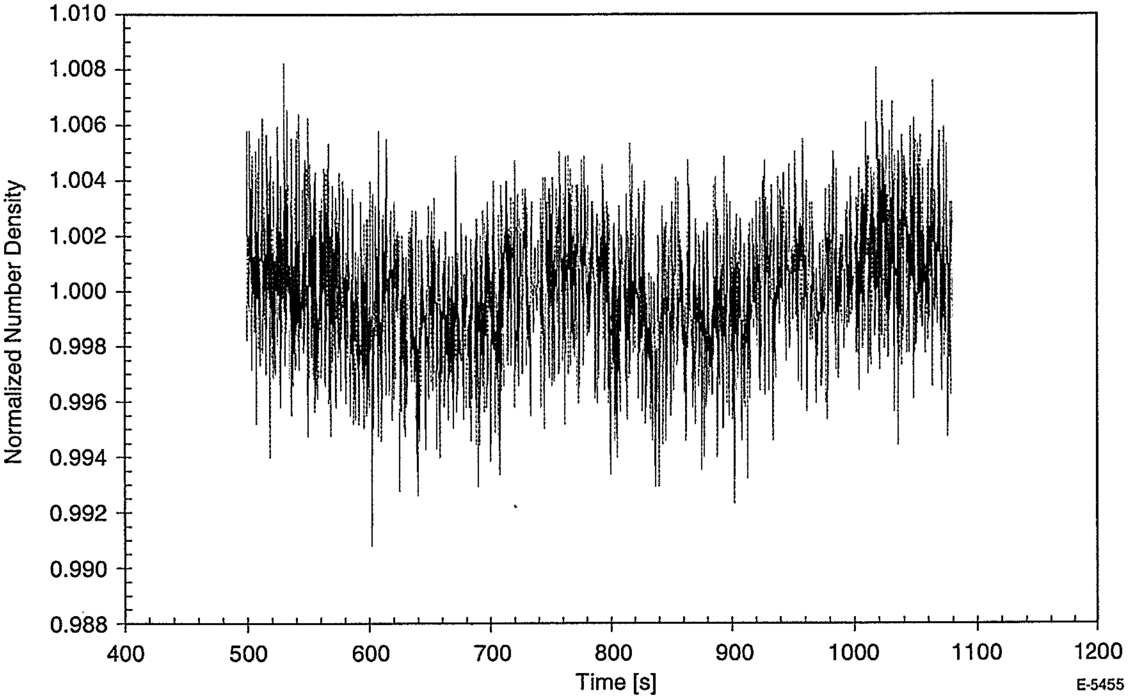

Figure 36. Normalized CO_2 number density measured at 10 Hz vs time for 333 ppmv CO_2/N_2, 4.5 m path, 296 K, 1 atm, and 0.1 s integration. The standard deviation is 2.4×10^{-3} ($1\ \sigma$) for 10 min of data collection.

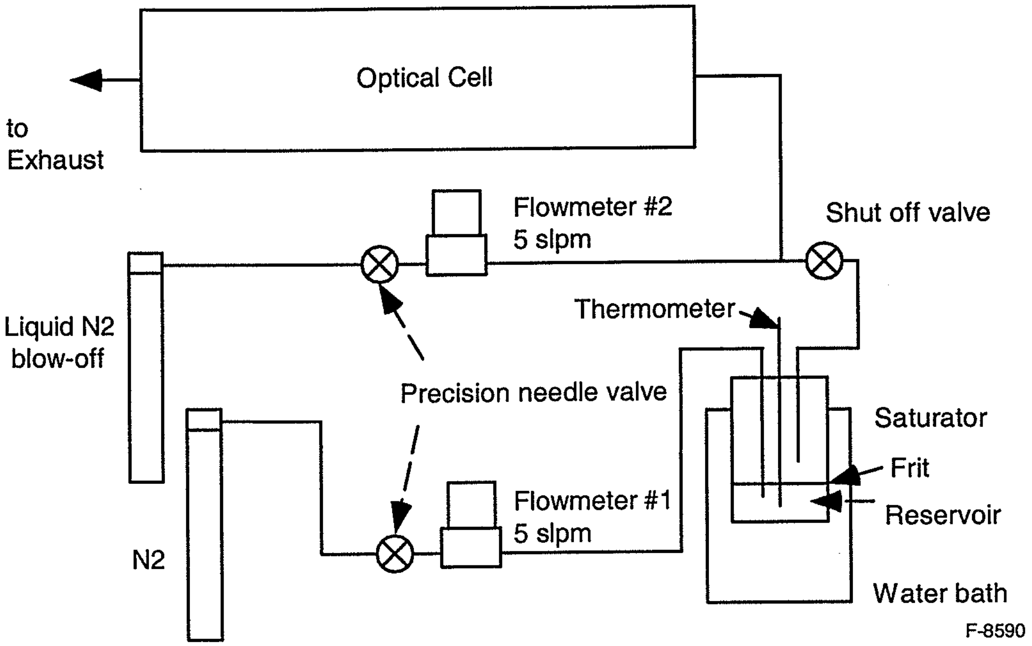

Figure 37. Schematic diagram of in-house H_2O vapor saturator facility.

Typical results are presented in Figure 38 for the calibration and intercomparison of the two instruments. The plot shows 20 min worth of span check data for both instruments followed by a zero check. This data was taken 4 weeks before the second field trials. The sample volumes for the two sensors are different: 50 cm^3 for the NDIR sensor and 126 cm^3 for the TDL sensor. (Note that for the TDL sensor, the calibration can (see Figure 22) has a volume of 3.2 liters, leading to long residence times at typical flow rates during calibration.) Between 600 and 1235 seconds, the TDL-measured relative humidity was 52.0% ± 0.11% for a measurement precision ratio of 0.0022 (1 σ). The NDIR-measured relative humidity was 50.7% ± 0.08% for a measurement precision ratio of 0.0017 (1 σ). The ratio of the TDL to NDIR data over this period was 1.026 ± 0.003 (1 σ). Flows rates were nominally 1 slpm and the temperature of the reservoir changed by only 0.1 °C over the course of the data acquisition.

The stability and reproducibility achieved in these tests were sufficient to prove the value of this technique in this Phase 2 engineering demonstration program. Further calibration and testing will be required for product development. Based on these findings, we moved on to field demonstrations.

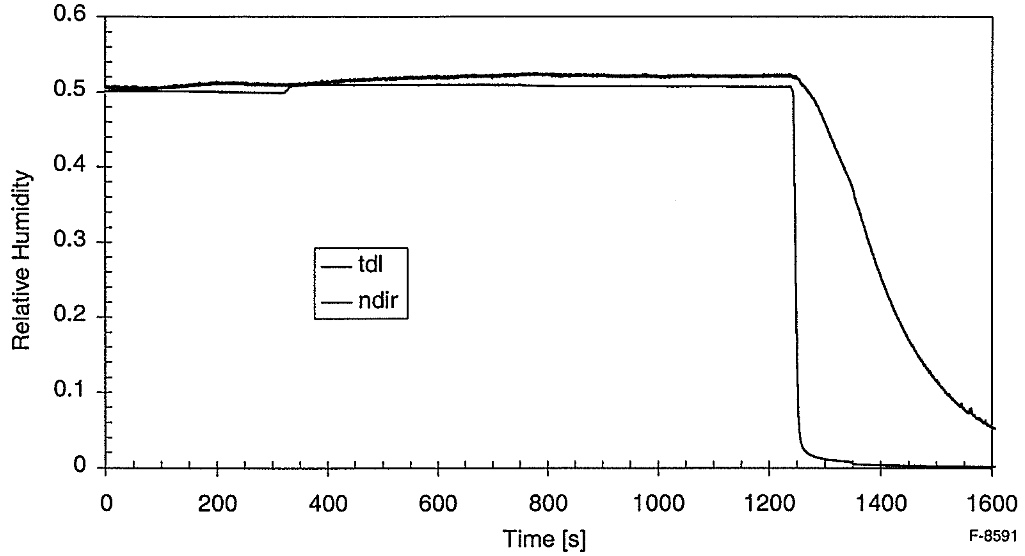

Figure 38. Intercomparison of TDL and NDIR sensors for H_2O vapor response.

8. Field Demonstrations

8.1 First Deployment, Summer 2001, Proctor Maple Research Center, Underhill Center, VT

The goal of the first field trial was to intercompare the laser and LiCor NDIR sensors under real world conditions at a site at which we were the primary users. Thus, it was intended to be a shakedown experience for the laser sensor, in addition to an intercomparison with the NDIR sensor. In addition, we used the opportunity to observe forest respiration above the canopy.

The sensor underwent its first field trials during the Summer of 2001 at the University of Vermont Proctor Maple Research Center (PMRC) in Underhill Center, VT. PMRCs research mission is to investigate the ecology, physiology, and genetics of sugar maple trees, as well as the biochemistry and microbiology of maple sap and syrup. In addition, long term meteorological and air pollution monitoring is performed by the Vermont Monitoring Cooperative (VMC), the State of Vermont, and the U.S. Forest Service and other agencies. The VMC maintains long term monitoring and research programs at PMRC including an instrumented air quality monitoring site that measures acid deposition, UV-B radiation, wet and dry deposition of mercury, and other climatological data. Prof. Gerry Livingston (UVM), a subcontractor to this program, was the research director of the VMC activities at PMRC during the course of this program.

PMRC consists of 200 acres on the western slope of Mt. Mansfield. The site is forested primarily with hardwoods. The primary facility on the site is a modern research laboratory, which served as the base of operations for this program. A photo of the lab is provided in Figure 39. Our field trials were conducted at the Forest Canopy Tower facility located some 300 ft to the NE of the lab. The facility consists of a small, 5 x 10 ft instrument trailer

F-4616

Figure 39. Lab facility at PMRC.

(Figure 40) and a meteorological tower (Figure 41). The trailer is spaced by 20 ft from the tower. The tower is located at 72.9 deg west longitude, 44.5 deg north latitude. The base elevation of the tower is 418 m. The tower is nominally 21 m in height (elevation of final stage flooring). The tower is equipped with permanent meteorological instrumentation located in four monitoring stations at elevations of 0.5, 7.5, 18.7, 24.7 m. These substations include sensors to monitor wind speed and direction, air temperature, and relative humidity. These sensors are recorded at 10 to 60 seconds, depending on sensor and recorded every 15 min by a separate data logger. We refer to these as the "slow sensors". Other measurements at the top of the tower include a dry acid deposition station, a photosynthetically active radiation (PAR) sensor, a total radiation sensor, and an O_3 sampling station. Near the tower are five soil temperature measurement arrays with each array having sensors at five different depths.

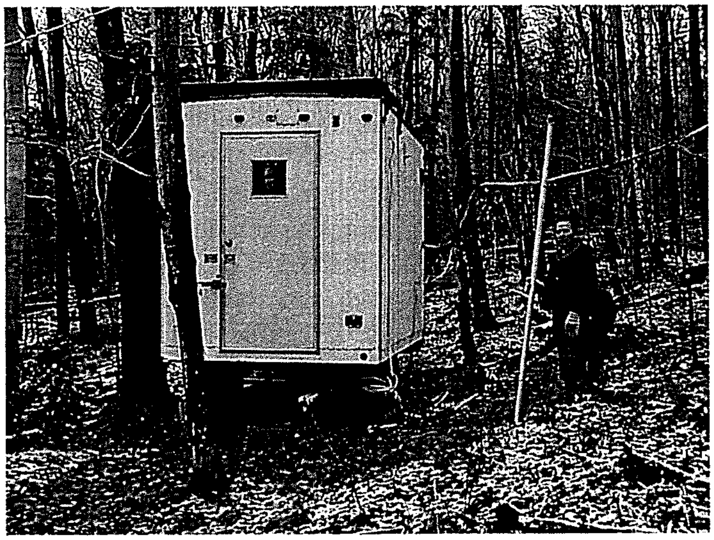

F-0578

Figure 40. Instrument trailer at PMRC.

F-0579

Figure 41. Canopy tower at PMRC.

The site trailer provides a controlled environment for the instrumentation. The trailer is air-conditioned and has line power (200 A service). Our instrumentation utilized a separate circuit. There is also a fiber-optical Ethernet connection between the trailer and the lab. Before our work commenced, the guy wires to the tower were retensioned and a cell phone tower installation contractor was consulted to review lightning protection.

In preparation for the installation of our sensor suite, we reviewed historical wind data for the site covering the past several years. In late July and August, the principal wind direction is SE and is relatively invariant with time of day. Thus we chose to mount our sensors off the SE corner of the tower. Our sensor array consisted of two open path multipass cells for the laser-based sensor, the sonic anemometer, and the sensor head for the Li-Cor NDIR instrument. We designed and fabricated a retractable boom that allowed the sensors to be mounted and serviced easily. The design is illustrated in Figure 42. In the retracted position, the sensors can be easily serviced from the top platform. In the extended position, the boom places the sensors one "tower characteristic width" (6 ft) away from the tower into the prevailing wind. The sensors were spaced by one "sensor characteristic width" (~1 ft) on a cross bar at the end of the boom. When

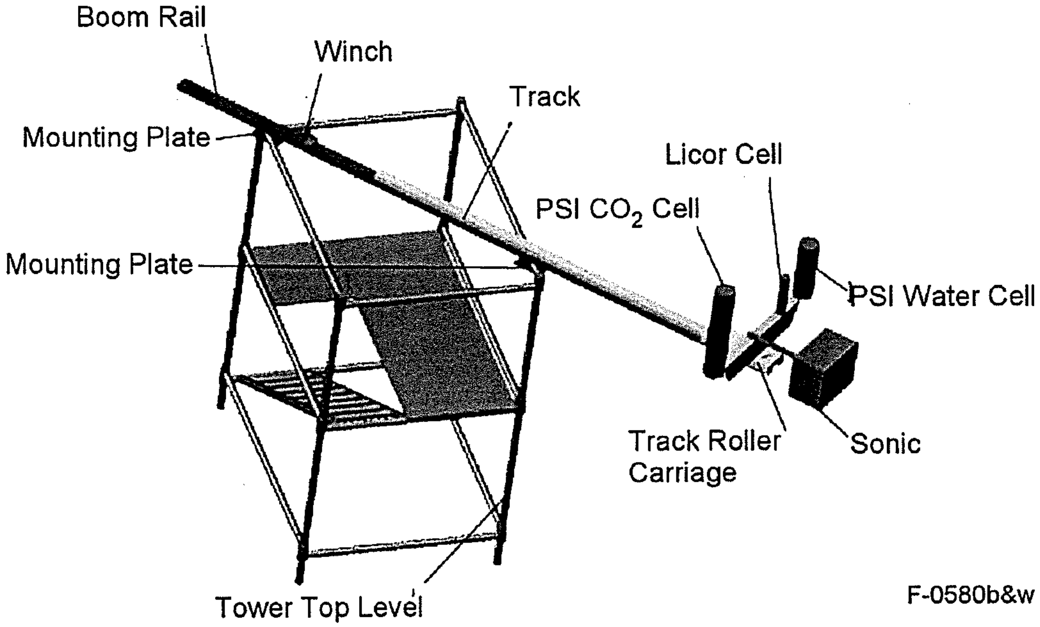

Figure 42. Sensor suite deployment on retractable boom at tower site at PMRC.

not in use, the boom was retracted and covers placed over the optical cells. The boom was mounted on the top rail of the final stage at an elevation of 21.9 m. The azimuth angle of the boom was 158 deg true.

The sonic anemometer and Li-COR NDIR sensor heads, as well as our Vaisala barometer, required DC power at the top of the tower. To provide this power, we used a deep cycle, marine storage battery of ~ 100 A-h capacity. This provided more than 2 weeks of operational power before recharging was required. We designed and fabricated an all weather power distribution box that routed power to each of the sensor heads. Power to individual sensors was fused and the main power was routed through a remotely controlled relay. The box was located just before the last level of the tower.

The SPM was housed in the site trailer. All electric and fiber optic cables running between the SPM and the sensors on the tower were bundled together and placed inside a protective plastic sheath. The SPM collected data from the sonic anemometer and the NDIR sensors over high-speed serial lines. It combined these data with data developed from the laser-based sensor to create a complete signal record file. Health monitoring was also performed by the SPM on various parameters of the lasers, for example. This data was written to a second file. The operator interfaced with the SPM single board computer using a standard monitor, keyboard and mouse. This allowed the operator to set up the sensor and monitor data and health parameters at the tower. In addition, it was also possible to utilize a fiber optic-based Ethernet LAN between the trailer and the lab as shown in Figure 43. The SPM and other sensors in the trailer shared the line via a local hub. At the lab, another hub could route data to our remote laptop. Thus, the SPM could be run from the lab over the Ethernet link, although in practice, we ran exclusively from the trailer.

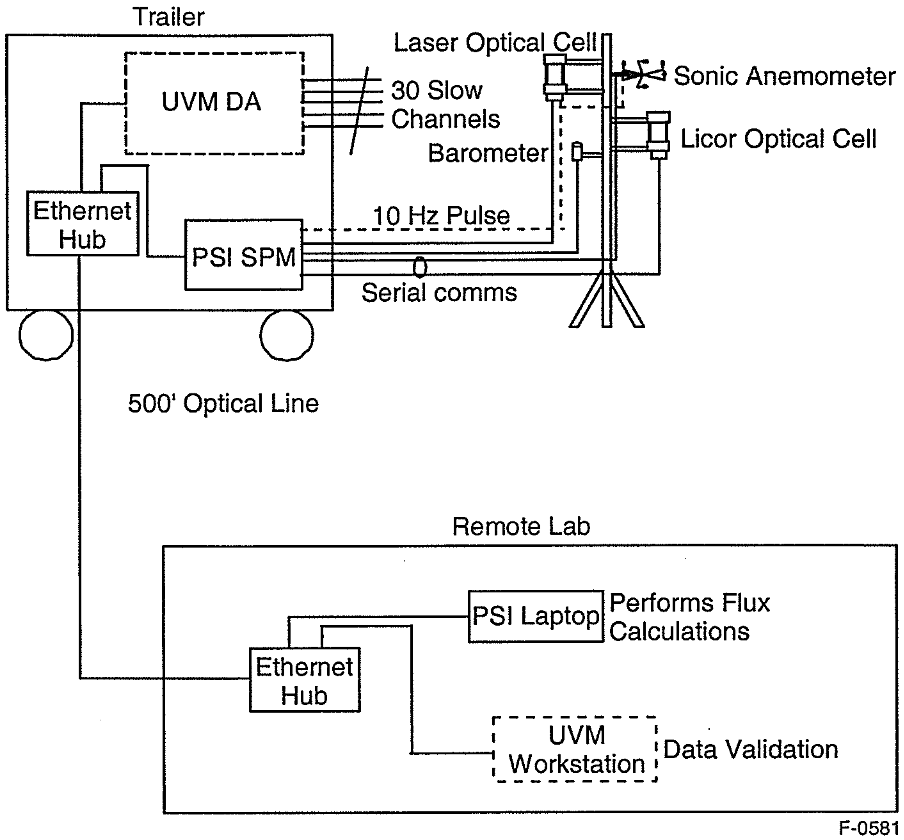

Figure 43. PMRC site communications.

Deployment Configuration

The sensor was configured as described in Table 7 for these initial demonstrations:

Table 7. Sensor Configuration Versus Deployment

	1st Deployment, 2001		**2nd Deployment, 2002**	
	Path	**Species**	**Path**	**Species**
Small cell	7.33 m 29 passes	$^{12}CO_2$, R32 4999.43 cm^{-1} peak $\alpha = 1.8\%$	3.80 m 15 passes	$^{12}CO_2$, R16 4989.97 cm^{-1} peak $\alpha = 2.0\%$
Large cell	0.56 m 1 pass	H_2O 7185.6 cm^{-1} peak $\alpha = 5.0\%$	34.5 m 69 passes	$^{12}CO_2$, R48 5006.98 cm^{-1} peak $\alpha = 1.1\%$ and $^{13}CO_2$, R22 5007.36 cm^{-1} peak $\alpha = 0.09\%$
Small cell			0.25 m 1 pass	H_2O 7185.6 cm^{-1} peak $\alpha = 2.3\%$

We collected data with the integrated sensor suite for a total of ~20 hours over the course of 2 weeks between 6 August and 17 August. In general, we found that the data from the $^{12}CO_2$ channel of the laser sensor was noisier than expected. The noise was correlated with the magnitude of the horizontal wind. We concluded that index variations arising from the wind was steering the incident beam over a large fraction of the extended response InGaAs signal detector surface area (1 mm diameter). Thus we felt we could not guarantee that the signal detector was collecting the entire signal beam power 100% of the time. This led to an effectively time-varying ratio of the reference and signal detectors that imposed increased noise on the log output of the BRD.

We also found that the data from the H_2O channel of the laser sensor at times suffered from a small offset drift. The drift was apparently correlated with scattered sunlight as the concentration outputs of the laser and NDIR sensors were very similar during periods of overcast and blocked direct sunlight (either by large clouds or via shading of the sensor heads with a large piece of cardboard). The magnitude of the effect also varied with solar angle. We concluded that scattered sunlight was leaking onto the signal detector. This led to a sufficiently large additional dc photocurrent on the signal detector to change the reference/signal ratio. At times this caused a spike at the beginning of the Vlog trace when the reference/signal ratio was very close to 1. The situation is illustrated in Figure 44. We darkened the metal surfaces in the field-of-view of the detector with some success. We noticed less of a scattered light problem with the $^{12}CO_2$ channel multipass cell.

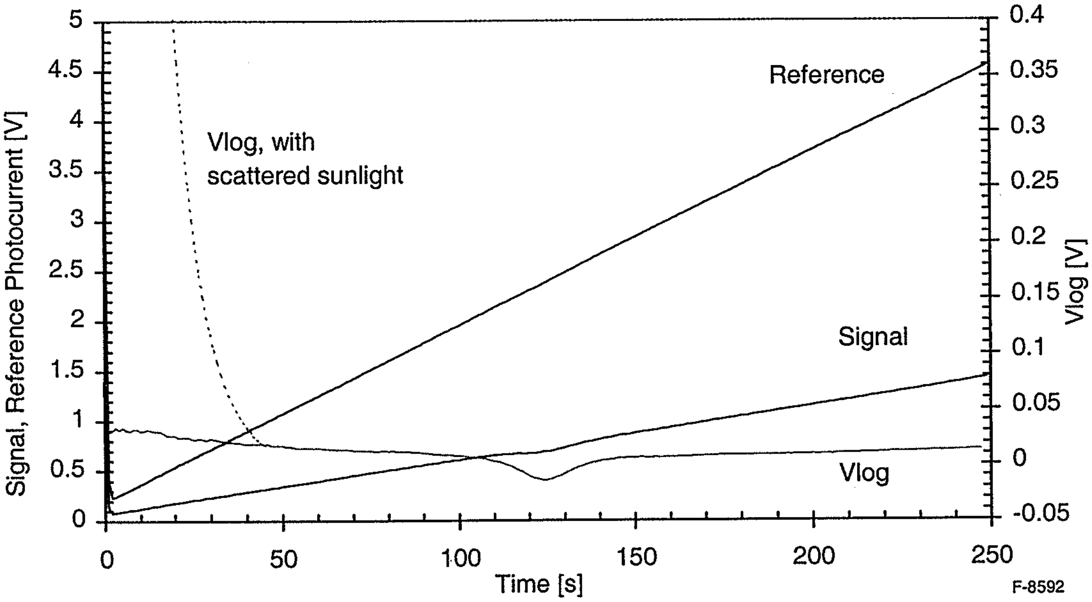

Figure 44. Illustration of effect of additional photocurrent from scattered sunlight on signal detector on the reference/signal current ratio.

The lessons learned from our initial deployment were hard ones in that we felt the data was sufficiently compromised as not to warrant full processing. We chose instead to concentration on engineering solutions to the deployment issues we had discovered.

8.2 Interim Upgrades and System Improvements

One of the first improvements to the system was to install and characterize the new 2 μm lasers that arrived too late to be included in the first summer's field testing. These lasers were semicustom fabricated devices from NEL that would allow access to the stronger CO_2 lines (P10, P12, R16, R18) near the peak of the Boltzmann distribution, as discussed above. We installed one of these devices and characterized it. The current tuning behavior is presented in Figure 45. We then set it up to monitor $^{12}CO_2$ on the R16 line at 4989.97 cm^{-1}.

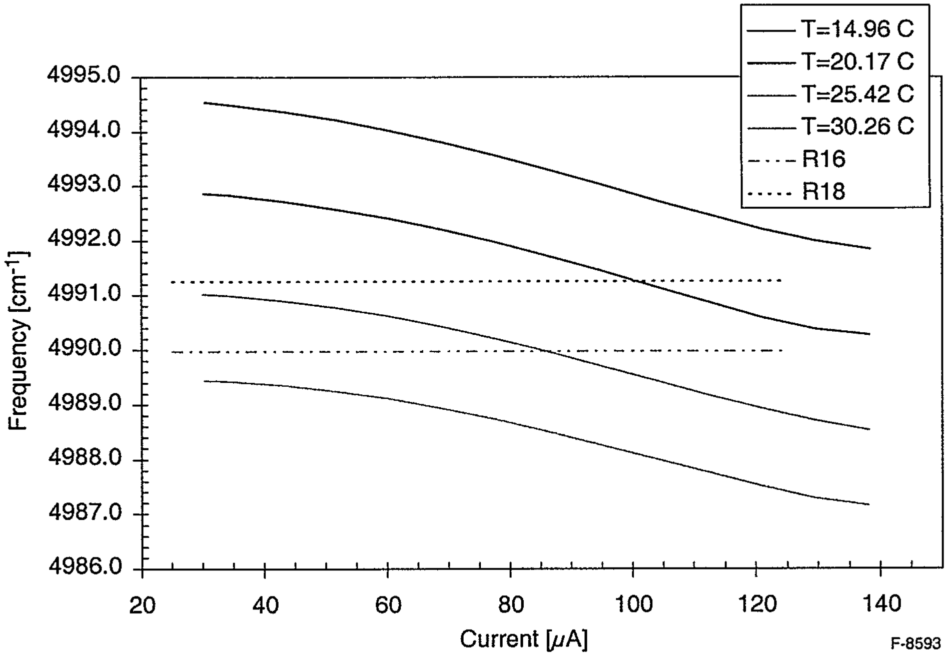

Figure 45. Wavelength vs injection current for the NEL KELD1951SCB SN 104310 device.

We were able to identify a new vendor for larger area extended response InGaAs detectors. Hamamatsu was able to provide us with 3 mm diameter devices. We modified the mounts and incorporated these into the $^{12}CO_2$ channel as the signal and reference detectors.

We investigated two approaches to dealing with the scattered sunlight issue. First, we attempted to insert narrow bandwidth interference filters into the signal leg of the H_2O channel. Although the peak absorption from the water vapor was on the order of 2%, the filter induced interference fringes on the Vlog of sufficient amplitude to cause problems with the measurement. Thus we did not incorporate these into the system.

We did design a baffle for the signal detector for all the absorption cells. This baffle served to confine the field-of-view of the detector. A diagram of the baffle is provided in Figure 46. The baffle was fabricated from black Delrin™ plastic and screwed into place.

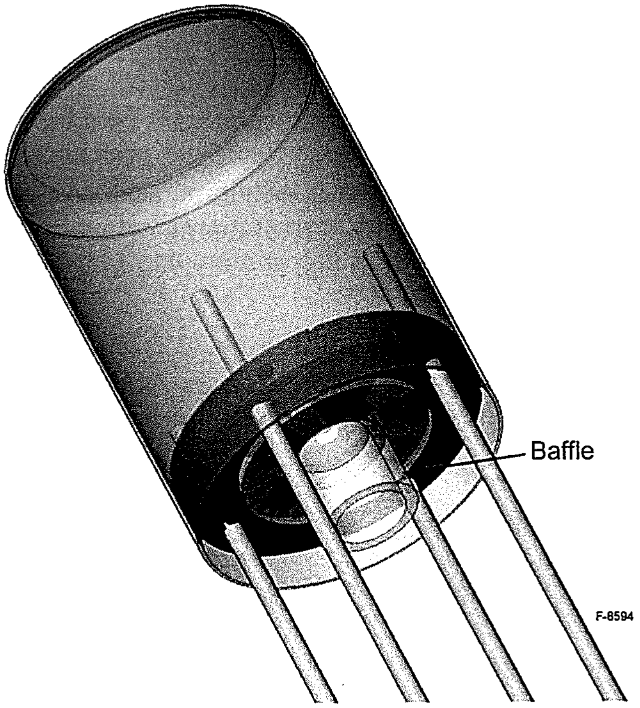

Figure 46. Baffle added to absorption cell to decrease amount of scattered sunlight reaching photodiode detector.

During the first field deployment, we used the large cell (0.5 m base path) for the H_2O channel. We did not have the opportunity to use it to make $^{13}CO_2$ measurements. The large cell used 0.25 in diameter rods for its main supports. We found this design to have problems with mechanical shifts affecting the alignment, even for the single pass application used for the H_2O measurements. Adding tensioned steel wire as braces did not help. We therefore designed and fabricated a new support system for the large cell. The flanges holding the mirrors were attached to a solid aluminum chassis machined from a single piece of thick walled pipe. The design is illustrated in Figure 47. This design showed significant improvement in alignment stability.

We demonstrated the operation of the large cell for $^{13}CO_2$ measurements by collecting spectra of room air. Figure 48 shows such a spectrum. The R48 and R50 peaks of $^{12}CO_2$ are seen along with the R22 peak of $^{13}CO_2$. The measured ratio of $^{13}CO_2$ to $^{12}CO_2$ is 0.01 whereas the ratio of the natural abundances is 0.011.

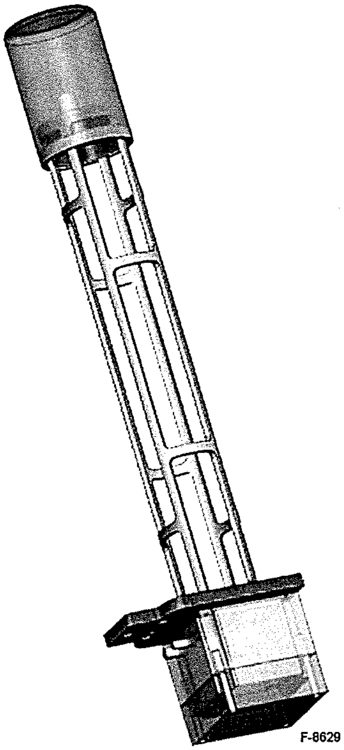

Figure 47. Single piece aluminum chassis for large base path cell.

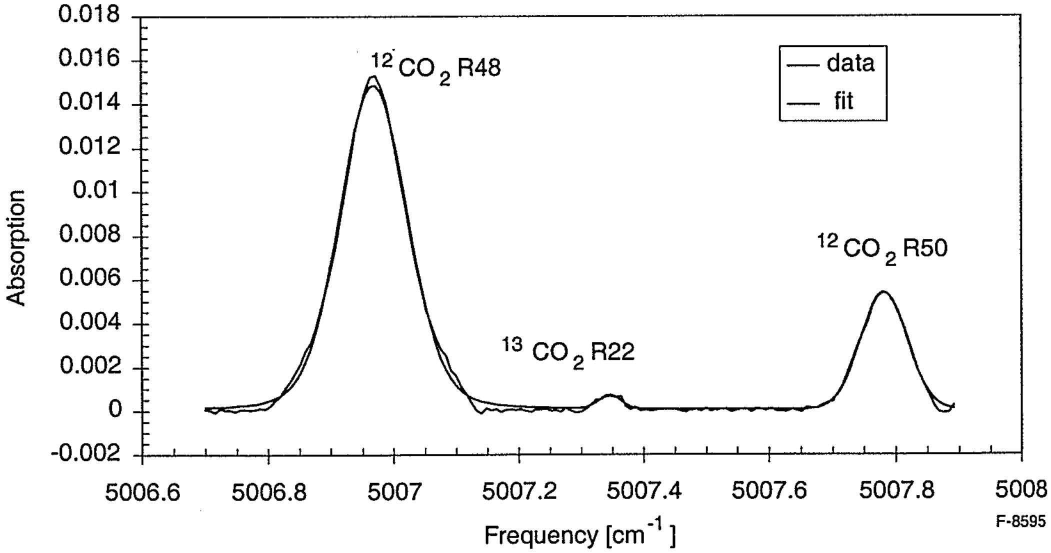

Figure 48. Spectrum of room air showing detection of $^{13}CO_2$.

The final enhancement to the system was the addition of spectral lineshape fitting routines to the operational software of the sensor. This additional code allowed us to fit the measured lineshape for a given species to an approximation of the Voigt lineshape given by:

$$\frac{I}{I_o} = \left[1 - \frac{w_l}{w_v}\right] exp\left[-2.772\left(\frac{\nu - \nu_o}{w_v}\right)^2\right] + \left[\frac{w_l}{w_v}\right]\frac{1}{1+4\left(\frac{\nu-\nu_o}{w_v}\right)^2} \tag{13}$$

where:

$$w_d = 7.16\,x\,10^{-7}\,\nu_o\sqrt{\frac{T}{M}}$$

ν_o is the center frequency

T is temperature

M is molecular mass = 44 for CO_2

$$w_l = 2\,\gamma_o\,P$$

γ_o is the collisional broadening parameter = 0.077 cm^{-1}/atm

P is atmospheric pressure

$$w_v = 0.5346\,w_L + \sqrt{w_d^{\,2} + 0.2166\,w_l^{\,2}}$$

where ω are full width half maximum for Doppler (d), Lorentz pressure (L) and Voigt (v) lineshapes.

The routine fit the measured signal to the sum of the Voigt lineshape approximation and a third order polynomial representing the baseline:

$$Y = a + bx + cx^2 + dx^3 \tag{14}$$

The routine used a nonlinear least squares method to carry out the fit. We implemented the fit with only Io and the baseline function constants as variable parameters. All the other parameters, including ω_d, ω_l, and ω_v, were calculated from measured parameters (T, P) and held fixed during the fitting process. The fitted Voigt function is then integrated in the usual way to calculate number density.

8.3 Second Deployment, Summer 2002, Proctor Maple Research Center, Underhill Center, VT

We were initially scheduled to deploy at the Environmental Measurement Station (EMS) (Ameriflux site) at Harvard Forest, Petersham, MA during our second field demonstration. The main canopy tower is fully instrumented and makes measurements full time. The site maintains a second canopy tower within ~100 m of the main tower for additional measurements, instrumentation tests, and for use by visitors. Unfortunately, this tower was condemned during the winter of 2001-2. Construction delays for the replacement tower, as well as load carrying ability and height above the canopy for the new tower, worked to preclude us from deploying there. Thus we returned to the PMRC site for our second field demonstration.

The sensor configuration for the second year is summarized in Table 5. A schematic of the sensor suite is provided in Figure 49. Table 8 lists the separations of the various sensor heads. A photo of the sensor suite installed on the tower is provided in Figure 50. We utilized a 25 cm base path cell for the $^{12}CO_2$ measurements, a second 25 cm cell for the H_2O measurements, and the refurbished 50 cm cell for the $^{13}CO_2/^{12}CO_2$ measurements. The installation details were the same as the previous year except that the azimuth angle of the boom was 171 deg true. We did, however, place all our upgraded fiber optic and BNC cables within PVC tubing strapped directly to the tower upright frame members.

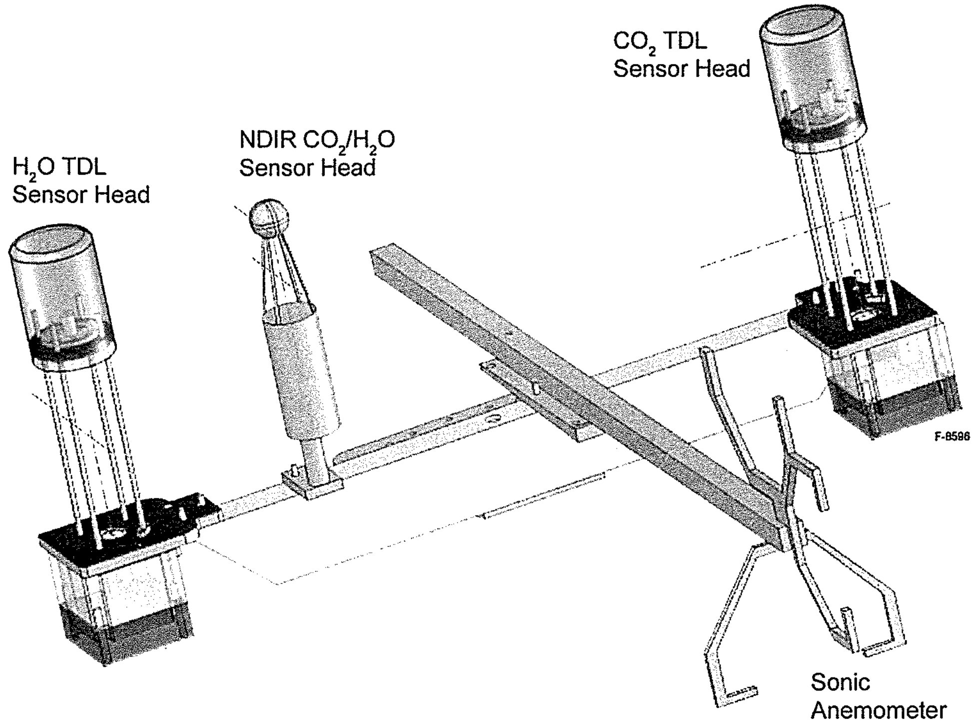

Figure 49. Schematic diagram of the sensor suite.

Table 8. Sensor head separations

Sensor Pair	Separation [cm]
Sonic anemometer to TDL CO_2	72.6
Sonic anemometer to NDIR	77.5
Sonic anemometer to TDL H_2O	93.5
Tdl CO_2 to NDIR	70.6
Tdl H_2O to NDIR	29.6

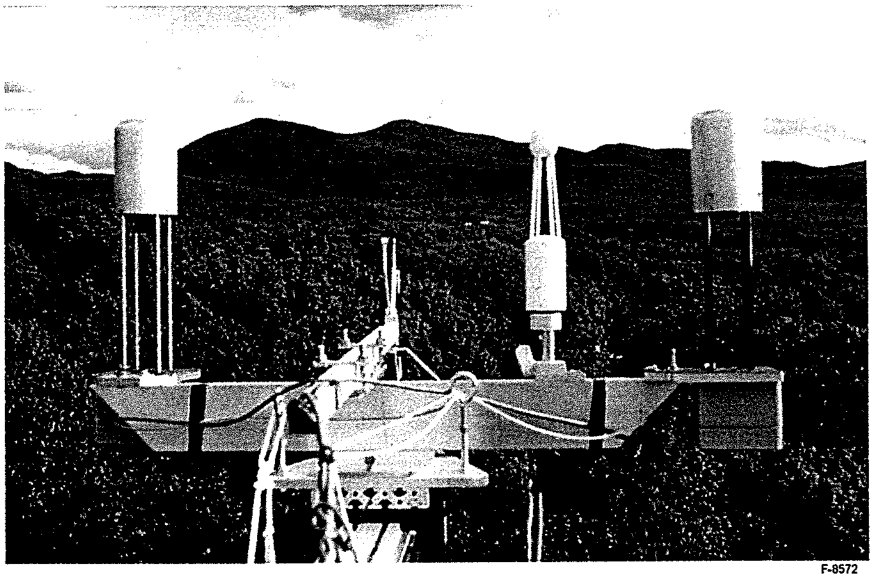

Figure 50. Photo of the sensor suite installed on the tower.

We collected data with the integrated sensor suite for a total of ~20 hours over the course of 2 weeks between 15 July and 26 July. We recorded flux data on Wednesday, 17 July (3 p.m. to sundown), on Friday 19 July (start to noon), on Monday, 22 July (1 p.m. to sundown), and on Thursday 25 July (all day). We present a detailed look at the data from Monday, 22 July. Although surface winds were fairly strong that day, they were consistently out of the south-southwest and the day was primarily characterized by mostly sunny conditions. In general, we found that the enhancements to the laser-based sensor yielded noticeable improvements in the data, especially from the $^{12}CO_2$ channel. For the other data sets, the winds were out of the wrong direction. For the rest of the deployment, it was raining, or we were installing or deinstalling the equipment. We were generally able to install or deinstall in a period of 1.5 days.

We collected 9 files between noon and sundown on this day; each 40 min in length. As illustrative data, we now present system data from the first file for 13:08 EDT. Figure 51 shows the horizontal wind rosette as measured by the sonic anemometer. The position of the boom is also indicated. Figure 52 shows the temporal history of the horizontal wind magnitude, while Figure 53 shows the temporal history of the horizontal wind direction, both measured by the sonic anemometer. The cup anemometer data for the 24.7 m tower station is also reported. A histogram of the horizontal wind magnitude (sonic anemometer) is presented in Figure 54, while a histogram of the horizontal wind direction (sonic anemometer) is presented in Figure 55. Finally, a histogram of the vertical wind magnitude (sonic anemometer) is presented in Figure 56. The horizontal wind stayed remarkably constant for the entire day. The wind rosettes for the other files are very similar to that for the first. This data indicates that the boom should have been located in a more southwesterly direction. We do not believe that the optical cell for the laser $^{12}CO_2$ measurements was seriously shadowed by the other sensors.

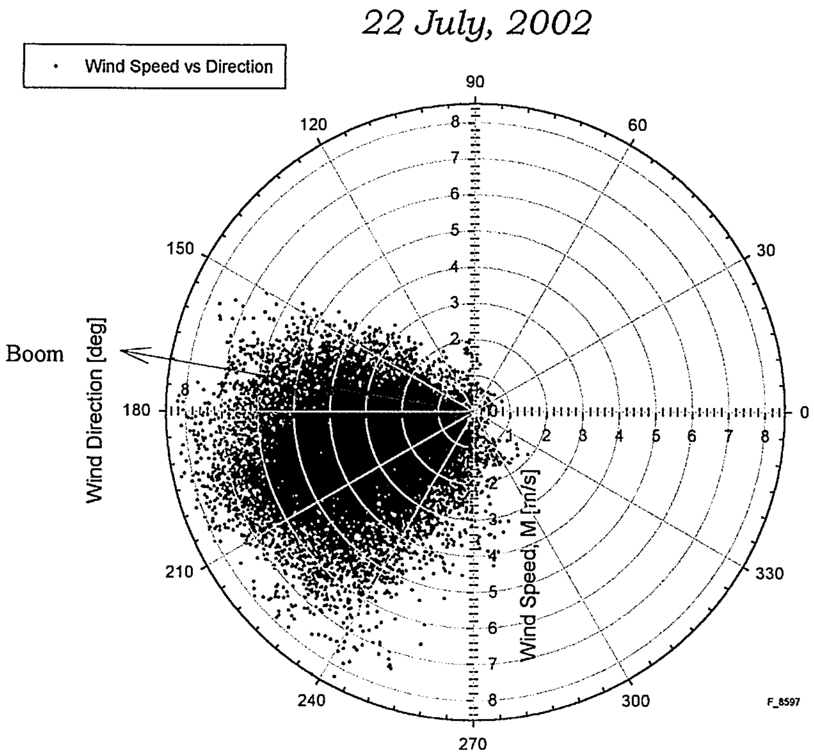

Figure 51. Horizontal wind rosette, 13:08, 22 July 2002 measured by the sonic anemometer.

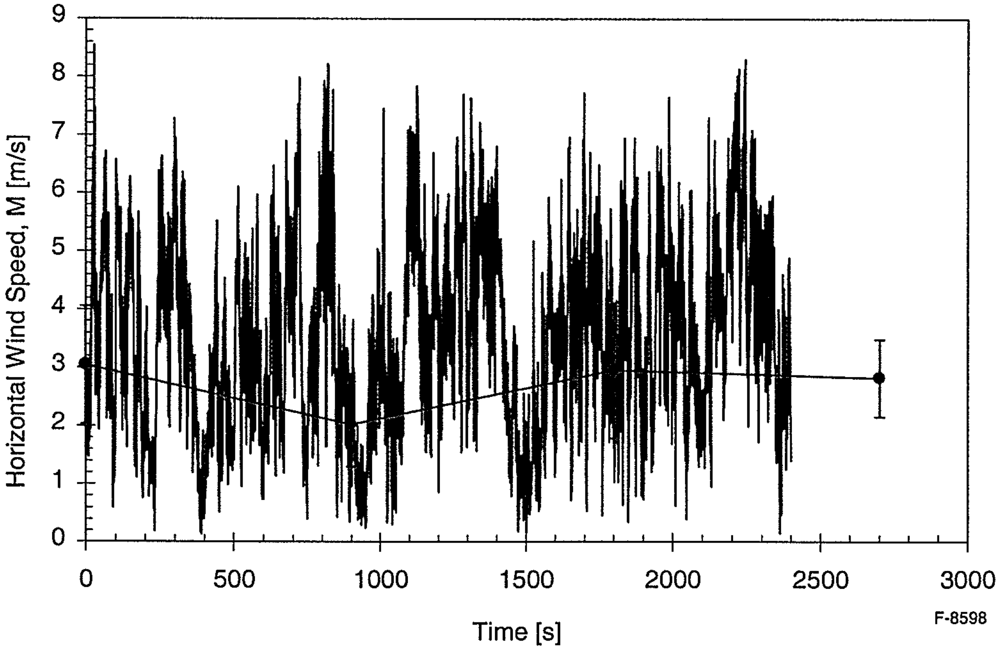

Figure 52. Horizontal wind magnitude temporal history, 13:08 EDT, 22 July 2002 measured by the sonic anemometer (blue) and by the cup anemometer at 24 m (red).

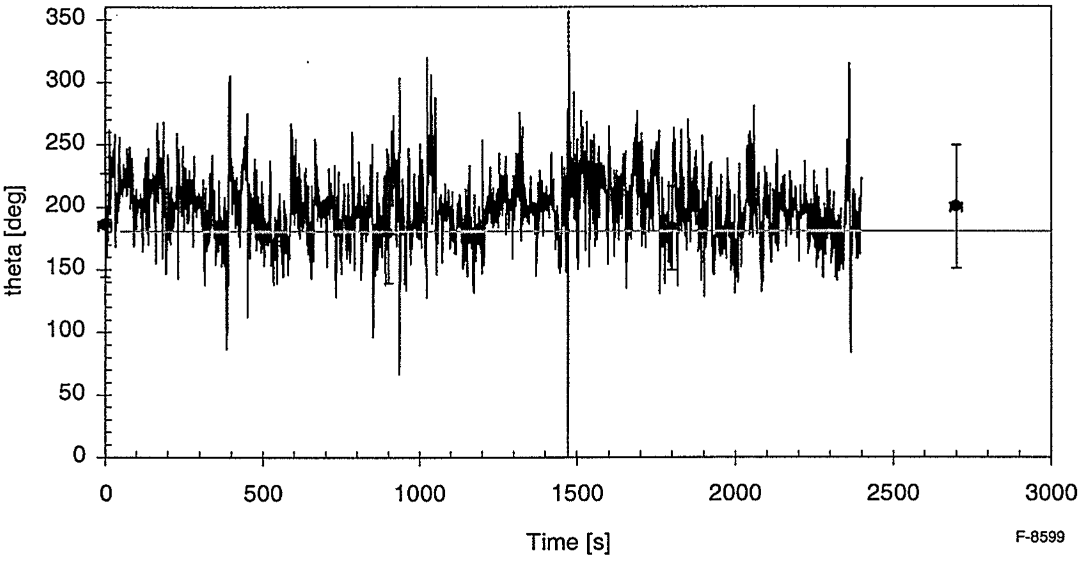

Figure 53. Horizontal wind direction temporal history, 13:08 EDT, 22 July 2002 measured by the sonic anemometer (blue) and cup anemometer at 24 m (red). The yellow line indicates 180 deg (south).

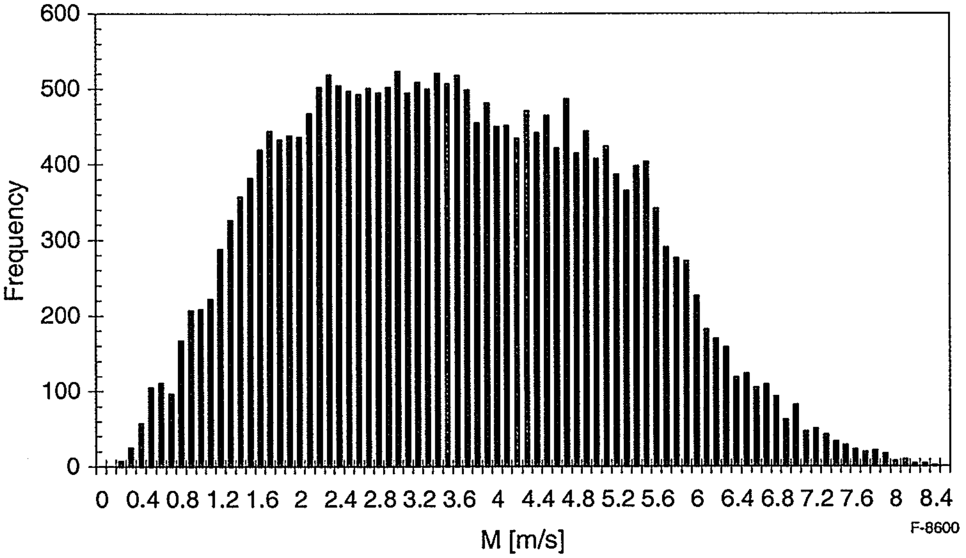

Figure 54. Histogram of the horizontal wind magnitude, 13:08 EDT, 22 July 2002 measured by the sonic anemometer.

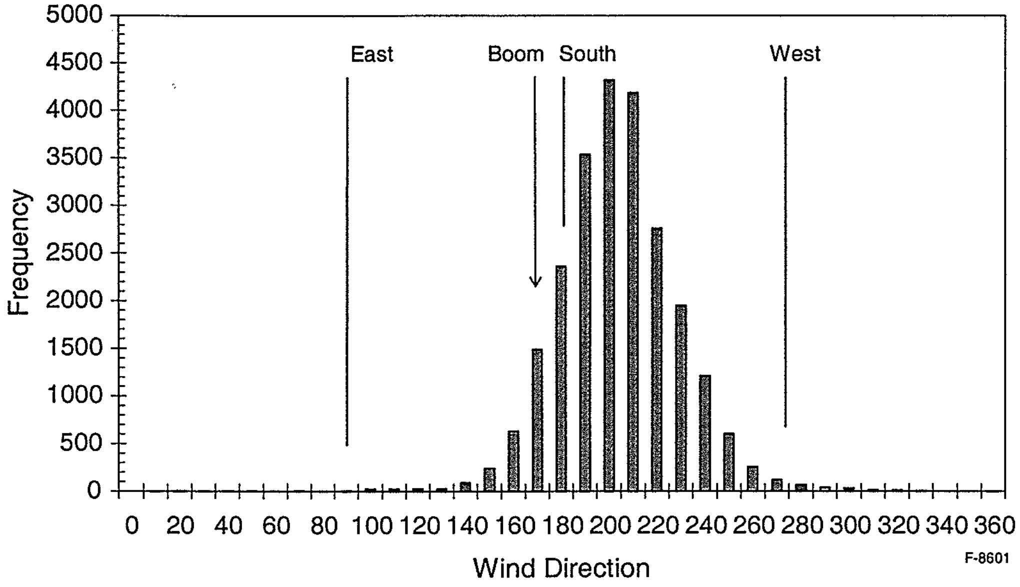

Figure 55. Histogram of the horizontal wind direction, 13:08 EDT, 22 July 2002 measured by the sonic anemometer.

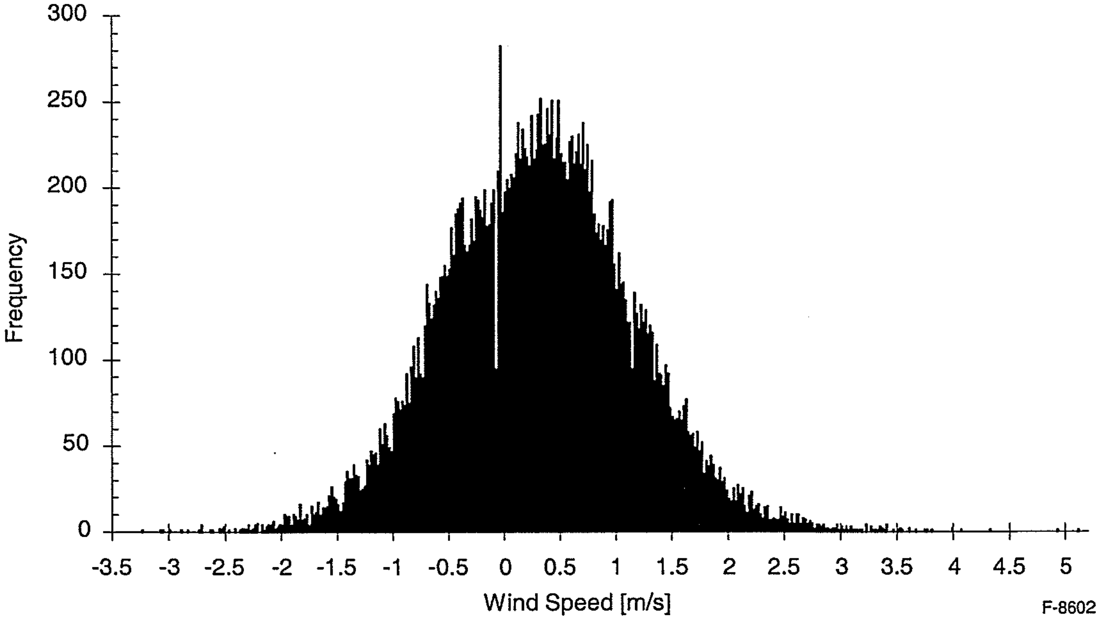

Figure 56. Histogram of the vertical wind magnitude, 13:08 EDT, 22 July 2002 measured by the sonic anemometer.

After calculating 300 second running averages for each of the variables (CO_2 concentration for each of the laser and NDIR channels, H_2O concentration for each of the laser and NDIR channels, T, and W), we calculated the perturbations from the mean. We then calculated power spectra for several of the variables. Figure 57 presents the unweighted power spectrum for w'. The data indicate that the inertial subrange is characterized by the typical -5/3 exponent for frequencies from 0.0005 Hz all the way to 5 Hz (the Nyquist frequency for this system). There is a noticeable spike in the data at a frequency of 0.00305 Hz (328 sec), which is close to the averaging period of 300 seconds. This spike appears in the power spectra calculated for all the variables. Figure 58 presents the unweighted power spectrum for CO_2' as measured by the TDL sensor. The slope for the inertial subrange here is -1.29 +/- 0.021 (2σ), which is fairly close to -1.67, for frequencies from 0.006 Hz to 1 Hz. For frequencies > 1 Hz, the TDL sensor response power spectrum is flat. This indicates that the noise floor has been reached for these frequencies. The unweighted power spectrum for CO_2' for the NDIR sensor is presented in Figure 59. For this data, the slope of the inertial subrange is -1.61 +/- 0.009 (2σ) and linear response extends all the way to 5 Hz.

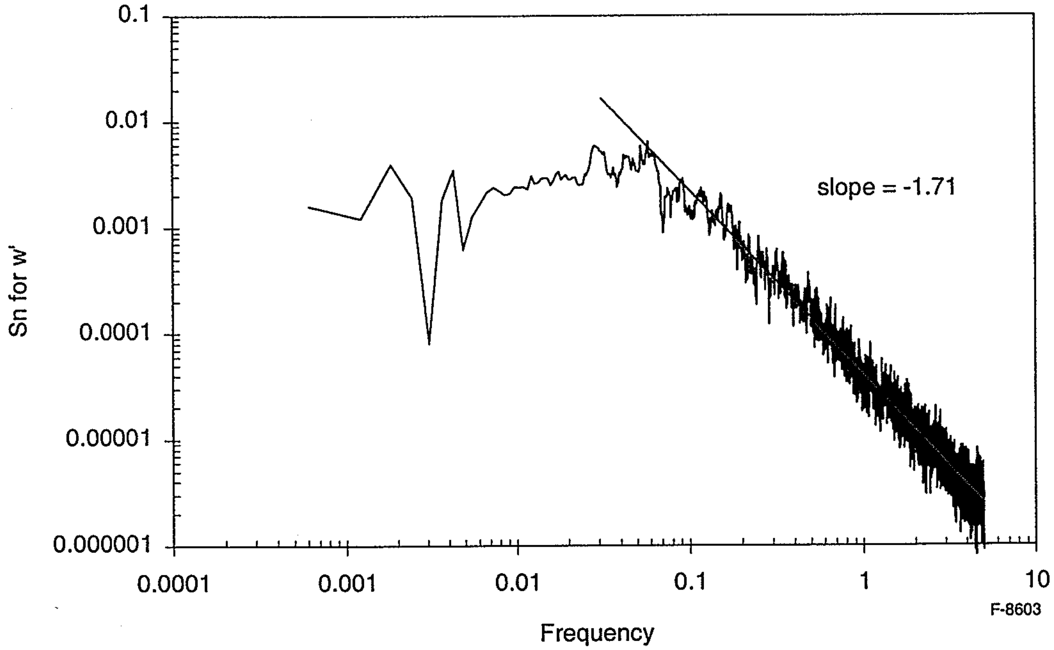

Figure 57. Power spectrum for w', 13:08 EDT, 22 July 2002 measured by the sonic anemometer.

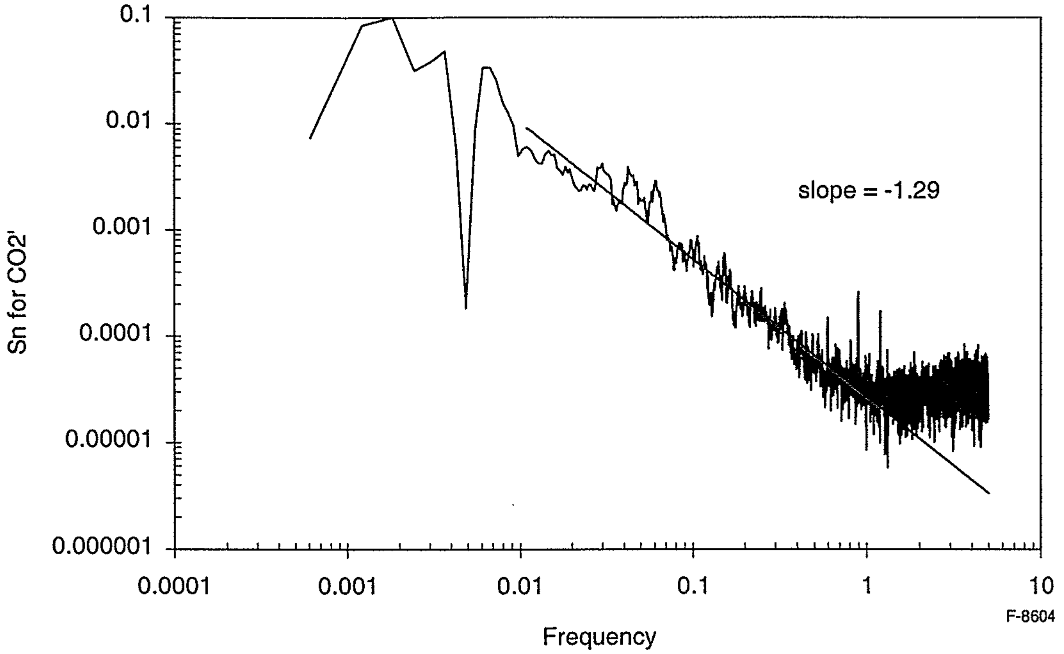

Figure 58. Power spectrum for CO_2’, 13:08 EDT, 22 July 2002 measured by the TDL spectrometer.

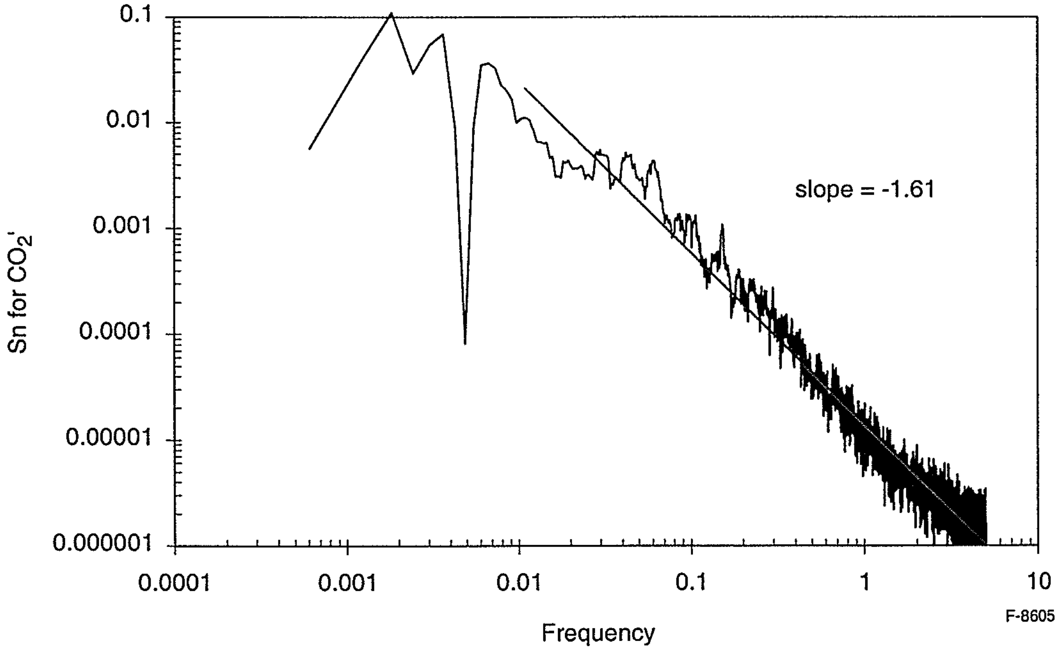

Figure 59. Power spectrum for CO_2’, 13:08 EDT, 22 July 2002 measured by the NDIR sensor.

We next calculated fluxes by taking the product of the pertinent perturbations to create the instantaneous flux and then calculated the 30 min average of the product over the data set to determine the average flux over the data set. The instantaneous flux (w'CO_2'(t) product) for the TDL channel is presented in Figure 60. The w'H_2O'(t) product for the TDL sensor is presented in Figure 61. The w'T'(t) product for the sonic anemometer is presented in Figure 62. Figures 63 through 65 show the same data as Figures 60 to 62, only in higher resolution around 1500 seconds. This highlights several eddies that we observed. Figure 66 presents the CO_2 flux measured by the laser sensor as a function of time of day. The calculated raw fluxes were subjected to the coordinate rotation and Webb corrections as discussed previously. The figure shows the raw flux and the flux after application of each of the corrections. For this data set, the correction provided by the 1st and 2nd coordinate rotations together increased the flux by 29% whereas the correction from the 3rd rotation was very minor. The Webb corrected data was some 37% lower. This magnitude of the Webb correction falls within the experience reported by other investigators.

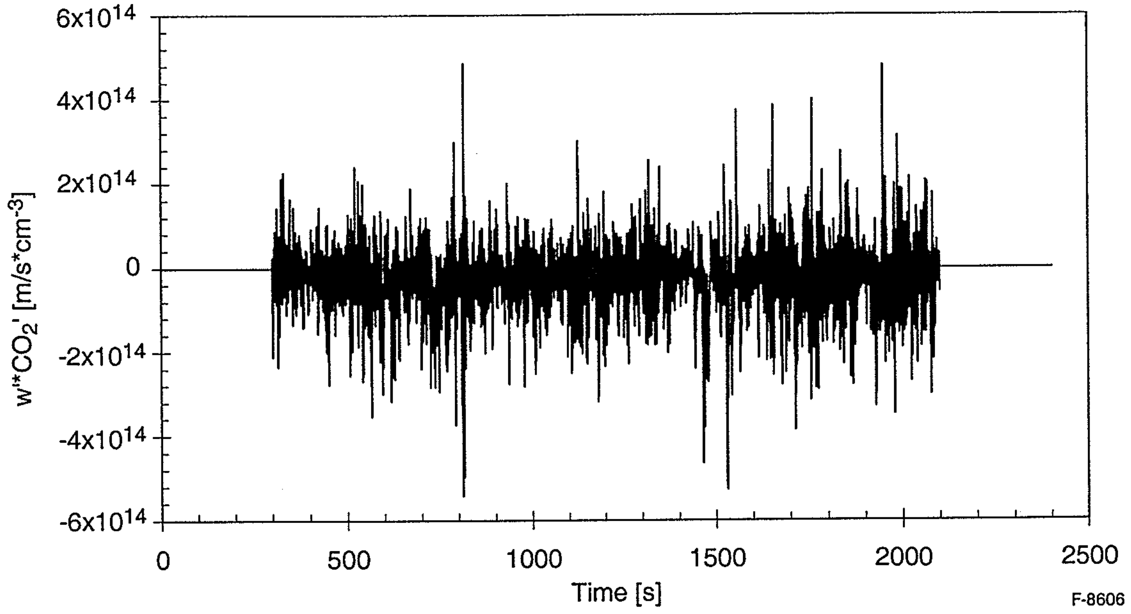

Figure 60. Calculated w'CO_2'(t), 13:08 EDT, 22 July 2002 measured by the TDL spectrometer.

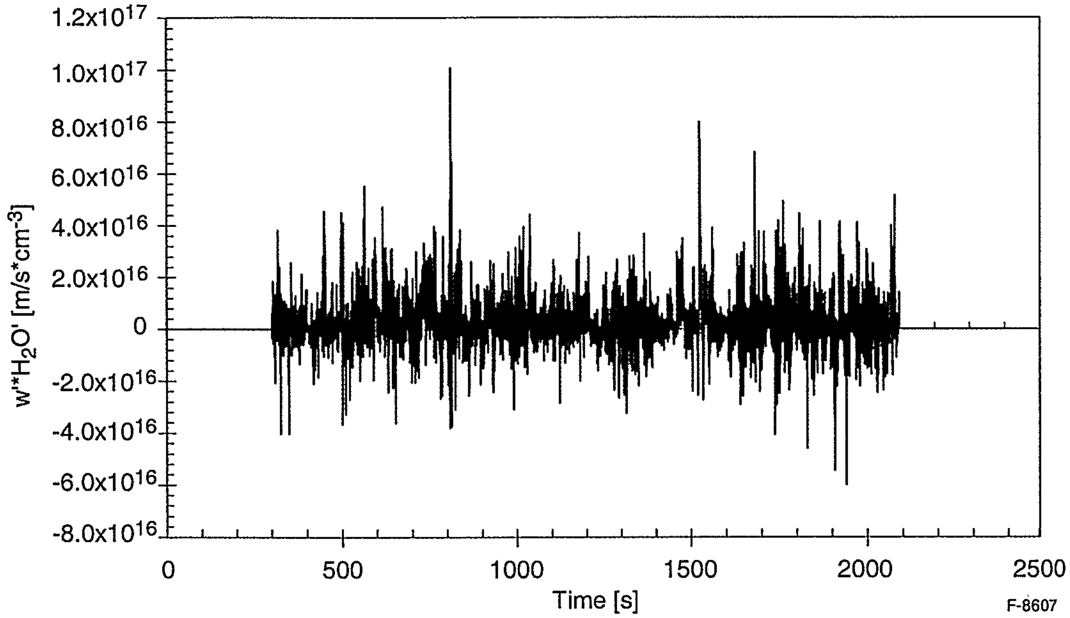

Figure 61. Calculated w'H_2O'(t), 13:08 EDT, 22 July 2002 measured by the TDL spectrometer.

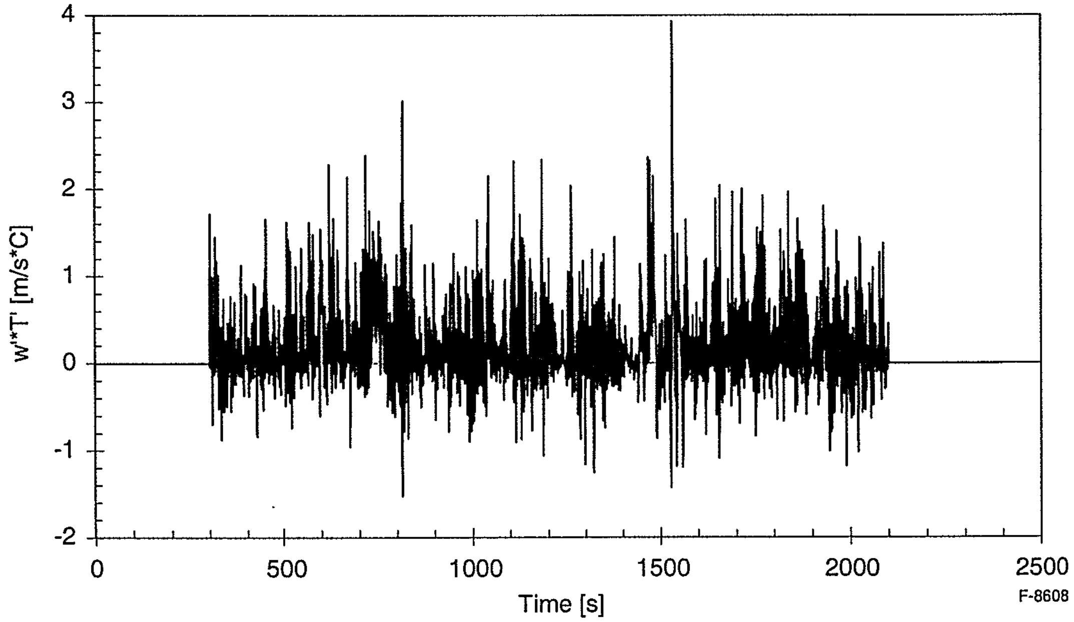

Figure 62. Calculated w'T'(t), 13:08 EDT, 22 July 2002 measured by the TDL spectrometer.

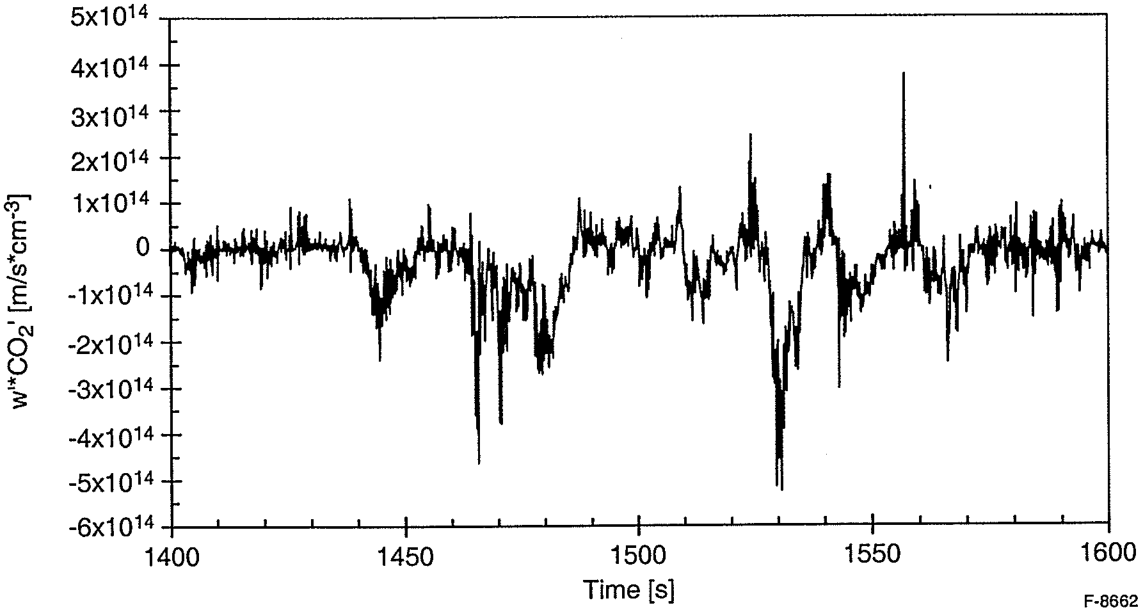

Figure 63. Calculated w'CO_2'(t), 13:08 EDT, 22 July 2002 measured by the TDL spectrometer, expanded scale.

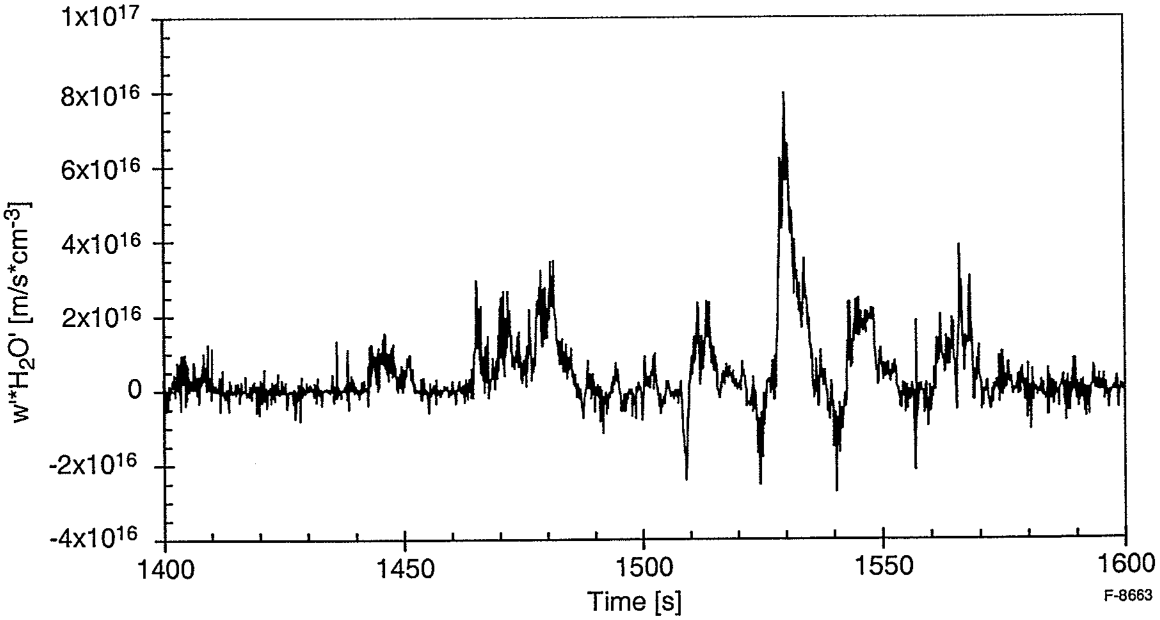

Figure 64. Calculated w'H_2O'(t), 13:08 EDT, 22 July 2002 measured by the TDL spectrometer, expanded scale.

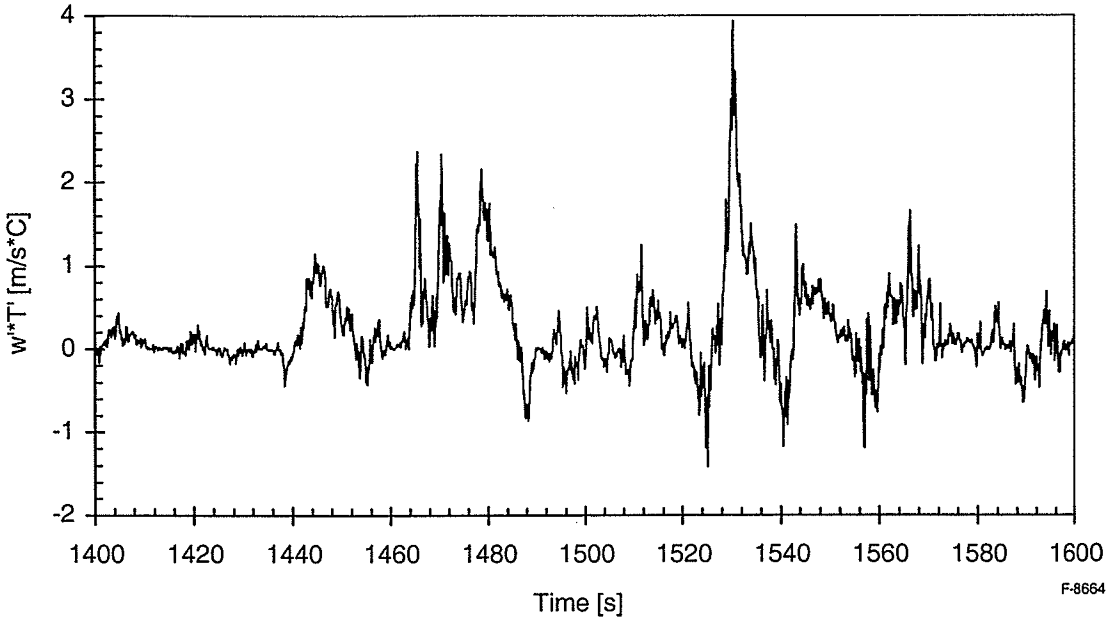

Figure 65. Calculated w'T'(t), 13:08 EDT, 22 July 2002 measured by the TDL spectrometer, expanded scale.

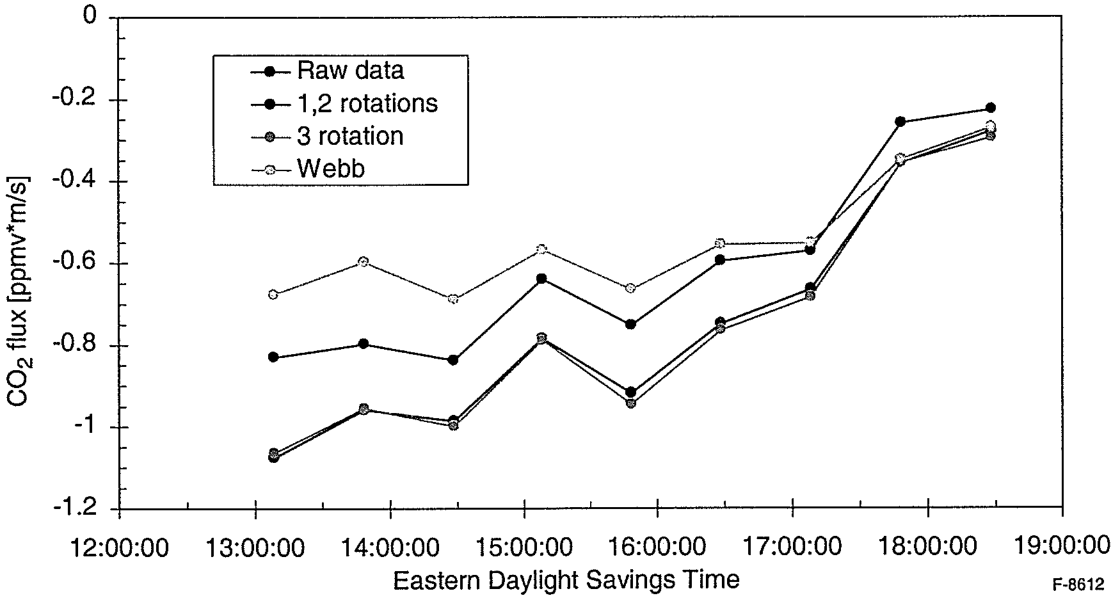

Figure 66. Calculated CO_2 flux (TDL) vs time of day, 22 July 2002. Adjusted results for coordinate rotation and Webb corrections are also plotted.

Figure 67 presents the CO_2 and H_2O fluxes measured by both the TDL and NDIR sensors as a function of time of day. The CO_2 flux is negative as it is a deposition flux (the trees are a sink of CO_2 during times of active photosynthesis) while the H_2O flux is positive (the forest is a source of H_2O). For comparison, Buchmann and Schultz report a Net Ecosystem Assimilation CO_2 flux of $1x10^{-3}$ gm $CO_2/m^2/s$ ($1.37x10^{13}$ CO_2 cm^{-3}*m/s or 0.55 ppmv*m/s at 1 atm and 296 K) for broadleaf deciduous forests.[36] For both species, the TDL sensor reported a larger flux than the NDIR sensor, on average by 48% for CO_2 and by 31% for H_2O. Given the reported measurement precision, the NDIR channel measures flux to better than 10%. In contrast, with a precision of between 0.8 and 1.5 ppmv, the TDL channel measures flux with an error of between 31 and 58%. The NDIR and TDL data sets agree within the error bars of the TDL channel. At this time, we are working to understand these observations. Part of the difference may lay in the way the data was collected. To investigate this difference, we calculated the instantaneous flux by displacing one data set (w' or CO_2') from the other by a fixed temporal offset. We then varied the offset. Figure 68 presents the instantaneous CO_2 flux calculated vs offset for 13:08 EDT, 22 July 2002 for both the TDL and NDIR sensors. The peak value represents the measured flux for this data set. For spatially close-coupled *in situ* sensors, this peak value should occur at zero offset. In contrast, for extractive sampling concentration sensors, the temporal delay incurred by the sample transport time is determined by finding the temporal offset resulting in the peak value from such a plot. The concentration data set must then be corrected for this offset. We see that the TDL instantaneous flux peaks at a temporal offset of -0.7 seconds while that for the NDIR channel peaks at a temporal offset of +0.3 seconds. Similar results were obtained in the correlations of w' with the TDL and NDIR H_2O channels. (The correlation of w' with T' peaks at the expected zero offset as both variables are derived from the sonic anemometer.) The CO_2 TDL channel temporal offset likely arises from the geometry of the sensor suite. Table 8 shows that the separation between the sonic anemometer and the TDL CO_2

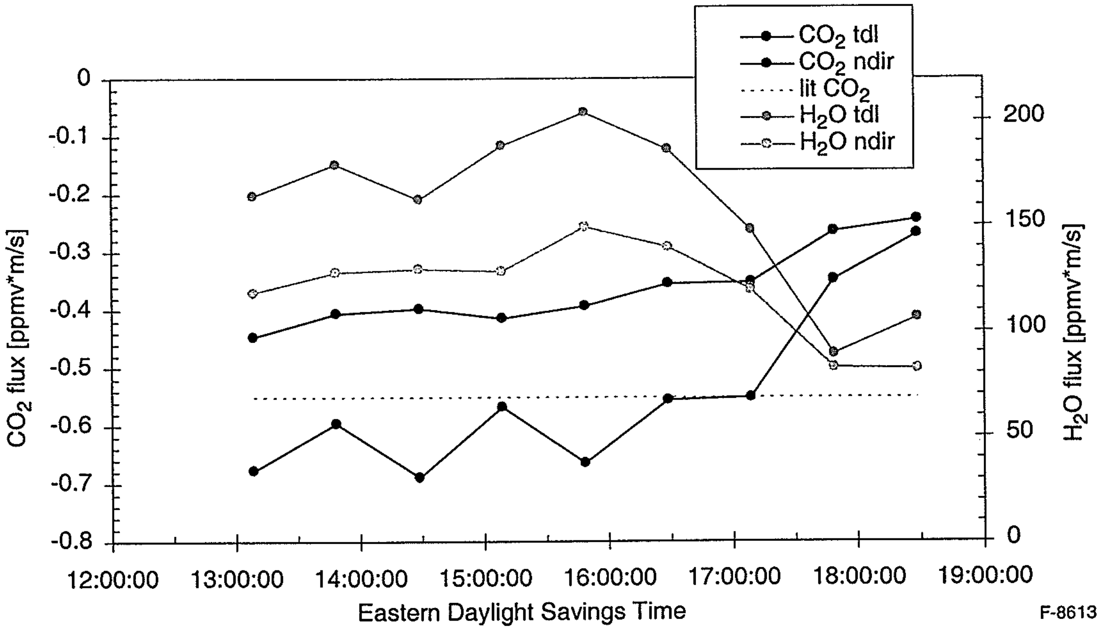

Figure 67. Calculated CO_2 and H_2O fluxes measured by both the TDL and NDIR sensors vs time of day, 22 July 2002.

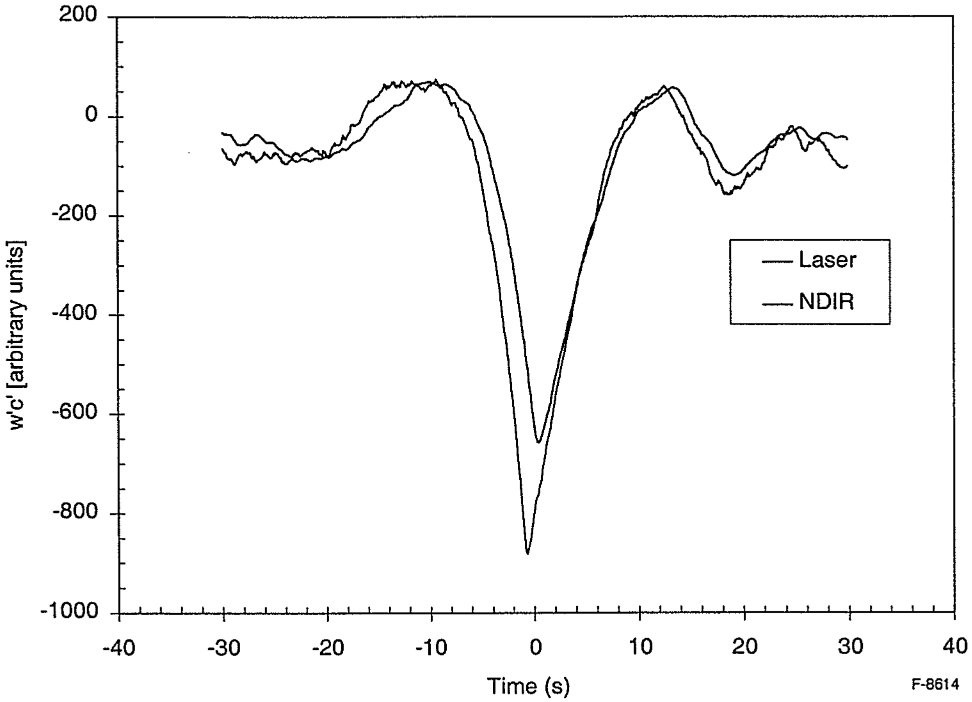

Figure 68. Calculated CO_2 flux (TDL) for 13:08 EDT, 22 July 2002 as a function of temporal delay between the vertical wind and concentration sensor data.

head was 72.6 cm. Figure 54 shows that the average wind speed was between 2 and 5 m/s for this data set. This would result in a simple transport time of between 0.36 to 0.15 seconds. The measured offset is reflecting to some extent the transport time between the two sensors, which now appear to have been too widely separated. The offset is negative because the TDL sensor was triggering the sonic anemometer. The NDIR sensor was not triggered by the TDL sensor, but was "freewheeling." The manual for the LI-7500 NDIR sensor states that there is a fixed throughput delay of 230 ms for this device. This is the time delay between when the data is taken and when it is logged and appears at the RS232 output. Since both concentration sensors were approximately equally spaced behind the sonic anemometer, we expect that the temporal offset for both should be equal except that the value for the NDIR should be slightly more positive due to its fixed temporal offset. This is not what the data in the Figure 68 show. (We expect the overall delay for the NDIR data would be -0.7 + 0.3 = -0.4 seconds). While the fluxes reported in Figure 67 were calculated at 0 offset, we see from Figure 68 that the peak fluxes for both channels were actually higher but the ratio of the two remains almost the same when the temporal corrections are made. We note that, since the perturbations are linear functions of the concentration, if one of the two sensors had somehow lost its calibration, the ratio of the perturbations would be directly affected. However, the ratio of the TDL CO_2 concentration to that of the NDIR CO_2 concentration was 1.00 +/- 0.02 (2 σ) for this data set, while the ratio of the TDL H_2O concentration to that of the NDIR H_2O concentration was 1.01 +/- 0.04 (2 σ) for this data set. A second possibility for the difference between the TDL and NDIR reported fluxes may be that the TDL head was being "shaded" by the sonic anemometer head, given the average wind direction for this data set.

Finally, Figure 69 shows the normalized, calculated CO_2 flux plotted together with the measured photosynthetically active radiation (PAR) measured by the tower sensor. The magnitude of the CO_2 sink tracks the PAR very well. The calculated sensible heat flux <w'T'> vs time of day is presented in Figure 70.

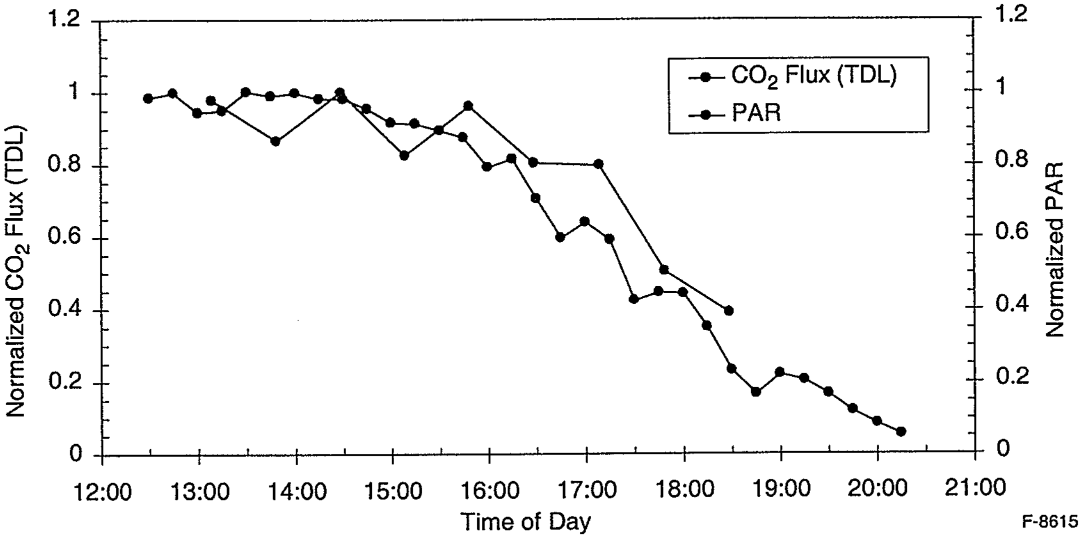

Figure 69. Calculated CO_2 flux (TDL sensor) plotted along with measured PAR vs time of day, 22 July 2002.

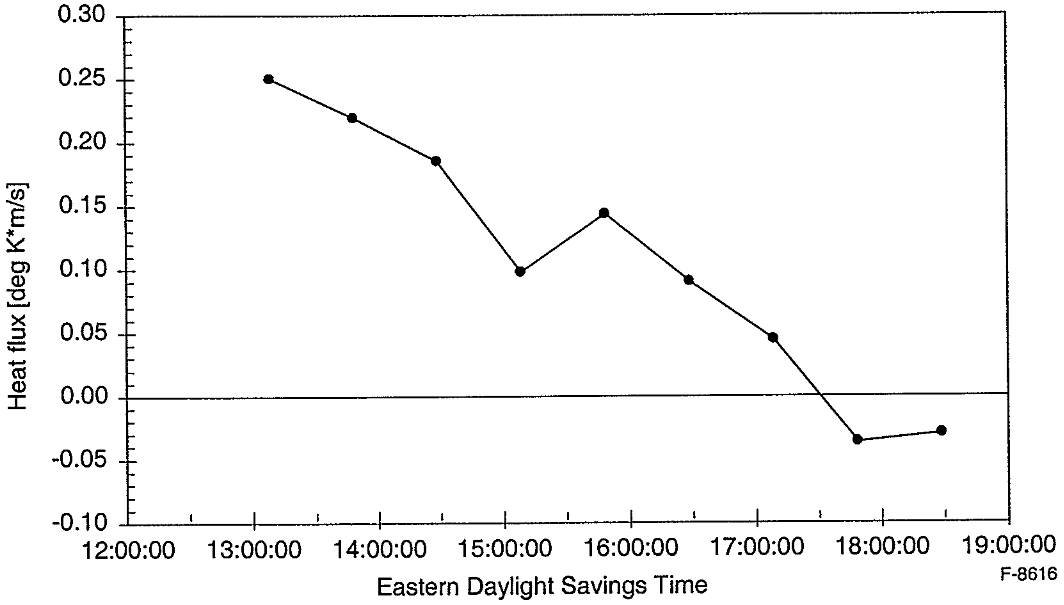

Figure 70. Calculated heat flux (sonic anemometer) vs time of day, 22 July 2002.

We did investigate the magnitude of the calculated flux (TDL sensor) as a function of the averaging period. We varied the averaging period from 300 to 1000 sec. The results are presented in Figure 71. Over the investigated averaging period, the calculated CO_2 flux varied by 14% while the calculated H_2O flux varied by 12%. Thus we did not find a large effect. We also investigated the averaging method on the magnitude of the calculated flux. Perturbations can also be calculated from a mean determined by using a high pass, digital recursive filter:

$$\overline{c}_i = \alpha\,\overline{c}_{i-1} + (1-\alpha)c_i \tag{15}$$

$$\alpha = \exp(-\Delta t/\Gamma) \tag{16}$$

where $\overline{c}_i$ is the current value of the average of c, $\overline{c}_{i-1}$ is the previous average, c_i is the instantaneous value of the concentration, Δt is the sampling resolution (0.1 s), and Γ is the averaging period. For equal periods (300 seconds), we found only a 3% difference in the calculated CO_2 flux (TDL sensor) for the 13:08 EDT, 22 July 2002 data set. Thus, we processed all the data using the linear running average with a 300 second period.

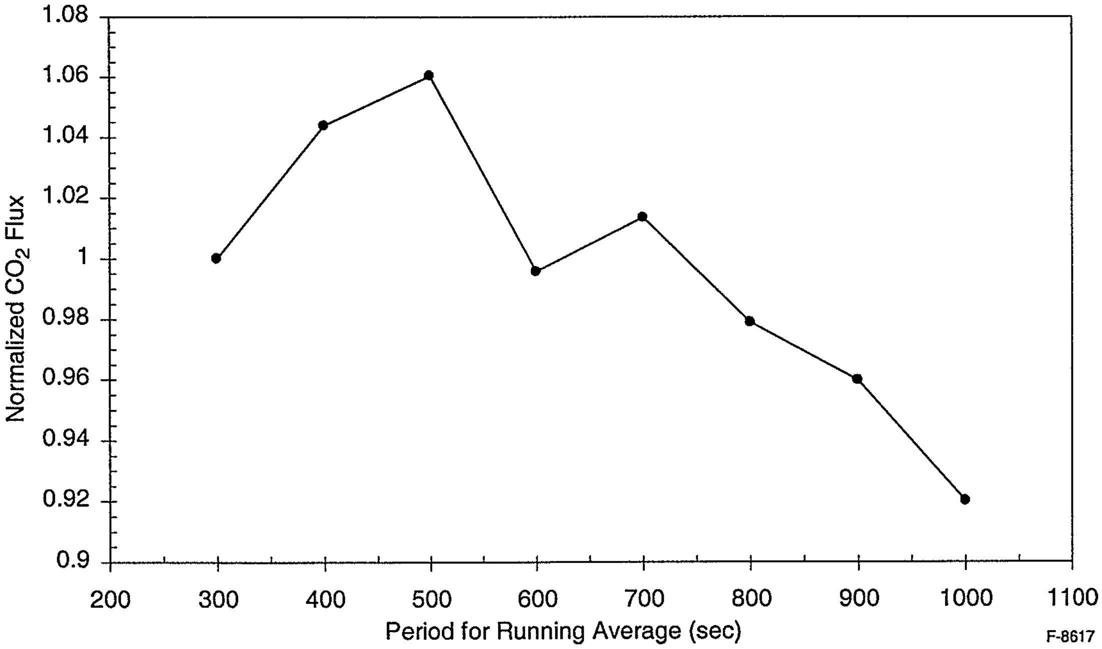

Figure 71. CO_2 flux (TDL sensor) calculated as a function of averaging period, 13:08 EDT, 22 July 2002.

We also carried out an exercise to calculate the fluxes using a different procedure. This procedure capitalized on the fact that the TDL sensor measures concentration of absorbers directly, including a high speed concentration determination of water vapor. We calculated mixing ratios for CO_2 in dry air using the air data measured by the pressure and wind sensors as outlined below. This then precluded the need to apply the Webb corrections to the computed flux.

1. Calculate total air density, ρ, using the pressure as measured by the Vaisala sensor, $P_{Vaisala}$ and the temperature as reported by the sonic anemometer, T_{sonic},
$$\rho = \frac{P_{Vaisala}\,1000}{k\,T_{sonic}}$$

2. Calculate the dry air density using the measured laser water vapor density,
$$\rho_{las}^{a} = \rho - \rho_{las}^{H2O}$$

3. Calculate the dry air density using the measured NDIR water vapor density,
$$\rho_{lic}^{a} = \rho - \rho_{lic}^{H2O}$$

4. Calculate the mixing ratio of CO_2 as measured by the laser and NDIR sensors,
$$X_{las}^{CO2} = \frac{c_{las}^{CO2}}{\rho_{las}^{a}} \text{ and } X_{lic}^{CO2} = \frac{c_{lic}^{CO2}}{\rho_{lic}^{a}}$$

5. Calculate the running means of CO_2 as measured by the laser and NDIR sensors,
$$\overline{X}_{las}^{CO2} \text{ and } \overline{X}_{lic}^{CO2}$$

6. Calculate the perturbations from the running means for both sensors,
$$X_{las}'^{CO2} = X_{las}^{CO2} - \overline{X}_{las}^{CO2} \text{ and } X_{lic}'^{CO2} = X_{lic}^{CO2} - \overline{X}_{lic}^{CO2}$$

7. Calculate the fluxes from the perturbations for both sensors,
$$F_{las}^{CO2} = \overline{\rho}_{las}^{a}\, w' X_{las}'^{CO2} \text{ and } F_{lic}^{CO2} = \overline{\rho}_{lic}^{a}\, w' X_{lic}'^{CO2}$$

8. For H_2O, the mixing ratios as measured by the laser and NDIR sensors are,
$$X_{las}^{H2O} = \frac{c_{las}^{H2O}}{\rho} \text{ and } X_{lic}^{H2O} = \frac{c_{lic}^{H2O}}{\rho}$$
and the flux calculation procedure is then similar to that for CO_2.

9. The fluxes were then processed by the coordinate rotation routines but not by the Webb correction routine.

We found excellent agreement between the fluxes calculated by the two methods. Representative data for 22 July 2002 are presented in Figure 72.

The final calculation we performed with the flux data was to calculate the cospectrum, $C_{w'c'}$, between the vertical wind and CO_2 concentration. The unweighted spectrum is presented in Figure 73. The cospectrum is equivalent to the covariance between W and C. The sum over all the frequency components equals the flux. The spectral amplitudes are negative as expected for a surface sink (deposition flux). We found that integrating the cospectrum over frequency did indeed yield the flux as calculated using the methods described above within a few percent. In addition, as shown in Figure 74, the inertial subrange shows the expected –5/3 slope for frequencies up to 1 Hz.

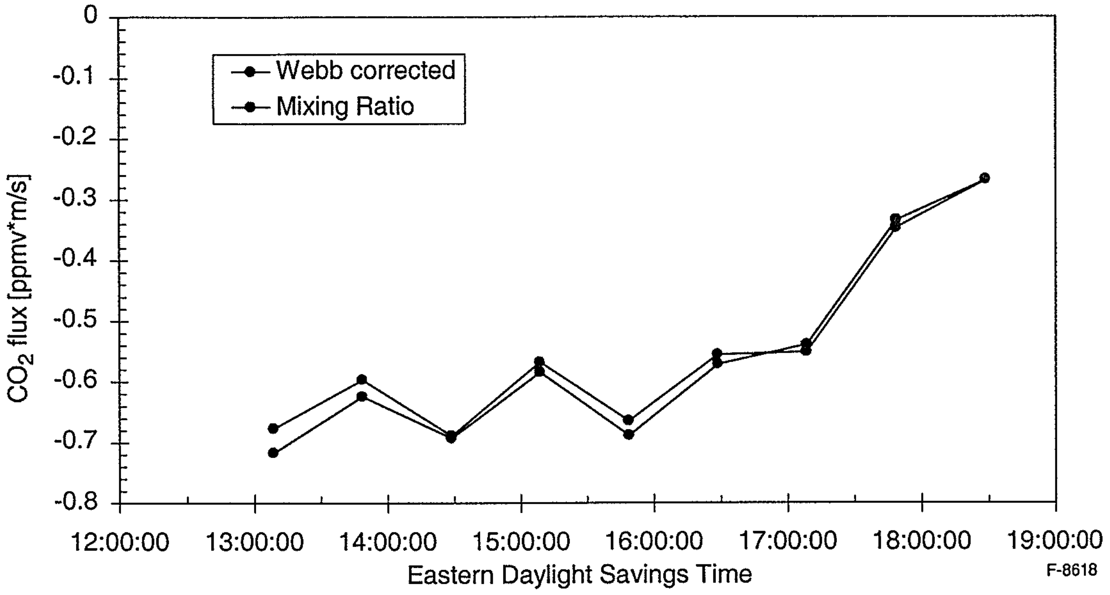

Figure 72. CO_2 flux (TDL sensor) calculated via method 1 vs method 2 plotted vs time of day, 22 July 2002.

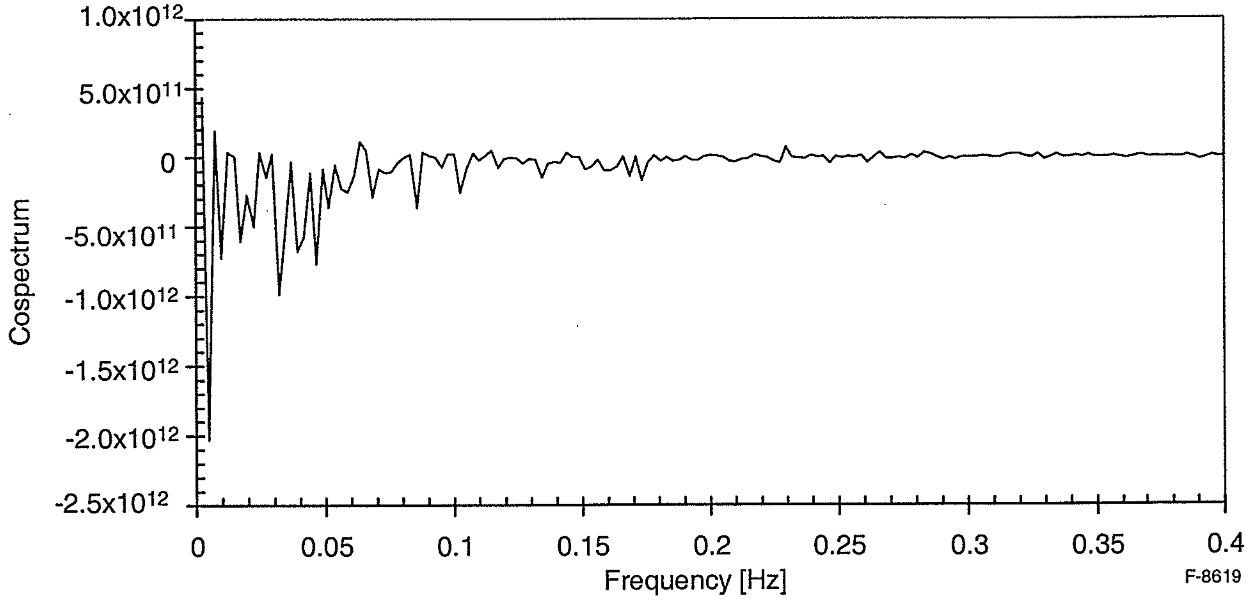

Figure 73. Cospectrum, $C_{w'c'}$, between the vertical wind and CO_2 concentration (TDL) for 13:08 EDT, 22 July 2002.

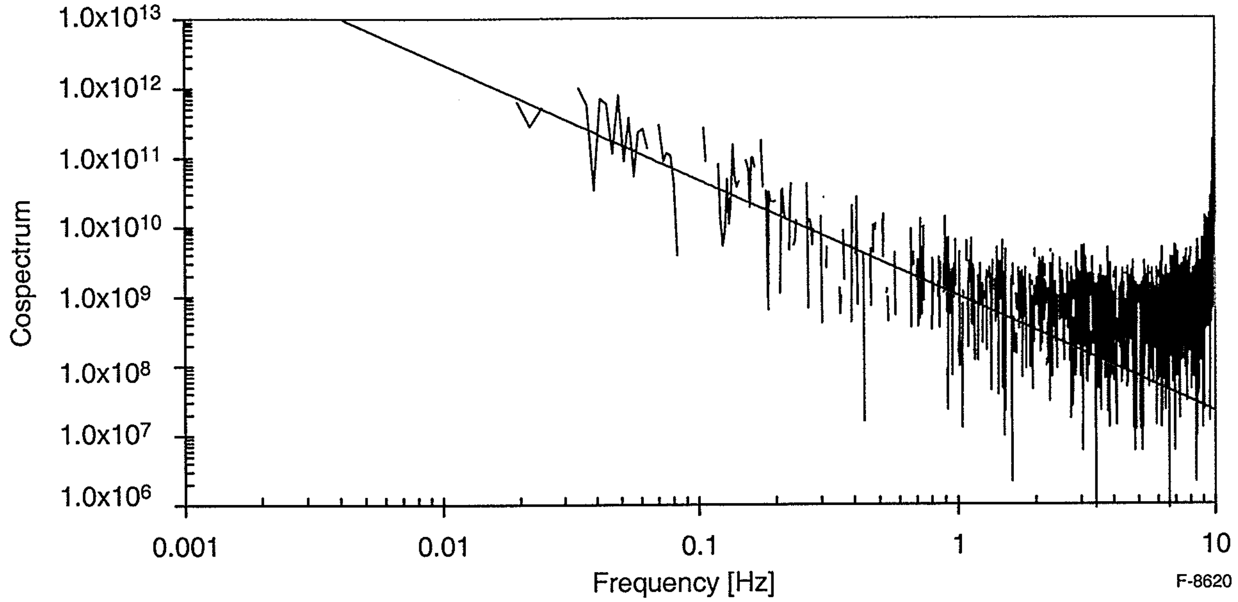

Figure 74. Cospectrum, $C_{w'c'}$, between the vertical wind and CO_2 concentration (TDL) for 13:08 EDT, 22 July 2002. Red trace has a slope of –5/3 and indicates the inertial subrange.

From the measured ancillary data, we calculated several parameters to monitor boundary layer conditions during the course of the afternoon. These parameters included:

Reynold's Stress, $\tau_{\mathrm{Re}\,ynold} = \left(\tau_{xz}^{\;2} + \tau_{yz}^{\;2}\right)^{1/2} = \left(\left(-\bar{\rho}\,\overline{u'w'}\right)^2 + \left(-\bar{\rho}\,\overline{v'w'}\right)^2\right)^{1/2}$ (17)

Friction velocity, u*, $u*^2 = \tau_{\mathrm{Re}\,ynold} / \bar{\rho} = \left(\left(\overline{u'w'}\right)^2 + \left(\overline{v'w'}\right)^2\right)^{1/2}$ (18)

Drag coefficient, $C_D = \left(\frac{u*}{\overline{M}}\right)^2$ (19)

Correlation coefficient, $R_{u,v} = \frac{\overline{u'w'}}{\left(\sigma_u^{\;2} + \sigma_v^{\;2}\right)^{1/2}}$ (20)

Potential temperature, $\theta = T\left(\frac{P_o}{P}\right)^{0.286}$, where P_o is a reference pressure usually = 100 kPa (21)

Potential virtual temperature, $\theta_v = \theta\,(1 + 0.61r)$, where r is the water vapor mixing ratio (22)

Scaled potential temperature, $\theta_* = \frac{-\overline{w'\theta'}}{u_*}$ (23)

Atmospheric parameter, $AP = \frac{\sigma_\theta}{u_* \left|\theta_*\right|}$ (24)

Several of these parameters are presented as a function of time of day in Figures 75 and 76. Generally, conditions in the boundary layer were favorable for eddy flux covariance measurements throughout the afternoon. The atmospheric parameter, for example, varied between 2.6 and 6.4 s/m over the course of the afternoon. Following the analysis of Businger and Delany (as summarized in Figure 1), the instrument concentration resolution (precision) needed to measure a CO_2 flux of 1 x 10^{-3} g CO_2 m^{-2} s^{-1} to 10% precision varied between 0.14 and 0.35 ppmv. This is within the capabilities of NDIR sensor, which has a stated precision of 0.10 ppmv at 10 Hz. (We measured 0.08 ppmv at 10 Hz.) However, the measured TDL instrument precision (1.5 ppmv) was outside this range, which implies that the TDL channel likely was not measuring the flux to 10% precision.

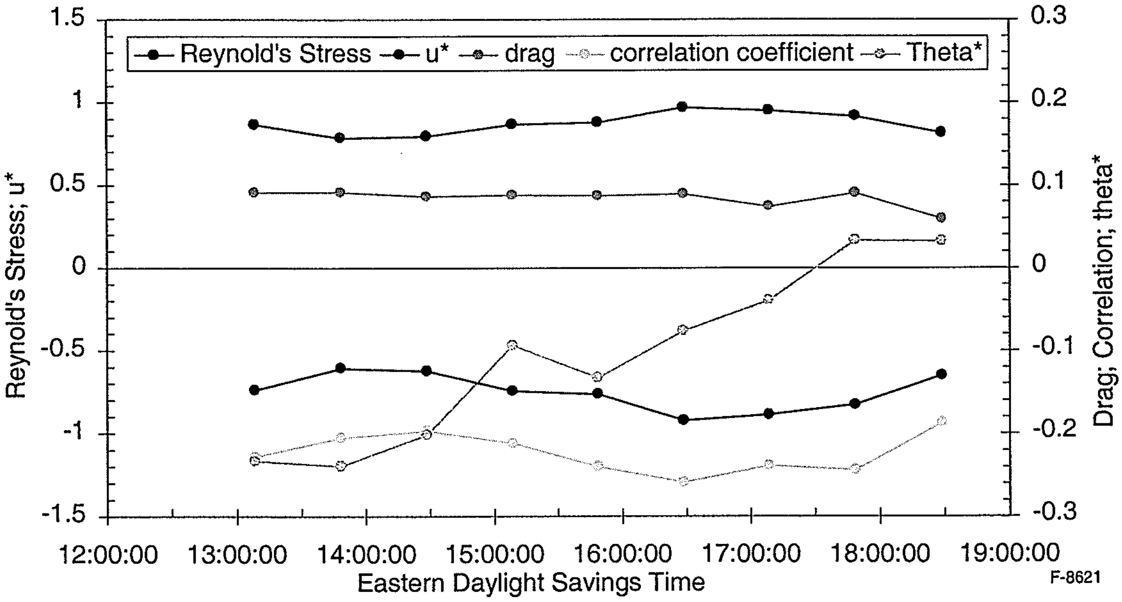

Figure 75. Reynold's Stress, u*, drag coefficient, correlation coefficient, θ_* vs time of day, 22 July 2002.

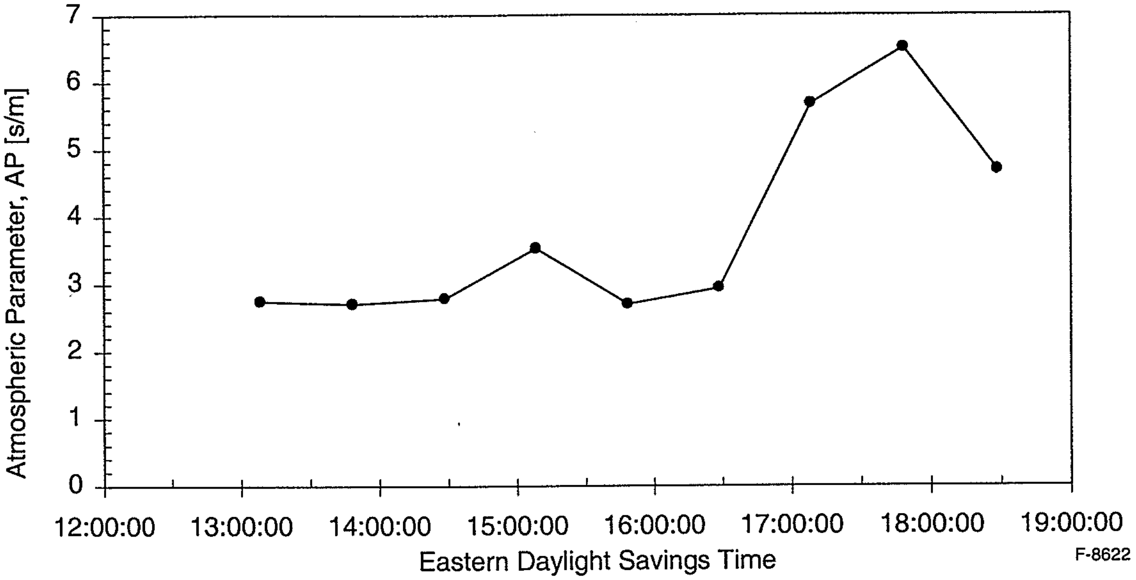

Figure 76. Atmospheric parameter, AP, vs time of day, 22 July 2002.

Finally, we looked at the footprint and fetch of our measurement geometry. The footprint of a flux measurement is the upwind area most likely to influence the downwind measurement of flux at a given height. Schuepp and coworkers have developed analytical solutions to the diffusion equation from which the footprint can be determined.[39] They find that the relative contribution to the vertical flux at height z from an infinitely wide crosswind source (or sink) at an upwind distance x is given by:

$$\frac{1}{Q_o}\frac{dQ}{dx}=-\frac{U(z-d)}{u_* \, k \, x^2}\exp(-U(z-d)/u_* \, k \, x) \tag{25}$$

where Q is the source strength, z is the measurement height above the zero displacement, d, and k is the von Karman constant. This equation defines the one dimensional footprint or relative importance of sources at upwind distances x to the flux measurement at point (x,z). The peak of the footprint (x_{max}) is the area to which the flux at (0,z) is most sensitive. The peak can be described as:

$$x_{\max}=\frac{U(z-d)}{u_* \, 2k} \tag{26}$$

The cumulative normalized contribution to the flux (CNF), at height z, from an upwind area bounded by distance x_L from the point of observation is obtained by integrating Eq. (26) from 0 to x_L:

$$CNF(x_L)=-\int_0^{x_L}\frac{U(z-d)}{u_* \, k \, x^2}\exp(-U(z-d)/u_* \, k \, x)\,dx=\exp(-U(z-d)/u_* \, k \, x_L) \tag{27}$$

This is the so-called fetch of the flux measurement. Figure 77 shows the footprint for our geometry as a function of <M>. The footprint was calculated for a sensor height of 21.9 m and a forest canopy height (zero offset) of 19.8 m. The results show that the peak of our footprint only extended out to a few tens of m under typical conditions. The height of our sensor boom above the canopy (~2 m) was clearly insufficient for achieving a reasonable footprint, as we suspected. The calculated fetch is shown as a function of <M> in Figure 78. These results show that 90% of the measured flux came from distances of < 120 m (<M> = 2 m/s) to < 460 m (<M> = 8 m/s). The tower height would need to be ~ 27 m for a fetch of 1 km (i.e. 90% of the measured flux coming from distances of ≤ 1km). Future such measurements at the Forest Canopy Tower will require increasing the tower height by several stages in order to extend the footprint and fetch to reasonable values.

We had only a very limited amount of time to attempt to measure the $^{13}CO_2/^{12}CO_2$ isotope ratio. We installed the large 50 cm base path cell on the tower on Thursday, 25 July and prepared to make measurements during the morning hours on Friday, 26 July. We did not expect to make flux measurements, only concentration measurements, in our first demonstration. The mean horizontal wind was not favorable on Friday, being very high. The mean horizontal wind is plotted in Figure 79. The measured isotope ratio is plotted in Figure 80. The measured ratio was less than the expected value of 0.011, as measured in the lab. We are still working to understand this observation. Within our estimated error bars, we saw no statistically significant change in the measured ratio as the day progressed. As photosynthesis turns on in the morning, the surrounding atmosphere becomes enriched in $^{13}CO_2$ as photosynthesis discriminates against the heavier isotope. Thus, one expects the measured ratio to increase with time during the day.

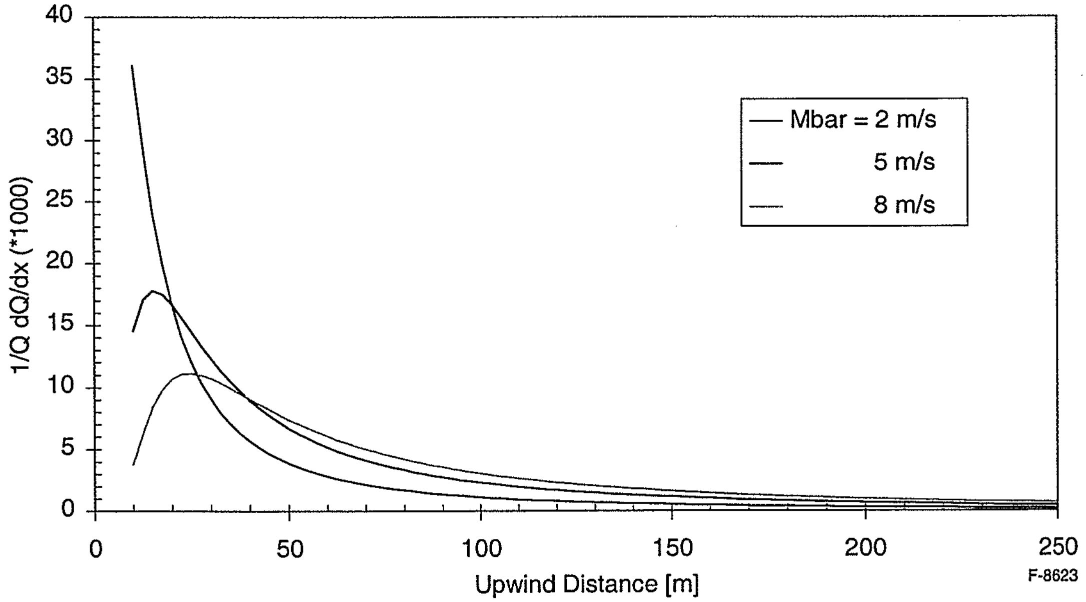

Figure 77. Footprint as a function of <M>.

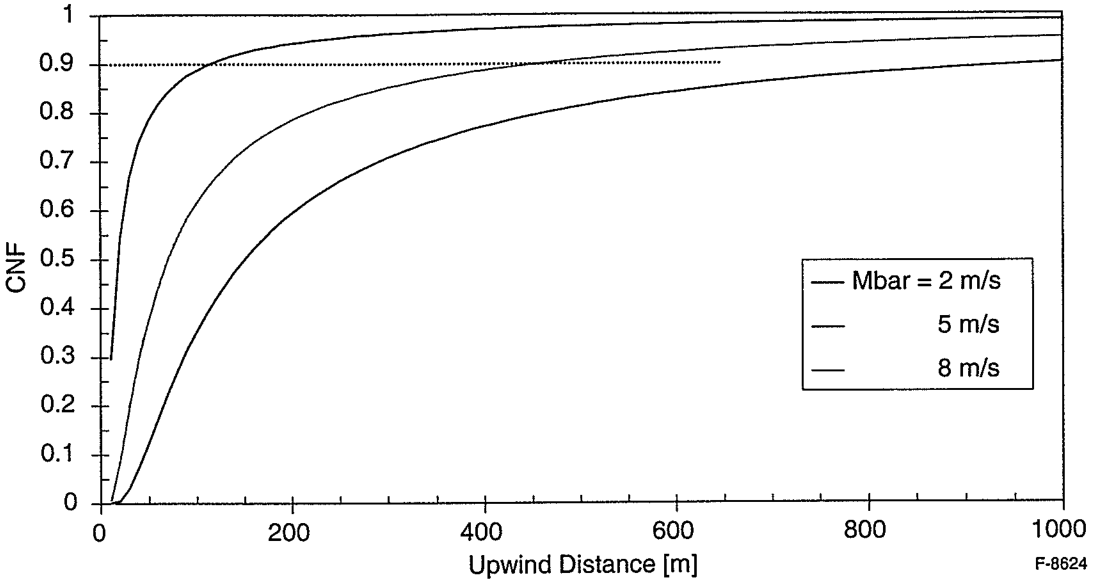

Figure 78. Fetch as a function of <M>.

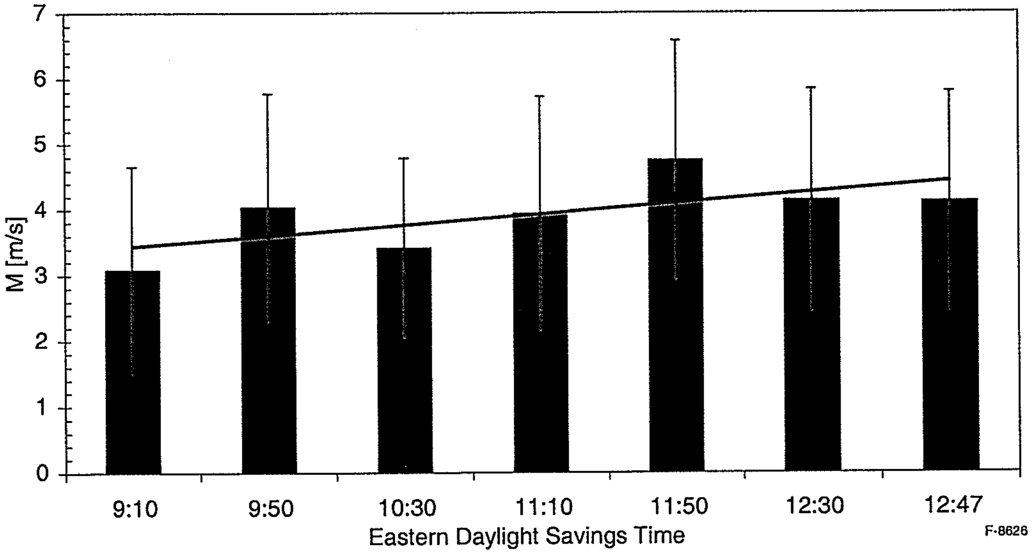

Figure 79. <M> vs time of day, 26 July 2002.

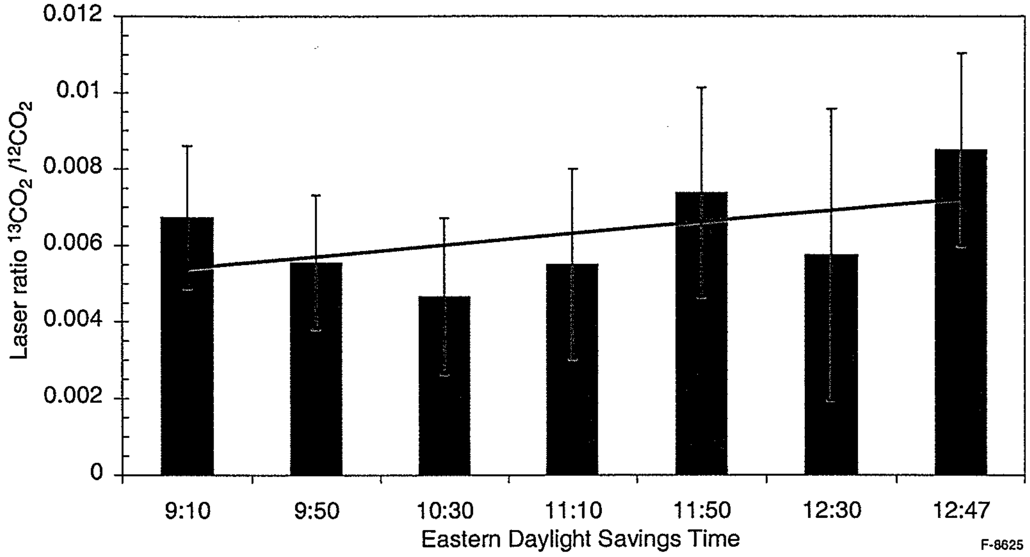

Figure 80. Isotope ratio $^{13}CO_2/^{12}CO_2$ vs time of day, 26 July 2002.

However, the dilution of this ratio by diffusion and turbulent mixing from the large mean horizontal wind may have led to our lack of observation of a meaningful change. The high horizontal wind did increase the noise on the CO_2 data as beam steering by density gradients adversely affected the alignment of the large cell and steered the beam spot around the face of the active region of the signal photodiode. It is very likely that our precision was insufficient to measure a change in the isotope ratio.

8.4 Lessons Learned from Field Demonstrations

We found that the hardware improvements made between the 1st and 2nd demonstrations increased our CO_2 precision so that we were able to successfully measure fluxes. These improvements included the new 2 μm laser (enabled monitoring of stronger lines), larger detectors (significantly reduced noise arising from wind-induced beam steering), and better fiber optic cables (more power transmitted to the tower). The added baffles significantly reduced sensitivity to sunlight, although did not remove it entirely. A proposed solution to this problem is to move the detector off axis by 90 deg, as shown in Figure 81. A right angle prism with a narrow bandpass, high reflectivity coating can be used to direct the incoming laser beam to the detector.

The amount of field data collected for the $^{13}CO_2/^{12}CO_2$ ratio measurements was insufficient to form many conclusions on the efficacy of the measurement technique for this application. However, we recently identified a second vendor of custom wavelength TDLs in the spectral region of interest. Nanoplus, GmbH of Gerbrunn, Germany produces lasers operating near 2.04 μm that would allow us to monitor $^{13}CO_2$ transitions that are both stronger and much better isolated than the transition used for our measurements. Figure 6 shows the HITRAN modeled spectrum for natural abundance levels of $^{13}CO_2$ at 296 K and 1 atm pressure. The R22 transition of the $2\nu_1 + \nu_3$ combination band at 2.0394 μm is clearly a better choice for monitoring $^{13}CO_2$. We did purchase a device at this wavelength but did not have time to make any demonstration measurements in the laboratory.

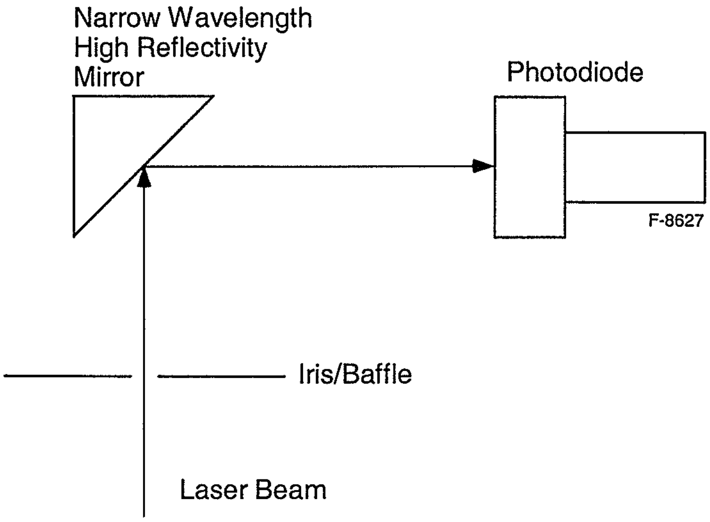

Figure 81. Diagram of optical layout for minimizing sensitivity to scattered sunlight.

9. Technology Commercialization

Li-Cor, a major supplier of NDIR CO_2 and H_2O sensors to the environmental monitoring community, has been the Phase II partner for this program. Interchange meetings with Li-Cor personnel were held on 18 September 2000 and on 23rd February 2001. A final program related meeting was held on 29-30 January 2003. Li-Cor loaned this program a Model 7500 dual channel CO_2 and H_2O NDIR sensor with *in situ*, open path head. The sensor was interfaced with the SPM and was used to intercompare the laser-based sensor results.

In addition to loaning the program an NDIR instrument for field intercomparisons, Li-Cor also conducted a marketing study to determine the magnitude of the world market for a laser-based sensor such as the one developed under this program. Their conclusions are presented in a separate report reproduced in Appendix A. In addition, Li-Cor conducted a design review of the engineering drawings for our laser-based sensor. Their recommendations with respect to manufacturability are presented in a separate report reproduced in Appendix B.

10. References

1. J.T. Houghton, et al., (eds.), *Climate Change, Science of Climate Change, Technical Summary*, pp. 9-97, Cambridge Univ. Press, New York, 1995.
2. P.J. Sellers, et al., "BOREAS in 1997: Experiment overview, scientific results, and future directions," *J. Geophys. Res., 102*, 28,731-28,769, 1997.
3. K. Trenberth (ed.), *Climate Systems Modeling*, 788 pp., Cambridge Univ. Press, New York, 1992.
4. G.P. Livingston and G. L. Hutchinson, "Enclosure-based measurement of trace gas exchange: applications and sources of error," in *Methods in Ecology, Biogenic Trace Gases: Measuring Emissions from Soil and Water,* P.A. Matson and R.C. Harriss (eds.), 1995.

5. M.L. Goulden, et al., "Measurements of carbon sequestration by long-term eddy covariance: Methods and a critical evaluation of accuracy," *Global Change Biol., 2*, 169-182, 1996.
6. R.T. McMillen, "An eddy correlation technique with extended applicability to non-simple terrain," *Boundary Layer Meteorol., 43*, 231-245, 1988.
7. D.D. Baldocchi, B.B. Hicks, and T.P. Meyers, "Measuring biosphere-atmosphere exchanges of biologically related gases with micrometeorological methods," *Ecology, 69*, 1,331-1,340, 1988.
8. R.L. Leuning and M.J. Judd, "The relative merits of open- and closed-path analysers for measurement of eddy fluxes," *Global Change Biol., 2*, 241-254, 1996.
9. M.L. Goulden, et al., "Physiological responses of a black spruce forest to weather," *J. Geophys. Res.*, *102*, 28,987-28,996, 1997.
10. D. Fitzjarrald et al., "Daytime turbulent exchange between the Amazon forest and the atmosphere," *J. Geophys. Res., 95*, 16,825-16,838, 1990.
11. S.C. Wofsy, et al., "Net exchange of CO_2 in a mid-latitude forest," *Science, 260*, 1,314-1,317, 1993.
12. D.D. Baldocchi and C.A. Vogel, "Energy and CO_2 flux densities above and below a temperate broad-leaved forest and a boreal pine forest," *Tree Physiol., 16*, 5-16, 1996.
13. D.E. Anderson, S.B. Verma, and N.J. Rosenberg, "Eddy correlation measurements of CO_2, latent heat, and sensible heat over a crop surface," *Boundary Layer Meteorol., 29*, 263-272, 1984.
14. P.M. Lafleur, "Evapotranspiration from sedge-dominated wetland surfaces," *Aquatic Botany, 37*, 341-353, 1990.
15. S.B. Verma et al., "Eddy correlation measurements of methane flux in a northern peatland ecosystem," *Boundary Layer Meteorol., 58*, 289-304, 1992.
16. D.L. Auble and T.P. Meyers, "An open-path, fast response infrared absorption gas analyzer for H_2O and CO_2," *Boundary Layer Meteorol., 59*, 243-256, 1992.
17. J.A. Ritter, et al., "Airborne flux measurements of trace species in an Arctic boundary layer," *J. Geophys. Res., 97*, 16601, 1992.
18. S.M. Fan, et al., "Micrometeorological measurements of CH_4 and CO_2 exchange between the atmosphere and Subarctic tundra," *J. Geophys. Res., 97*, 16627, 1992.
19. D.D Baldocchi and T.P. Meyers, "Trace gas exchange above the floor of a deciduous forest 1. Evaporation and CO_2 flux," *J. Geophys. Res., 96*, 7271, 1991.
20. J.R.M. Arah, I.J. Crichton, K.A. Smith, H. Clayton, and U. Skiba, "An automated GC analysis system for micrometeorological measurements of trace gas fluxes," *J. Geophys. Res., 99*, 16593, 1994.
21. B. Galle, L. Klemedtsson, and D. Griffith, "Application of a Fourier transform IR system for measurements of nitrous oxide fluxes using micrometeorological methods, an ultra large chamber system, and conventional field chambers," *J. Geophys. Res., 99*, 16575, 1994.
22. A.E. Suyker, S.B. Verma, and T.J. Arkebauer, "Season-long measurement of carbon dioxide exchange in a boreal fen," *J. Geophys. Res., 102*, 29,021-29,028, 1997.
23. F.G. Wienhold, T. Zenker, and G.W. Harris, "A dual channel two tone frequency modulation tunable diode laser spectrometer for ground-based and airborne trace gas measurements," in *Tunable Diode Laser Spectroscopy, Lidar, and DIAL Techniques for Environmental and Industrial Measurements*, A. Fried, D.K. Killinger, and H.I. Schiff, eds., Proc. SPIE, *2112*, 31, 1994.

24. D.C. Hovde, A.C. Stanton, T.P. Meyers and D.R. Matt, "Methane emissions from a landfill measured by eddy correlation using a fast response diode laser sensor," *J. Atm. Chem., 20,* 141, 1995.
25. M.S. Zahniser, D.D. Nelson, J.B. McManus, and P.L. Kebabian, "Measurement of trace gas fluxes using tunable diode laser spectroscopy," *Phil. Trans. R. Soc. Lond. A, 351,* 371, 1995.
26. G.W. Sachse, J.E. Collins, Jr., G.F. Hill, L.O. Wade, L.G. Burney, and J.A. Ritter, "Airborne tunable diode laser sensor for high-precision concentration and flux measurements of carbon monoxide and methane," in *Measurement of Atmospheric Gases,* H.I. Schiff, ed., Proc. SPIE, *1433,* 157, 1991.
27. F.G. Wienhold, H. Frahm, and G.W. Harris, "Measurements of N_2O fluxes from fertilized grassland using a fast reponse tunable diode laser spectrometer," *J. Geophys. Res., 99,* 16557, 1994.
28. G. Edwards, H. Neumann, G. den Hartog, G. Thurtell, and G. Kidd, "Eddy correlation measurements of methane fluxes using a tunable diode laser at the Kinosheo Lake tower site during the Northern Wetlands Study", *J. Geophys. Res., 99,* 1511, 1994.
29. A.E. Suyker, S.B. Verma, R.J. Clement, and D.P. Billesbach, "Methane flux in a boreal fen: Season-long measurement by eddy correlation," *J. Geophys. Res., 101,* 28637, 1996.
30. Campbell Scientific Inc., Logan, UT.
31. R. Leuning and K.M. King, "Comparison of eddy-covariance measurements of CO_2 fluxes by open- and closed-path CO_2 analyzers," *Boundary Layer Meteorol., 59,* 297-311, 1992.
32. E.K. Webb, G.I. Pearman, and R. Leuning, "Correction of flux measurements for density effects due to heat and water vapor transfer," *Quart. J. Roy. Meteor. Soc., 16,* 85-100, 1980.
33. P.C.D. Hobbs, "Ultrasensitive laser measurements without tears," *Appl. Opt., 36,* 903, 1997.
34. M.G. Allen, K.L. Carleton, S.J. Davis, W.J. Kessler, C.E. Otis, D.A. Palombo, and D.M. Sonnenfroh, "Ultra-sensitive dual-beam absorption and gain spectroscopy: Applications for near-ir and visible diode laser sensors," *Appl. Opt., 34,* 3240, 1995.
35. J.A. Businger and A.C. Delany, "Chemical sensor resolution required for measuring surface fluxes by three common micrometeorological techniques," *J. Atm. Chem., 10,* 399, 1990.
36. N. Buchmann and E-D. Schulze, *Global Biogeochemical Cycles, 13,* 751, (1999).
37. A vibrational state of CO_2 is labeled by the quantum numbers for each of the fundamental vibrational modes (ν_1, ν_2, ν_3 where ν_1 is the symmetric stretch, ν_2 is the bend, and ν_3 is the antisymmetric stretch) as well as the angular momentum quantum number associated with the bending mode, l. Each state is labeled as (ν_1, ν_2, l, ν_3). In addition, there is an accidental Fermi resonance between the vibrational states ν_1 and $\nu_2 = 2\nu_1$. This resonance causes a splitting of the original states into several new states whose wavefunctions are a mixture of the original states. The new states are labeled with an additional identifier, which in the HITRAN notation is r, the ranking index. The value of r ranges between 1 for the highest energy level and $\nu_1 + 1$ for the lowest energy level in unit steps. The perturbed states are labeled then as (ν_1, ν_2, l, ν_3, r). For the $2\nu_1 + \nu_3$ state of interest to this work, r takes on values of 1, 2, or 3. The transitions involved in this work arise out of the ground state to these perturbed states. The situation is the same for $^{13}CO_2$. It has the same vibrational state structure although the band centers are shifted to lower energy by the isotope effect. The transitions are summarized in Table 9.

Table 9. Band Centers for the $2\nu_1 + \nu_3$ Combination Bands near 2 µm

Transition	**$^{12}CO_2$**	**$^{13}CO_2$**
00001→20011	5100 cm^{-1}	4992 cm^{-1}
	1.96 µm	2.00 µm
00001→20012	4978 cm^{-1}	4887 cm^{-1}
	2.01 µm	2.05 µm
00001→20013	4855 cm^{-1}	4750 cm^{-1}
	2.06 µm	2.11 µm

38. C.J. Moore, "Frequency response corrections for eddy correlation systems," *Boundary Layer Meteorol., 37*, 17-35, 1986.
39. P.H. Schuepp, M.Y. LeClerc, J.I. MacPherson, and R.J. Desjardins , "Footprint prediction of scalar fluxes from analytical solutions of the diffusion equation," *Boundary Layer Meteorol., 50*, 355-373, 1990.

APPENDIX A

LI-COR Marketing Report

Market Report

Instruments for Making High Speed Measurements of Carbon-Containing Trace Gases

Submitted to Physical Sciences Inc.

Prepared by
Dayle K. McDermitt
LI-COR Biosciences
4308 Progressive Ave.
Lincoln, NE 68504

December 2, 2002

This report contains CONFIDENTIAL AND PROPRIETARY LI-COR INFORMATION
"The following information is Confidential and Proprietary LI-COR INFORMATION and this information is covered by the terms of the PSI/LI-COR MUTUAL NONDISCLOSURE AGREEMENT, signed March, 2000; and the JOINT DEVELOPMENT AGREEMENT between Physical Sciences and LI-COR, effective April, 2001. The parties have agreed to use all necessary means to guard this LI-COR INFORMATION as Confidential and Proprietary."

DISCLAIMER
"LI-COR INFORMATION is hereby provided as a good faith effort to fulfill the obligations of APPENDIX B and APPENDIX C of the JOINT DEVELOPMENT AGREEMENT between Physical Sciences and LI-COR, effective April, 2001. In so providing this LI-COR INFORMATION, LI-COR makes no representation as to its accuracy or utility for making future product or business decisions."

Market drivers

Climate has a major effect on the economic activity and well-being of any nation. It could be argued that the ability to feed and clothe itself are the most basic requirements of any society, even above defense; for we can live without freedom, but we cannot live without food and shelter. Along with soil quality, the climate variables temperature, precipitation, radiation and wind are some of the most important factors affecting plant growth and agriculture. Climate has other important impacts on societies as well. Sea levels, storm frequencies, storm intensities, and weather patterns affect our lives and the economies of nations in many ways. It is the importance of these considerations that provides the social imperative driving research in global warming and climate change.

The energy balance of the earth and climate are strongly affected by the temperature of the atmosphere. While the atmosphere is largely transparent to incoming shortwave solar radiation, the earth's surface absorbs it, is warmed, and reemits radiation at longer wavelengths in the mid-IR. The reemitted radiation is then absorbed by heteronuclear compounds in the atmosphere, trapping it as vibrational – rotational energy, and warming the atmosphere. This so-called "greenhouse warming" has the effect of warming the atmosphere about 30 C higher than it would be without greenhouse gases (GHGs) [1]. This has a profound effect on the state of water at the earth's surface and on all life on the planet.

There are three principal naturally occuring greenhouse gases: CO_2, H_2O and ozone, although, methane and nitrous oxide (N_2O) also occur in small natural abundance and make significant contributions to greenhouse warming. Of these, CO_2 is most important. According to the Intergovernmental Panel on Climate Change report [2], CO_2 levels have increased from about 280 ppmv prior to the industrial revolution, to about 364 ppmv in 1997 [1], and it continues to rise at roughly 0.4% per year due to human activities. Since 1750, it is estimated that methane has increased from about 700 ppbv to about 1760 ppbv today, and N_2O has increased from about 270 ppbv to about 317 ppbv today [2]. Both gases continue to rise sharply. Ozone presents a more complicated story owing to the fact that it is partitioned into a stratospheric component, which has undergone depletion in modern times due mainly to the chemistry of halogenated carbon compounds in the upper atmosphere, and a tropospheric component, which is estimated to have increased by about 36% due to local ozone formation that results from the action of sunlight on NO_x (the sum of NO and NO_2) and VOCs.

These changes have a number of important consequences, but here we focus on global warming and climate change. According to the IPCC [2], over the 20th century there has been a 0.6C increase in the global average surface temperature, and it is likely that the 1990s were the warmest decade and 1998 the warmest year in the past 1000 years. At the same time, the freeze-free season has been lengthened in many mid- and high latitude regions, snow cover in the Northern Hemisphere has been reduced by 10% since the 1960's, summer sea ice and annual duration of lake and river ice cover have been reduced in the Northern Hemisphere, global average sea level has risen 0.1 to 0.2 m, and there have been other possible effects on cloud cover, precipitation, and storm frequency and intensity.

These environmental changes have serious economic implications and it is important to determine if there is a causal relationship between the increase in greenhouse gas concentrations and the climate and environmental changes just enumerated. While the climate and GHG changes over the 20th century seem clear, a causal relationship between them cannot be considered as established unequivocally because of the large interannual variability in the climate data, and limitations in our understanding of the atmosphere and climate system [3].

Funding availability

Because of the serious social, economic and political implications of climate change, President Bush announced a new climate change policy on February 14, 2002 that set as a national goal, for the US to reduce greenhouse gas intensity (i.e. how much GHG it emits per unit of economic activity) 18% by 2012 [4].

This policy carries with it unprecedented funding for climate change-related programs. For FY 2003, President Bush is requesting $4,476MM dollars for programs addressing climate change, which represents a $700MM increase over FY2002. As part of this total, the US Global Change Research Program includes $1,714MM, the Climate Change Research Initiative (CCRI) includes $40MM, and the National Climate Change Technology Initiative (NCCTI) includes $1,304MM. A summary of these programs and how funding will be divided among the various government agencies is shown in Table A-1.

Undoubtedly, funding will be available for gas analysis and gas exchange products from many of the funding agencies mentioned in Table A-1; however, I will particularly note the first goal of the CCRI, and the fifth goal of the NCCTI, as stated in an address by Harlan L. Watson, Senior Climate Negotiator and Special Representative, which was delivered under the auspices of the U.S. Department of State[4].

> **CCRI: Understanding the North American Carbon Cycle** – An intensive research effort will be focused on understanding North American terrestrial and oceanic carbon sources and sinks, to improve monitoring techniques, reconcile approaches for quanitifying carbon storage, and elucidate key controlling processes and land management practices regulating carbon fluxes between the atmosphere, land and the ocean.
>
> **NCCTI: Evaluate Improved Technologies for Measuring and Monitoring Gross and Net Terrestrial GHG Emissions.** Private sector investors are reluctant to participate in projects without reliable and credible quanitification of the uncertainties associated with different land management practices. Cost-effective measurement systems will not only

increase the attractiveness of agricultural GHG projects to investors, but can also provide valuable information to individual farmers and ranchers optimizing the use of fuel, fertilizers, and other substances.

The CCRI is focusing on basic science and its funding is coming principally from the Department of Commerce, presumably through NOAA; the NCCTI is funded principally through DOE, with some funding coming through the EPA and USDA. The thrust of the NCCTI research goal seems to be practical monitoring, although research instruments are also envisioned. Overall, *a very large funding initiative has been proposed supporting climate change research.*

Scientific requirements

I believe we can identify three major classes of questions that need to be addressed with instrumentation: (1) carbon balance research, (2) monitoring carbon credits, and (3) air polution research and monitoring. In this report, I will focus on carbon balance research.

The North American Carbon Program (NACP) was recently described in a report to the U.S. Global Change Research Program. Briefly stated, the goals of the NACP were to (1) ...determine the emissions and uptake of CO_2, CH_4 and CO, the changes in carbon stocks, and the factors regulating these processes..., (2) Develop the scientific basis to implement full carbon accounting on regional and continental scales..., (3) Support long-term quantitative measurements of sources and sinks of atmospheric CO_2 and CH_4.... They go on to identify the "Highest Priority Enabling Developments for the NACP." The number one priority on this list is to "*Develop in situ sensor and sampling protocols for aircraft, ocean, tower, and soil and* *vegetation flux measurements of CO_2, CO and CH_4.*" They specifically mention sensors for atmospheric measurements, ocean buoys and soil flux measurements.

The NACP will address carbon sources, sinks and dynamics with a four tiered approach.

Tier 1 involves comprehensive measurements with remote sensing, using satellite imaging and high altitude aerial photography.

Tier 2 involves dense sampling with inventory techniques already conducted by the USDA, including Forest Inventory Analysis (FIA), etc., that use a combination of remote sensing and ground-based measurments.

Tier 3 is a most interesting level. It involves process monitoring at medium-intensity sites. *About 1000 of these sites are planned* in order to obtain adequate coverage of the nation's ecosystems and land-use histories. These are new sites in addition to the AmeriFlux sites that exist today. "Measurements at these sites should address the major processes in the carbon balance, including net primary productivity (NPP), leaf area index, leaf nutrients, soil respiration, ..., and CH_4 flux. *Depending upon technology development, it may be practical to measure C balance with eddy flux at many of these sites*" [5]. This represents an opportunity both for new eddy covariance technology and new sensor technology.

Tier 4 involves mechanistic and process studies at intensive measurement sites. These intensive sites will include the existing AmeriFlux (88 sites), Canada-Flux (7 sites) and NSF Long-Term Ecological Research sites (24 sites), plus others. Eddy covariance measurements will be the center piece at these sites. "Data from flux sites help test physiological models of C exchange and are critical to relating fluxes and remote-sensing data. Companion physiological and ecological measurments enable partitioning carbon fluxes into plant and soil components and reveal mechanisms repsonsible for these fluxes" [5].

But eddy covariance techniques only measure the net flux, they cannot partition the flux into the components that make it up. Knowledge of partitioning is necessary to understand the mechanistic processes that determine how ecosystems respond to changes in CO_2 concentration and climate variables [6]. Without such an understanding, we cannot predict how climate changes will affect the source or sink strengths of ecosystems, or project atmospheric CO_2 concentrations into the future.

Stable isotope data are particularly useful for dissecting net assimilation into gross photosynthesis and respiration. The CO_2 in the atmosphere is made up of about 98.9% carbon-13 and 1.1% carbon-12. Photosynthesis discriminates against $^{13}CO_2$ causing an enrichment of ^{12}C in plant organic matter. The isotopic signature of respiration is determined by the isotopic composition of the organic matter; so the isotopic composition of air surrounding vegetation reflects the bulk air isotopic composition, the rate and isotopic descrimination of gross photosynthesis, and the respiration rate and isotopic composition of the biomass. If the isotopic compositions of the biomass and bulk air are known, then the components of the net carbon exchange rate (gross photosynthesis and respiration) can be computed from the local air isotopic composition and the net flux [6]. Yakir and Wang [6] showed that independent estimates of the same variables also could be estimated using ^{18}O in CO_2. But whether with ^{13}C or ^{18}O, these are iNDIRect methods that can only be done in conjunction with gradient techniques to measure the net carbon flux, not with eddy covariance [6], and the best results require sites with high photosynthesis rates under optimal conditions [7]. In forests, eddy covariance offers the best approach for measuring flux, but according to Yakir [7], “Fast responding isotope analyzers with the required precision are not available at present...” so more iNDIRect techniques must be applied. Yakir [7] states that “To date there are still difficulties...” with these methods. Fast response analyzers with the precision required to measure fluxes of the stable isotopes of carbon and oxygen in CO_2 and H_2O would be welcome for obtaining more detailed mechanistic information at the flux sites around the world.

Stable isotope analysis is also widely used for descriminating between oceanic and terristrial sources and sinks for carbon (e.g. Francey, et al, 1995). Flask sampling and mass spectrometry are the methods of choice for this work. Mass spectrometry is also used to determine the isotopic composition of plant tissues and water. Nevertheless, there is a need for faster and lower cost methods here as well.

This need is clearly illustrated by a recent call for proposals sponsored by DOE. The following request was made (Pacific Northwest National Laboratory, 10/25/02): "Grant applications are also sought for unique, rapid, and cost-effective methods for measuring the natural carbon isotopic composition of plant, soil and atmospheric media. The idea is to use isotope technology to identify sources and sinks of carbon materials, and to use carbon isotopes to distinguish relative carbon exchanges between terrestrial or aquatic media and the atmosphere."

In summary, the North American Carbon Program is calling for the development of novel and cost-effective instruments for making rapid measurements of stable carbon isotopes in CO_2 (and methane, if possible), and easier and more cost-effective ways to measure eddy covariance. Also, better instruments are needed for deployment on aircraft, ships, ground stations and tall towers for measuring CO_2, CH_4 and CO.

There are probably similar programs focusing on N_2O because it has about 300 times greater global warming potential (GWP) [9] than CO_2, making it an important GHG, even though it is present in the atmosphere at about a 1000-fold lower concentration. The GWP is defined as the ratio of the time-integrated radiative forcing from the instantaneous release of 1kg of a trace substance relative to that of a 1kg release of CO_2[9]. Oxides of nitrogen (NO and NO_2, or NO_x) and VOCs are also important as GHGs, but perhaps they are even more important as air pollutants due to their affects on ozone formation and human health. These gases can also be detected with IR technologies and deserve further analysis than I can give here.

Instrument requirements

In 2000, 2001 and 2002, we carried out surveys of scientists working in relevant disciplines to determine their requirments and expectations for new instruments that measure trace gases. The surveys were informal and were in the form of questionnaires given at scientific conferences, or in phone interviews. The number of respondents are too small to make quantitative inferences from the samples to the market; however, they do allow us to draw conclusions about what this subset of potential customers are looking for. The greatest response to the survey came from the 6th International Conference on Air-Surface Exchange of Gases and Particles, held in Edinburgh, Scotland, July 3-7, 2000 (11 respondents). The survey was also offered at the Agriculture and Forest Meterology Conference, held in Davis, CA, Aug 2000 (2 respondents), the Ecological Society of America Conference, held in Madison, WI, Aug 2001 (2 respondents), at INTECOL 2002, held in Seoul, Korea (no respondents), and at the American Meterological Society meeting, held in Orlando, FL, Jan 2002 (no respondents).

The survey asked two principal questions:

1. Please list the top three trace gases (or isotopes) you are interested in monitoring, or would like to see monitored.

2. For each gas or isotope you listed above, please indicate desired specifications for a sensor that would monitor that gas or isotope.

> We then gave five categories of specifications for each gas, including sensor measurement range, precision/resolution, response time, accuracy, and the price they would be willing to pay.

We asked additional questions about their perceptions of the market size and applications, but the responses indicated that respondents understood, or misunderstood, the questions in such a variety of ways that the data are not very useful.

A summary of responses to question 1 is given in Table A-2. The respondent's top priority was given a weighting of 3, second priority 2, third priority 1, and the scores were summed for each gas mentioned. In this small sample, the single gas with the highest interest was NH_3, and as a group, it was the NO_x group. The level of interest in N_2O, methane and ozone was equal and about half of that in NH_3. While this small group had considerable interest in nitrogen compounds, we cannot extrapolate this as reflecting the market demand because the sample size is so small.

By contrast, however, we can ask what this group of respondents were looking for in a trace gas analyzer. The results from question 2 are given in Table A-3. The average price quoted is $16,700 but this is skewed by two respondents giving a price of $30,000 for all three sensors. The median is $15,000, which is probably a reasonable target price for this market. There will be some willing to pay $30,000 but they will be in the minority, and there will be some who will be looking for lower cost instruments, especially for monitoring. Only one respondent asked for instruments at a price of $1000 and these only required slow response times for ozone and CO. He indicated he would need multiple instruments for monitoring. In a comment, another respondent said very low cost sensors (about $100) would be useful for monitoring NO_x and methane in buildings.

With regard to performance, there were 46 responses stating response times. Of these, 24 required response times of 10Hz (or .1s) or faster, suggesting that 52% were looking for an instrument with specifications consistent with flux measurements. An additional 5 required 5Hz, which is adequate for flux measurements over forests. Seventeen respondents (37%) were looking for instruments with response times slower than 5Hz, suggesting they would be used either for monitoring or analytical measurements.

There did not seem to be any clear relationship between the gas being measured and the price point or response time requirements. This is reasonable as there is a need for both flux measurements and monitoring for all the gases mentioned, and it seems that a price in the neighborhood of $15,000 is about optimal for all of them. This conclusion is supported by results from a telephone survey we performed recently, in which we asked about the price of the LI-COR LI-7500 Open Path CO_2/H_2O Analyzer (the price of the LI-7500 is $13,400.) Eight of ten respondents indicated the price of that instrument was "ok" or "good," but two said "cheaper..." or "lower is better." However, it is important to note that while a price of $15,000 appears ideal, there are not any technological solutions presently that would enable the design and production of a sensor that would meet both these specification and price requirements. Current technology to measure trace gases is suited only to laboratory usage and costs are multiples times that of instruments such as the LI-7500.

When asked about measurement range, responses varied with the gas being measured as one would expect; however, when precision and accuracy were expressed as a percent of the maximum range, the requirements were similar for all the major gases, and varied widely from 0.01% to about 5%. The average precision for all gases was 1.72% and the median was 0.25%.

The accuracy requirements were also similar for all major gases, varying from 0.03% to 12% of the maximum range, with both the median and average equaling 4.4%.

None of the respondents in this survey mentioned an interest in stable isotope measurements, even though we mentioned them in our questions. This indicates either a lack of interest or a lack of awareness in the groups being surveyed, although it does not reflect a lack of interest or need in the market as a whole. A conference was held in May of this year entitled, Stable Isotopes and Biosphere-Atmosphere Interactions, with 26 invited speakers. I am sure we would have obtained quite a different response if we had performed the survey there. Also, in the same phone survey mentioned previously, we asked respondents to tell us what gases other than CO_2 and H_2O they would like to measure. Two respondents out of ten mentioned stable isotopes. Methane was mentioned most often (4 out 10 respondents), and NO_x, ozone and VOCs were each mentioned by two of ten respondents.

Market size

Since the mid-1990's carbon flux measurements have dominated the sales growth of our gas analyzers. The advent of the LI-COR LI-6262 CO_2/H_2O Analyzer made it possible to routinely measure the net fluxes of CO_2 and water vapor using several different techniques. During the same period networks of research sites dedicated to carbon flux and ecological measurement were established around the world. Table A-4 lists six such flux networks and the approximate number of sites at each as enumerated on their web sites. The actual total may be above 200, based upon information coming from a recent Ameriflux meeting. In addition to these sites, there are 24 Long-Term Ecological Research sites maintained by the NSF. These sites and others like them represent a fundamental metric in assessing the market size for our instruments; however, these numbers do not account for the volume of sales we have experienced over the past 10 years, or so.

Figure A-1 shows a plot of sales over time for our open path and closed path instruments. The surge in total sales and the drop-off in closed path sales in 2000 are coincident with the introduction of the LI-7500 Open Path CO_2/H_2O Analyzer. This revolutionary instrument made open path measurements practical and widely available for the first time, and it caused about a 50% drop in sales of our closed path instruments. Nevertheless, the closed path approach does have its advantages and appropriate applications, and in 2000, we introduced a new closed path instrument, the LI-7000 CO_2/H_2O Analyzer. This instrument has characteristics that make it well-suited to high frequency closed path measurements.

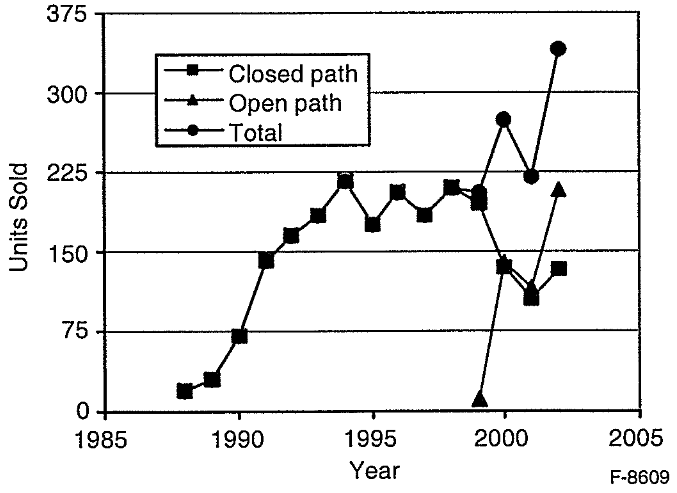

Figure A-1. Sales of closed path and open path analyzers from 1988 to 2002.

So how large is this market place? Total market size estimates are very difficult to attain or predict for the future. However, based on present data available we would estimate that the flux market for any given widely used product will be in excess of 1000 units world-wide over its lifetime. The dollar value of such a market follows immediately from the average selling price.

Funding for climate change research is being increased sharply, and the North American Carbon Program is envisioning establishing 1000 *new* Tier 3 medium intensity sites. According to the NACP plan, net primary productivity, soil respiration, methane and LAI measurements will be made at most of those sites, and C balance with eddy flux measurements will be made at many of them, if appropriate technology is available [5]. This has the potential to expand the market for some classes of instruments by a significant amount. I think the market for stable isotope measurements will grow much larger than it has been in the past, but it will remain a fairly small and specialized field compared to total CO_2 measurements, unless it becomes widely used for monitoring specific CO_2 sources.

Summary and Conclusions

In this analysis, I have attempted to show:

(1) There is a strong world-wide social, political and economic imperative driving climate change research that is based upon a climate change that is probably real and at least partly due to greenhouse gas emissions resulting from human activity.

(2) Funding in the United States has increased sharply to support this research.

(3) There is a need for new sensors for measuring at least CH_4 and CO to support the NACP; there are also sensor needs for N_2O, NO_x, O_3 and NH_3, although I cannot quantify them at present.

(4) Stable isotopes are necessary for dissecting gross productivity and respiration from net fluxes measured by micrometerological methods. It would be useful to be able to measure the flux rates of C-13 and O-18 CO_2 directly.

(5) Stable isotopes are also useful for dissecting terrestrial and oceanic carbon sources and sinks. New sensors are being solicited to support both this and ecological studies.

(6) The optimal price point for instruments capable of making flux measurements in the field is probably near $15,000. However, the technology to produce such a sensor at this price is presently not available.

(7) The precision of such instruments should be 0.25% or better, with accuracy near 4%.

(8) Using CO_2 analyzers as the model, and for sensors with similar scope for flux measurement applications, the market size for a new gas analyzer is probably in excess of 1000 units over its lifetime. This estimate may be too large for carbon isotope analyzers, because the latter represents a specialized niche, as important as it is.

References

1. Ledley, T.S., et al, Climate change and greenhouse gases. EOS 80: 453, 1999.

2. Climate Change 2001: The Scientific Basis, Intergovernmental Panel on Climate Change, Summary for Policymakers. http://www.ipcc.ch/

3. Climate Change Science: An analysis of some key questions. 2001. National Academy Press, Washington, DC. http://books.nap.edu/html/climatechange/notice.html

4. Harlan L. Watson, Evolving U.S. Policy on Climate Change, address given at the Wilton Park Conference 663 – Climate Change: What Can Be Done? May 14, 2002. U.S. Department of State. http://www.gcrio.org/OnLnDoc/pdf/HWatson020514.pdf

5. Wofsy, S.C and R.C. Harriss, co-chairs. A report of the NACP Committee of the U.S. Carbon Cycle Science Steering Group, U.S. Global Change Research Program, Washington, DC, 2002. http://www.esig.ucar.edu/nacp/

6. Yakir, D. and X-F Wang, Fluxes of CO_2 and water between terrestrial vegetation and the atmosphere estimated from isotope measurements, Nature, 380, 515-517, 1996.

7. Yakir, D. Framework for incorporation of stable isotope measurements in selected Carboeuroflux sites. Appendix to Work Package 5: Stable isotope studies, 2000. http://www.weizmann.ac.il/ESER/Yakir/Keeling_plots.html

8. Francey, R.J. et al., Changes in oceanic and terrestrial carbon uptake since 1982, Nature 373, 326 – 330, 1995.

9. U.S. EPA, Global Warming Potentials, http://yosemite.epa.gov/oar/globalwarming.nsf/content/EmissionsNationalGlobalWarmingPotentials.html

Table A-1. FY2003 Requested Funding for Climate Change – Related Programs.

Data from Reference 4.

Program	**$ Millions**
CLIMATE CHANGE SCIENCE	
US Global Change Research Program (USGCRP)	
NASA	1109
NSF	188
DOE	126
DOC (NOAA)	100
NIH	68
USDA	66
DOI (Interior)	28
EPA	22
SI (Smithsonian Inst)	7
Total USGCRP	**1714**
Climate Change Research Initiative	
DOC	18
NSF	15
NASA	3
DOE	3
USDA	1
Total CCRI	**40**
Grand total CLIMATE CHANGE SCIENCE	**1754**
CLIMATE CHANGE TECHNOLOGIES	
DOE	
Energy conservation R&D	588
Renewable energy R&D	408
Office of Science	35
Energy information administration	3
Total DOE	**1034**
USAID	155
EPA	108
USDA	7
Grand total CLIMATE CHANGE TECHNOLOGIES	**1304**
OTHER CLIMATE CHANGE PROGRAMS	
Programs not supporting basic science or technology	**1418**
Grand total of ALL CLIMATE CHANGE PROGRAMS	**4476**

Table A-2. Weighted scores reflecting the instruments requested most often in written surveys. First choice was given a weighting of 3, second choice 2, and third choice 1. Weighted scores were summed and reported as the total score. Number of respondents = 15.

Gas(es)	**Score**
NH3	21
NO, NO2, NOx, HNO3	29
N2O	10
CH4	10
O3	10
CO	4
All others (CO2,SO2,H2S,SF6,HCHO,VOCs)	8

Table A-3. Detailed responses to surveys described in Table A-2.

Respondent	Gas	Meas range (min)	Meas range (max)	Response time	Precision as % of max range	Accuracy as % of max range	Price
1	O3	0	200ppb	slow	2.50%	2.5%	$1,000
4	O3	.1ppb	200ppb	10Hz	0.05%		$15,000
9	O3	0	100ppb	10Hz	0.40%	3.0%	$15,000
10	O3	0	200ppb	10Hz	0.25%	5.0%	
1	CO			slow	5.00%	5.0%	$750
2	CO	.04ppb	1000ppb	kHz	0.01%	0.03%	
3	CO	100ppb	10000ppb	20Hz	0.10%		$17,500
2	NO	.04ppb	1000ppb	kHz	0.01%	0.03%	
6	NO		ppb	3min	1.00%		$30,000
10	NO	0	200ppb	10Hz	0.13%	5.0%	
11	NO			2Hz			$30,000
12	NO	.05ppb	50ppb	1Hz	5.00%	5.0%	$10,000
13	NO	.05ppb	5ppb	5Hz	5.00%	12.0%	
3	NO2	.05ppb	50ppb	20Hz	0.02%		$17,500
4	NO2	.01ppb	100ppb	10Hz,(5min)	0.10%		$15,000
10	NO2	0	200ppb	10Hz	0.10%	5.0%	
12	NO2	.05ppb	50ppb	1Hz	5.00%	5.0%	$10,000
13	NO2	.05ppb	5ppb	5Hz	5.00%	12.0%	
7	NOx	0	100ppm	10Hz	0.10%	1.0%	$10,000
4	HNO3	.01ppb	10ppb	10Hz,(5min)	0.10%	1.0%	$15,000
12	HNO3	.05ppb	50ppb	1Hz	5.00%	5.0%	$10,000
2	N2O	.04ppb	1000ppb	kHz	0.01%	0.03%	
5	N2O	.1ppb	2ppb	10Hz	2.50%	5.0%	
8	N2O	200ppb	1000ppb	10Hz	0.50%	1.0%	$10,000
11	N2O			2Hz			$30,000
14	N2O	.1ppm	100ppm	10Hz	3.00%		$20,000
15	N2O	0	1ppm	1Hz			
3	NH3	.05ppb	50ppb	20Hz	0.02%		$17,500
4	NH3	.01ppb	50ppb	10Hz,(5min)	0.02%		$15,000
5	NH3	.1ppb	125ppb	10Hz	0.01%	0.8%	
6	NH3		ppb	3min	1.00%		$30,000
7	NH3	1	100ppm	10Hz	0.10%	1.0%	$10,000
9	NH3	0	125ppb	10Hz	0.03%	3.0%	$15,000
12	NH3	1ppb	1000ppb	10Hz	5.00%	10.0%	$15,000
5	CH4	.5ppb	2.5ppb	10Hz	2.00%	4.0%	

Respondent	Gas	Meas range (min)	Meas range (max)	Response time	Precision as % of max range	Accuracy as % of max range	Price
7	CH4	0	100ppm	10Hz	0.10%	1.0%	$10,000
8	CH4	1.6ppm	100ppm	5Hz	0.01%	1.0%	$10,000
11	CH4		3ppm	2Hz	0.03%		$30,000
14	CH4	.1ppm	10ppm	10Hz	3.00%		$20,000
6	SO2		ppb	3min			$30,000
9	H2S	0	60ppb				
12	VOCs	.05ppb	100ppb	2Hz	5.00%	5%	$25,000
13	SF6		ppb	5Hz	5.00%	12%	
13	HCHO	.05ppb	5ppb	5Hz	5.00%	12%	
average					**1.72%**	**4.4%**	**$16,698**
median					**0.25%**	**4.4%**	**$15,000**

Table A-4. The number of eddy covariance flux sites participating in flux networks around the world. Data compiled from informal counts of flux sites from the homepages of each flux network. Information given at the Ameriflux meeting held October 2002 indicated the number is 202 worldwide.

Network	Number of sites
AmeriFlux	88
Fluxnet-Canada	7
Carboeuoflux	33
Asia Flux (Japan & Pacific Rim)	41
Oz Flux (Australia & NZ)	8
Ko Flux (Korea & SE Asia)	10
Total identified from the web	**187**
Total reported at Ameriflux 2002	**202**

APPENDIX B

LI-COR Engineering Report

Technical Evaluation of the High Precision Analyzer Prototype Implementation

December 2, 2002

LI-COR Engineering

This report contains CONFIDENTIAL AND PROPRIETARY LI-COR INFORMATION
"The following information is Confidential and Proprietary LI-COR INFORMATION and this information is covered by the terms of the PSI/LI-COR MUTUAL NONDISCLOSURE AGREEMENT, signed March, 2000; and the JOINT DEVELOPMENT AGREEMENT between Physical Sciences and LI-COR, effective April, 2001. The parties have agreed to use all necessary means to guard this LI-COR INFORMATION as Confidential and Proprietary."

DISCLAIMER
"LI-COR INFORMATION is hereby provided as a good faith effort to fulfill the obligations of APPENDIX B and APPENDIX C of the JOINT DEVELOPMENT AGREEMENT between Physical Sciences and LI-COR, effective April, 2001. In so providing this LI-COR INFORMATION, LI-COR makes no representation as to its accuracy or utility for making future product or business decisions."

PSI provided to LI-COR Engineering 3-D CAD files for the purposes of evaluating the implementation of an open path gas analyzer prototype. Utilizing the CAD files, the evaluation focused primarily on structural and environmental observations related to the system in general and specifically on the "sensor head". This evaluation is based on the experience LI-COR has developed over many years, working with both closed path and open path CO_2 measurements in diverse measurement scenarios.

System Level Evaluation

Based on the CAD rendering, the Control Box seems quite extensive and appears to need a controlled operation environment in terms of operating temperature range and power consumption. It is assumed that the system design allows for a long cable to connect the sensor head to the control box due to this fact. Of concern would be the noise introduced with a long cable between these two elements of the system. If fiber optics were used, then the signal degradation concern would be minimized. The chief concerns here relates to the fact that many measurement sites that would use such an analyzer are in remote locations. These sites typically have a limited power budget and may be exposed to significant temperature range variation. System designs that require a demanding power budget and operational environment could be limiting.

Typically these systems are integrated with other key measurements systems to provide a combined data set for evaluation. What mechanisms have been designed into the system to enable synchronized data collection? What is the form of the output? What is the frequency response of your system? Signal to noise ratio? How stable is the measurement system and what is the frequency of recalibration required due to system drift?

Sensor Head Evaluation

The sensor head seems rather large for some eddy covariance measurements. It appears most suitable for placement at high elevations where eddies are large. What will be discovered is that the scientists making these types of measurements want the sensor head to be in close proximity to the sonic anemometer for measurement correlation. They will therefore be concerned about the physical footprint of the analyzer. Optical path support structures that offers the least wind disturbance is the best choice

The structural integrity of the design such that the detector and source housing orientations are maintained throughout typical environmental conditions, particularly high winds is a concern. Large physical footprints in the detector and source housings will increase the demand for a more substantial mechanical structure. This is in opposition to the previous discussion in terms of airflow perturbation. This extends then to a vibration analysis of the system under such conditions and how this effects the operation of the head. Is maintaining alignment a concern given the current design implementation?

Certainly rain, snow and dirt created by various events will be concerning in terms of performance degradation. What aspects of the design minimized water retention around the optics? Is cleaning going to be required for dirt buildup? How does the system perform over a wide temperature range consistent with many measurement locations currently used by the scientific community?

How do you calibrate the sensor head? Is it required? Of particular concern here is the measurement setup at a typical site and how the scientist ensures calibration of the analyzer in the regular maintenance of their system configuration.